Astronomy Reports, Vol. 44, No. 2, 2000, pp. 103–111. Translated from Astronomicheskiĭ Zhurnal, Vol. 77, No. 2, 2000, pp. 124–133.

The Large-Scale Magnetic Field on the Sun: The Equatorial Region

V. N. Obridko and B. D. Shel'ting

Institute of Terrestrial Magnetism, Ionosphere, and Radiowave Propagation, Russian Academy of Sciences, Troitsk, Moscow oblast, 142092 Russia

Received February 24, 1999

Abstract—The sector structure and variations in the large-scale magnetic field of the Sun are studied in detail using solar magnetic-field data taken over a long time interval (1915–1990). The two-sector and four-sector structures are independent entities (i.e., their cross correlation is very small), and they are manifest in different ways during the main phases of the 11-year cycle. The contribution of the two-sector structure increases toward the cycle minimum, whereas that of the four-sector structure is larger near the maximum. The magnetic-field sources determining the two-sector structure are localized near the bottom of the convection zone. The well-known 2–3-year quasi-periodic oscillations are primarily associated with the four-sector structure. The variations in the rotational characteristics of these structures have a period of 55–60 years. The results obtained are compared with the latest helioseismology data. © *2000 MAIK "Nauka/Interperiodica"*.

1. INTRODUCTION

The present work continues a series of papers [1–3] devoted to studies of cyclic variations in the structure of the large-scale magnetic field on the Sun over a long time interval (1915–1996) using both direct measurements of the magnetic fields [4–7] and computations of the fields derived from Hα spectroheliograms. The main problem here was the development of a method for polar correction, enabling us to calculate the field structure on the source surface and, therefore, to reveal the main harmonics of the global field. We describe this method in [1–2], together with a comparison between the computed polar field and the number of polar faculae. These two quantities have almost the same time behavior.

A detailed comparison between the structure of the reconstructed global magnetic field (GMF) at the source surface and the sector structure of the interplanetary magnetic field (IMF) was presented in [3]. We used the most complete series of IMF data (1926–1990), obtained by Svalgaard and coworkers (see [8–11]) and Mansurov *et al.* [12] from geomagnetic measurements. The method developed by Mansurov and Svalgaard enables reconstruction of the sign of B_x component of the interplanetary magnetic field using ground-based geomagnetic data. In the optimal case, this procedure requires data from several geomagnetic observatories in the Arctic and Antarctic. Unfortunately, this condition was fully satisfied only after 1958. Restoration results for earlier times are considerably less reliable, and IMF data are completely absent before 1926.

We used computed values of the magnetic field amplitude on the source surface at the helioprojection point of the Earth as GMR data. The time resolution of all data was one day. In general, the structure reconstructed from the Hα data is in satisfactory agreement with that derived from geomagnetic data, especially, after 1958, when both data series coincide in detail. For earlier periods, our data seem to be more reliable.

To obtain more accurate comparisons between the GMF and IMF data, we calculated mean annual spectra for the entire data set and constructed the patterns of these spectra (Fig. 1). Both spectra show two- and four-sector structures (27 and 13 days) and demonstrate similarity in the time variations of their amplitudes.

In the present paper, we study the cyclic variation and rotation of the two- and four-sector structures of the large-scale magnetic field. We emphasize that, everywhere, we refer to *synodic* rotational periods.

Our computation of the field at the source surface, in fact, corresponds to a spatial filtration and automatically separates the field harmonics that vary most slowly with height. Consequently, all subsequent conclusions about the structural characteristics refer to some unknown depth under the photosphere, which we will call the generation region of the corresponding structure of the global magnetic field.

2. PREVIOUS STUDIES OF THE SECTOR STRUCTURE

The concept of the sector structure of the interplanetary magnetic field appeared in 1965, when Wilcox and Ness, via direct observations using the IMP 1 satellite, discovered that the interplanetary magnetic field is usually directed toward or away from the Sun over quite long time periods, of the order of several days [13, 14]. This structure exists for several years and rotates with a period close to 27 days. It was believed for a long time

1063-7729/00/4402-0103$20.00 © 2000 MAIK "Nauka/Interperiodica"

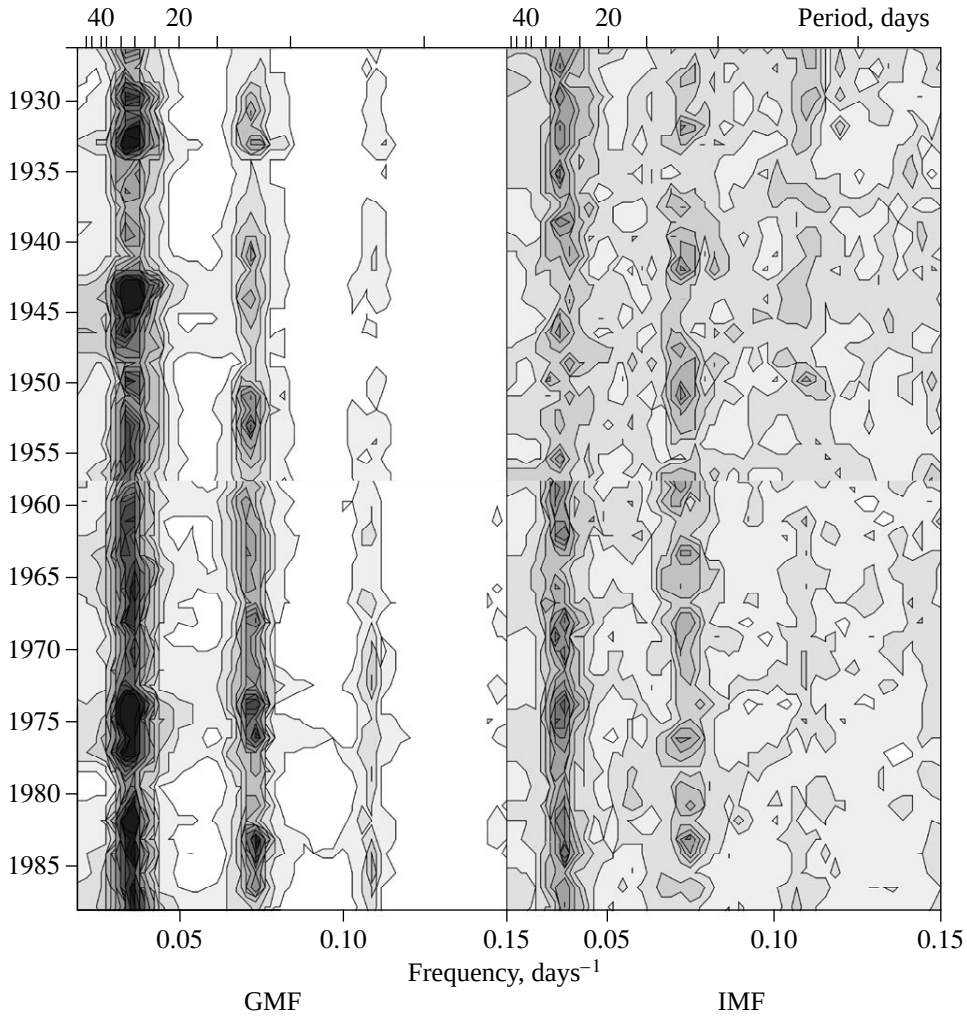

Fig. 1. Spectra of the GMF (left panel) and IMF (right panel).

that this structure is primarily composed of four sectors, as at the time of its discovery. However, this was later subject to question [15–19]. Unfortunately, the relation between these two modes has not yet been fully studied. It is not clear how often the four-sector structure occurs, how well it is correlated with the main mode, and how these structures rotate when they are studied separately.

It is now quite clear that the sector structure (at least, from the point of view of its basic characteristics) is a continuation of the global magnetic field into interplanetary space. Therefore, subsequent analysis of the sector structure reduces, in effect, to analysis of the structure and cyclic variations of the global magnetic field of the Sun.

As shown previously in [15, 18], there are clearly-detected cyclic variations in the sector structure of the IMF. A two-sector structure with a rotational period of over 27 days (27.5–28.5 days) is always observed at the cycle maximum. Next, in the decline phase, the structure acquires a four-sector character with a clear 27-day recurrent period. At the cycle minimum, the structure of the IMF either disappears as a result of the Rosenberg–Coleman effect or acquires the form of a two-sector structure with a recurrent period of about 27 days. Of course, the Rosenberg–Coleman effect is absent when analyzing the solar magnetic field; nevertheless, we expect that the sector structure will disappear due to a weakening of the zonal coefficients. The two-sector structure that is finally formed plays the leading role up to the next cycle maximum, with the rotational period increasing to 27.5–28.5 days. It is interesting that the secondary solar-activity maximum in 1972 led to a disruption of the already-formed four-sector structure with a period of about 27 days, typical for the decline phase, and a short-time re-establishment of a two-sector structure with a rotational period 28.0–28.5 days, characteristic of the cycle maximum.

Thus, a higher level of solar activity corresponds to lower rotational velocity and (somewhat unexpectedly) to better-defined two-sector structure. In general, four-sector structure is a quite rare phenomenon: It does not

exist in a pure state at all and appears as a substantial addition to the two-sector structure in the decline phase, just after the field reversal.

In general, these results of our analysis of the structure and rotation of the IMF are in agreement with the results of other studies. For example, Svalgaard [20] obtained the following periods for various phases of the cycle: 27.1 days at the minimum, up to 28.3 days at the phase of increasing activity, and a nearly constant value of 27.2 days in the second part of the cycle. Wilcox and Colburn [21, 22] obtained rotational periods of 27.5 days for the period of increasing activity and ~27.0 days for the second part of the cycle. We emphasize that no difference between the two sector-structure modes was taken into account in [20–22], and their results essentially correspond to the entire IMF. Since, as noted above and shown below, the two-sector mode is the most significant, the results of [20–22] should correspond primarily to this mode.

An attempt to analyze only the four-sector structure in [10, 11, 23] was not entirely successful in our opinion. These authors assumed that the four-sector structure was inevitably present and separated it from the primary data by calculating the correlation function between these data and a model with four equally spaced sectors. They then derived the two-sector structure, which was not permanent, from the corresponding residuals. Thus, some results obtained in [23] do not agree with those obtained previously by the same authors [20–22]. In the present paper, we describe an alternative approach, which enables us to find the characteristics of both modes simultaneously and does not suffer from the drawbacks of the previous studies.

3. FORMULATION OF THE PROBLEM AND MATHEMATICAL TECHNIQUE

We based the development of our method for analyzing the solar magnetic field on the necessity of studying both modes of the sector structure on the Sun simultaneously, without assuming priori that one of these modes is dominant. Although we initially used Hα maps, which give only the field polarity, the field intensity can also be restored to some extent in the calibration process during the computation of the field at the source surface, as was shown in [1, 2]. This fact gives us an added advantages compared to the material used in [10, 11, 23].

A sequence of daily values of the magnetic field at the source surface was calculated for each heliolatitude from 50° S to 50° N in intervals of 10° from January 1, 1916, to December 16, 1988. This yielded 11 data sets with 26649 points in each. Further, using a moving interval with a length of 54 days and a shift of 27 days, we approximated the daily magnetic-field values via a least-squares method, using the formula

$$y_i = A_1\cos(2\pi i/T) + A_2\sin(2\pi i/T) + A_3\cos(4\pi i/T) + A_4\sin(4\pi i/T) + A_5, \quad (1)$$

$$A_{12} = \sqrt{(A_1^2 + A_2^2)}, \quad A_{34} = \sqrt{(A_3^2 + A_4^3)},$$

$$\tan\varphi_1 = A_1/A_2, \ \tan\varphi_2 = A_3/A_4, \ T = 27.275 \text{ days}.$$

It is obvious that the period $T = 27.275$ days, equal to the Carrington rotation period, was taken only as a test period. The phases φ_1 and φ_2 specify the positions of the maxima for the two- and four-sector structures in a heliographical longitude system, and the phase variations can easily be recalculated to determine the real rotational periods T_2 and T_4, respectively. All amplitudes are expressed in units of the mean-square approximation errors. Next, we smoothed the data using a standard moving interval composed of 13 points, where we took the window boundary points into consideration with half the statistical weight, and the smoothed value corresponds to the middle point of the window. In this way, we obtain four characteristics of the structure: The relative significance of the two-sector structure A_{12}, the relative significance of the four-sector structure A_{34} (in our subsequent discussion, these two quantities will sometimes be referred to as the amplitudes of the structures), the rotational period of the two-sector structure T_2, and the rotational period of the four-sector structure T_4. Each of these is a function of latitude (with resolution 10°) and time (with resolution 27 days). We can compare these dependences directly or use correlation and Fourier analyses.

In subsequent sections, we study the behavior of these quantities for the equatorial zone. The latitudinal dependence of this behavior will be considered in a future paper.

4. CHARACTERISTICS OF THE SECTOR STRUCTURES IN THE EQUATORIAL ZONE

4.1. Relative importance of the two-sector and four-sector structures. Figure 2 presents the $A_{12}(t)$ and $A_{34}(t)$ dependences in the equatorial zone. Despite their quite complex character, we can see that $A_{12}(t)$ and $A_{34}(t)$ can everywhere be distinguished quite reliably: All values of the coefficients are considerably greater than unity. The values of A_{12} are almost always significantly greater than those of A_{34}. The mean value of the ratio A_{34}/A_{12} over the entire observation interval is 0.52. The four-sector structure becomes comparable to (or even more significant than) the two-sector structure only within certain separate, very short time intervals.

Note that the cyclic character of the behavior of the two modes is quite different. For example, the widespread opinion that the four-sector structure represents merely a harmonic of the two-sector structure is not valid. The correlation coefficient between the functions $A_{12}(t)$ and $A_{34}(t)$ is only 0.158.

The dependence of the measured values of A_{12} on the phase of the 11-year cycle is shown in Fig. 3a. Phases 0.0 and 1.0 correspond to the Wolf-number min-

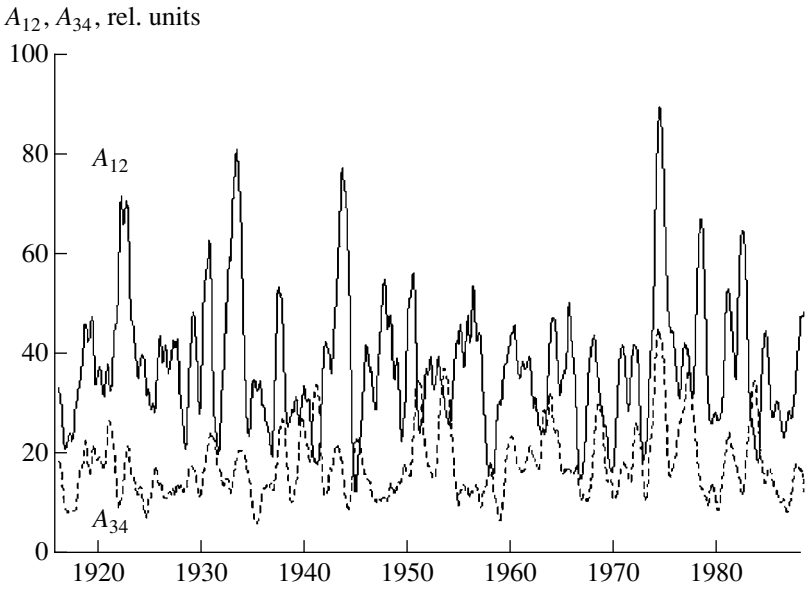

Fig. 2. Amplitudes of the two-sector (solid curve) and four-sector (dashed curve) structures as functions of time.

ima, and the cycle maximum occurs at phase 0.35–0.4. Although there is no clearly identified dependence, we can see that the largest values of A_{12} occur in the decline phase and, especially, at the cycle minimum. Therefore, the disappearance of the sector structure near the cycle minimum revealed in analyses of the IMF is not confirmed by our analysis of the large-scale magnetic field. The values of A_{12} are relatively small near the maximum. This is associated with the reversal of the global magnetic field, which is also manifest in the equatorial region.

The cyclic dependence of A_{34} (Fig. 3b) has maxima at phases 0.07, 0.36, 0.68, and 0.89. The first, third, and fourth points correspond to the phase of minimum (the reference points t_{Dm}, t_{min}, and t_{mA} introduced by Kuklin *et al.* [24–26]), whereas the second point coincides with the cycle maximum. Therefore, the cyclic dependence for A_{34} is sharply distinct from the dependence for A_{12}.

Figure 3c illustrates variations in the ratio A_{34}/A_{12} as a function of the cycle phase. We can see that this ratio is close to 0.5 over most of the plot. However, A_{34} exceeds A_{12} (i.e., the four-sector structure becomes quite significant) near phases 0.1, 0.35, 0.7, and 0.9. It is difficult to say whether these maxima are associated with the corresponding reference points of the cycle, or if they are the result of quasi-periodic fluctuations with characteristic periods 2–3 years, which will be discussed below.

4.2. Rotation of the two-sector and four-sector structures. The synodic rotational periods of the two- and four-sector structures $T_2(t)$ and $T_4(t)$ are presented in Fig. 4. The rotational period $T_2(t)$ changed in quite a regular way during the 15th–18th cycles: This period gradually increased in the phase of increasing activity and reached its maximum value at the end of this phase or just at the cycle maximum. This period then gradually decreased to its initial value, close to 27 days. Starting from the 19th cycle, some deviations appeared in this pattern. The maximum values of T_2 in the 19th and 20th cycles were achieved in 1962 and 1973, respectively, i.e., in the decline phase. In principle, this could be associated with the secondary solar-activity maximum observed in these cycles two years after the tabulated main maxima. Finally, the maximum rotational period in the 21st cycle was achieved almost at the beginning of the cycle minimum, in 1986. The mean rotational period over the entire interval under consideration is 27.6 days.

The mean rotational period T_4 is greater than or equal to 27.9 days. There are virtually no variations within the cycle, apart from an appreciable decrease in the 1940s–1950s (see Fig. 7 below). As for the correlation coefficient (A_{12}, A_{34}), the correlation coefficient (T_2, T_4) is negligible and equal to 0.018. This provides an additional argument that these two modes are independent. It may be that precisely such variations in the rotational period in the last cycles, and especially in the pattern of variations of T_2 and T_4 within the cycle, were the reason for the disagreement between the results of [20–22].

It is interesting that, although neither the amplitudes nor the periods of the structures correlate with each other, the difference of the periods T_2–T_4 (Fig. 5) varies in a regular fashion, suggesting the existence of a quasi-period of about two to three years with a quite stable amplitude. The character of these oscillations does not change with time, and there is no appreciable dependence on the phase of the 11-year cycle.

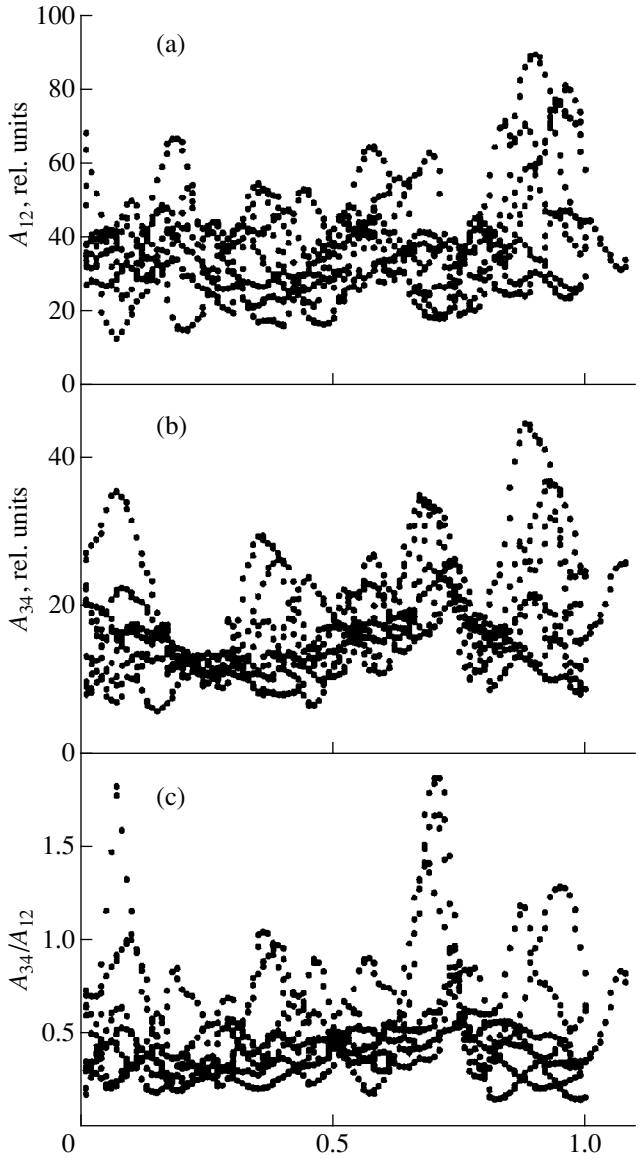

Fig. 3. Dependences of the (a) two-sector and (b) four-sector structures and (c) their ratio on the phase of the 11-year cycle.

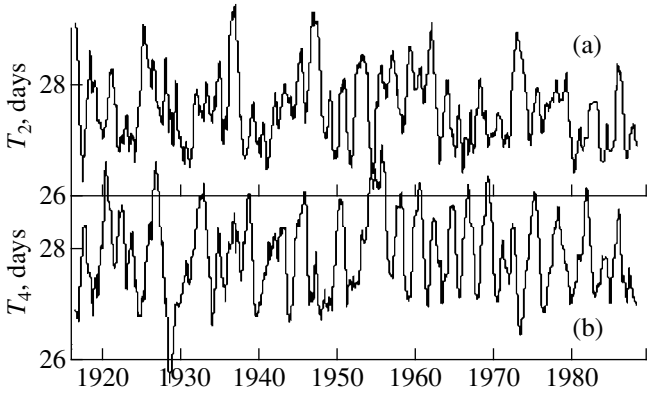

Fig. 4. Time dependence of the amplitudes of the synodic periods of rotation for the (a) two-sector and (b) four-sector structures.

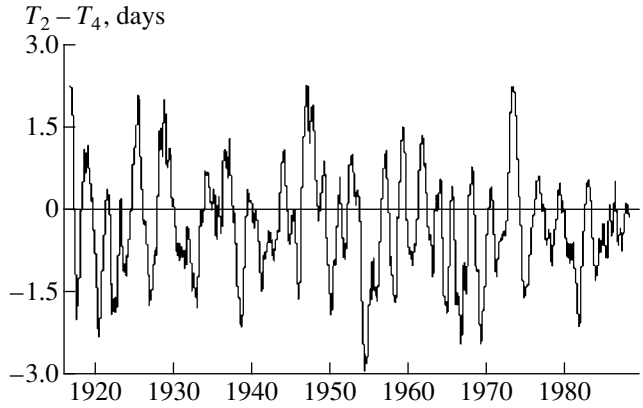

Fig. 5. Time dependence of the difference between the synodic periods of rotation of the two- and four-sector structures.

4.3. Quasi-periodic variations in the sector structures. We searched for quasi-periodic variations in the sector structures using a Fourier expansion over the entire time interval. One time unit was equal to 27 days, and each data set contained 972 points. Since we searched for periods from several years to 11 years, this time resolution was quite sufficient.

Figure 6 presents the Fourier spectra for A_{12}, A_{34}, and T_2–T_4. The frequencies corresponding to the quasi-periods in the adopted time units are plotted on the horizontal axis. For example, the frequency 0.02 corresponds to a quasi-period of 50×27 days, i.e., 1350 days or 3.7 years. We can see in Fig. 6 that, apart from the obvious period of about 10 years (this is the 11-year cycle, whose length in the 20th century was slightly greater than 10 years), quasi-periods of several years are clearly visible in the spectra. In the spectrum of A_{12}, the most significant frequency is 0.022, corresponding to a quasi-period of 3.36 years. This is surrounded by less significant quasi-periods in the range 3–5 years.

Separately, we can see quasi-biennial periods in the spectrum (whose frequencies are 0.034–0.036 and 0.042). In the spectrum of A_{34}, the quasi-triennial (with frequencies 0.022–0.026) and quasi-biennial periods can be identified even more clearly and do not have such powerful satellites as in the spectrum of A_{12} near the frequency 0.022. Thus, 2–3-year fluctuations (or quasi-periodic oscillations), well known from previous studies, are clearly visible in the spectrum of the sector-structure amplitudes.

As regards the spectra of variations in the rotational periods, neither the 11-year cycle nor the 2–3-year oscillations are appreciable in the total spectrum, which resembles noise (it is not presented here). On the other hand, the frequency 0.026 (which corresponds to a

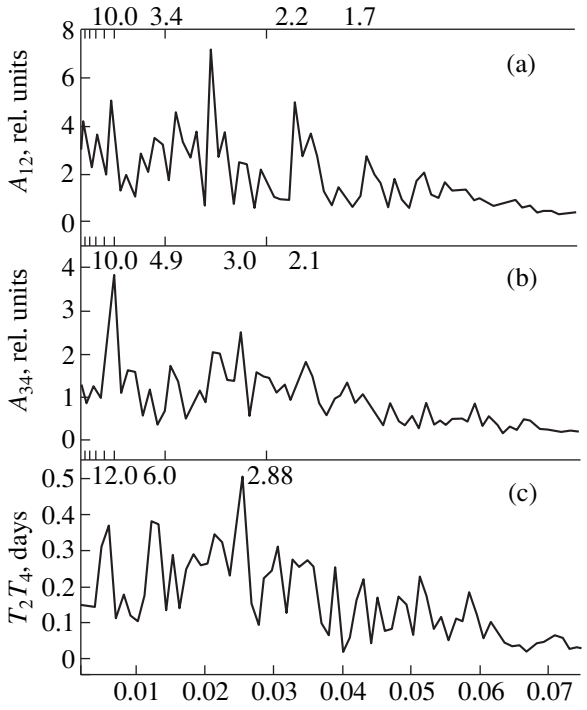

Fig. 6. Spectra of amplitudes for the (a) two-sector and (b) four-sector structures and (c) the difference between the periods of these structures. The horizontal axis is the frequency in units of 1/27 days^{-1}. Values of the corresponding periods (in years) for the most significant maxima in the spectra are given above the curves.

quasi-period of about three years) is quite prominent in the spectrum of T_2–T_4.

The quasi-noise-like character of the rotational-period spectra is probably due to the instability of cyclic variations in the rotational periods noted above (see Section 4.2). As a result, the spectrum derived from the entire observation interval does not satisfy the steady-state condition and leads to a quasi-noise pattern. On the other hand, some intrinsic correlation between the variations in the periods T_2 and T_4 is manifest as the appearance of quasi-periodic oscillations in T_2–T_4.

To verify this possibility, we separated the entire data set into two intervals. The first interval includes data for the 15th–18th cycles, i.e., from January 1916 to April 1954. The second interval corresponds to the 19th–22nd cycles and ends in 1988. As could be expected from the data presented in Section 4.2, the spectra of T_2 and T_4 become slightly more informative. The 11-year cycle (whose quasi-period is 9.2 years) becomes clearly visible in the first interval for T_2. The residual spectrum for the first interval has a noise-like character. The spectrum of T_2 in the second interval changed radically. The main maximum corresponds to a period of 18.02 years and contains no traces of the quasi-period of about 10 years. In addition, periods of 5.7, 4.2, and 1.7 years can be distinguished.

The spectrum of T_4 also contains no traces of the 10-year period in either the total realization or the truncated intervals. In the spectrum of T_4 for the first interval, there is a broad maximum in the period range 6.3–4.7 years, and the spectrum monotonically decreases toward higher frequencies. For the second interval, we can see two broad maxima in the period ranges 3.4–2.8 and 2.4–2.1 years. All other frequencies are expressed considerably more weakly.

Thus, it seems that there is no stable pattern for the variations in the rotational periods of the sector structures within a cycle. In general, this pattern is very unstable and changes from cycle to cycle, especially in the 19th and subsequent solar-activity cycles.

4.4. Variations in the characteristics of the sector structures over a long time interval. As we saw above, some characteristics of the sector structure change from cycle to cycle. This brings up the question: Are there regular features in such variations, and are periods longer than 11 years present?

It is rather difficult to analyze the corresponding behavior directly on the basis of the figures presented above. Therefore, we conducted additional smoothing of the data. All values were averaged over 27 points, i.e., over a two-year interval. Then, to exclude the influence of the 11-year cycle, we took values corresponding to the dates of maxima and minima in the Wolf-number cycles. The resulting values are presented in Fig. 7. Points corresponding to the cycle maxima are drawn by circles and joined by solid lines. Points corresponding to minima are drawn by stars and joined by dashed lines.

We can see in this figure that the transition from the 18th to the 19th cycle is characterized by substantial variation in the global solar activity. The maximum rotational period T_2 for both the maximum and minimum cycle phases is achieved at the time indicated above. A decrease in T_4 for the maximum phases is observed at the same time (and proceeding it). Accordingly, this time is also characterized by a sharp increase in the difference between the rotational periods T_2–T_4. We have the impression that this phenomenon has a periodic character (especially for T_4), with a period of 55–60 years. This dependence is more clearly visible in the rotational periods corresponding to the maximum phase.

In general, the rotational periods at the cycle minima do not show significant variations in the period under investigation. Nevertheless, we note some increase in the period T_2 for the minimum phase in the minimum between the 18th and 19th cycles. Moreover, as noted in Section 4.2, the rotational period T_2 was significantly greater at the maximum than at the minimum right up to a certain interval in the 18th–19th cycles, when this inequality was disrupted.

The characteristic behavior of the amplitudes of the two-sector and four-sector structures also changed during this specific interval in the 18th–19th cycles. Before

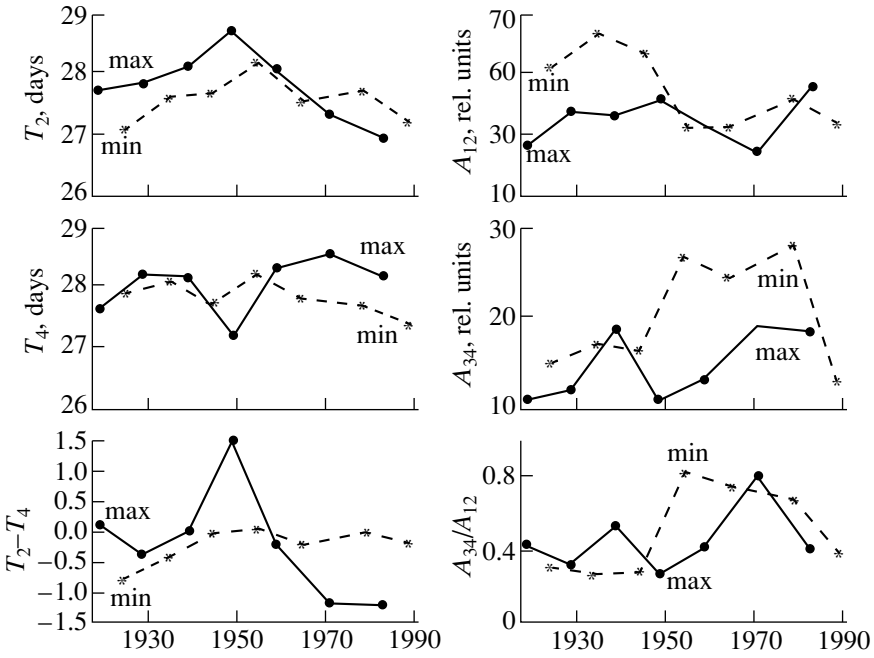

Fig. 7. Time dependence of the quantities T_2, T_4, $(T_2–T_4)$, A_{12}, A_{34}, and A_{34}/A_{12} at the maximum (solid lines) and minimum (dashed lines) phases of the 15th–21st solar-activity cycles.

1948–1952, A_{12} was substantially greater at the minimum than at the maximum. After this interval, the values of A_{12} at the maxima and minima are approximately equal. On the other hand, the behavior of A_{34} is exactly opposite: The values of A_{34} at the maximum and minimum of each cycle are roughly equal before 1952, and the minimum value of A_{34} became dominant after this. We can also note a gradual increase in the relative significance of the four-sector structure.

In general, Fig. 7 and some of our previous discussion indicate a "supplementary" character for the behavior of the sector structures. Despite the fact that direct correlations between parameters of the sector structures are negligible, the general characteristics of the cyclic and long-term variations are such that, from a qualitative point of view, these parameters vary in antiphase.

5. DISCUSSION

Our main results are summarized below.

We confirm the conclusions drawn in [15–19] that the two-sector structure dominates in the large-scale magnetic field. The average amplitude ratio A_{34}/A_{12} is 0.52. These amplitudes are comparable only during certain quite short intervals, which are usually characterized by a decrease in A_{12} rather than by an increase in A_{34}. As a result, the widespread concept that the four-sector structure is merely a harmonic of the two-sector structure is not valid. They are not correlated but, at the same time, are closely connected. This is revealed by the regular behavior of $T_2–T_4$ and the opposite qualitative behavior of these structures over long time intervals.

The amplitudes of the four-sector and two-sector structures become comparable at phases 0.1, 0.35, 0.7, and 0.9, i.e., near the reference points of the cycle. In general, since there are four reference points plus phases of maximum and minimum within each cycle, the increase in activity at these times can be interpreted as quasi-biennial oscillations. On the other hand, it is possible that precisely these oscillations (or, more precisely, the quasi-periodic 2–3-year fluctuations) stimulate the sharp changes in the solar activity that we take as the reference points of the cycle. Similar considerations have been put forward by Vitinskiĭ [27].

The 2–3-year oscillations have been observed by many investigators using various solar features and indices. The corresponding results are described in many papers, which we do not cite here in detail. However, we would like to mention some reports at the symposium held in Pushchino on February 25–27, 1991, devoted to the problem of quasi-biennial oscillations. This oscillation mode has been revealed in variations of solar activity in the polar zones [28, 29], the characteristics of the large-scale magnetic fields [30], dynamics of sunspot indices [31], and geomagnetic activity [32, 33]. A review of earlier studies is given in the monograph by Rivin [34]. Among later results, we note the discovery of quasi-biennial oscillations in the magnetic field of the Sun as a star [35], in the solar neutrino flux [36–38], and in the displacement of magnetic neutral lines [39]. There is an extensive bibliography in [39]. In addition, we note the presence of quasi-biennial oscillations in the Earth's stratosphere [40], although it

remains unclear if they are related to the solar 2–3-year oscillations.

We can add the following features to the previously known properties of these oscillations.

(1) In fact, there is fine structure in these oscillations. Separate modes with periods of 3.4–3.0, 2.1, and 1.8 years are nearly always present. The fine structure of these oscillations varies considerably, depending on the particular solar characteristics or indices used for the analysis.

(2) For some parameters (in particular, T_2–T_4), these oscillations are expressed even more clearly than the 11-year cycle. It seems that this mode exists independent of the 11-year mode.

(3) The 2–3-year oscillations are detected more clearly in the four-sector structure, especially when analyzing its amplitude rather than its rotational period.

Let us now discuss our results concerning the rotational periods of the structures. Variations within the solar cycle (first and foremost, the 2–3-year oscillations) were better revealed in our analysis of the amplitudes; when analyzing the periods, such variations are expressed only weakly, and display a quite complex quasi-noise pattern. Exceptions are the quantity T_2–T_4 and the fact that, over a series of cycles, the rotational period of the two-sector structure is greater at the cycle maxima than at the corresponding minima. The pattern of the variations in the periods over a long time interval is considerably more clearly defined. In the middle of the 20th century (i.e., in the 18th–19th cycles), we observe a sharp increase in T_2 and T_2–T_4 simultaneous with a general increase in the solar activity, and a corresponding decrease in T_4 at the cycle maxima. At the same time, the behavior of the ratio of the structure amplitudes changed (see Section 4.4 and Fig. 7). This phenomenon has a periodic character, with a period of 55–60 years. The corresponding dependence is more clearly expressed in the rotational periods corresponding to the maximum phase. We found the same periodic behavior earlier when analyzing computed variations in the parameter q characterizing variations in the divergence of polar plumes [1, 2]. The corresponding maximum of q was attained at exactly the same time, in the 18th–19th cycles. Makarov and Tlatov [41] also discovered a 55-year period in their analysis of torsional oscillations of the Sun in the period 1915–1990. The duration of the separate zone of fast and slow rotation reaches a minimum in 1950 and maxima in 1925 and 1975. If we take into account the fact that the data of [41] were smoothed over a four-year interval, the results of [1, 2, 41] and the present paper are in good agreement with each other. It is interesting that the same interval in the middle of the 20th century is also distinguished in variations of relations between solar, geomagnetic, and meteorological processes [42–44].

6. CONCLUSION

Thus, the two-sector and four-sector structures represent independent objects on the Sun. The four-sector structure is observed less frequently and expressed less clearly; its rotational period is slightly greater and decreases at the maximum of the 60-year cycle. It displays the 2–3-year oscillations more clearly. It appears that these two structures are generated in different layers of the Sun.

The relative location of these layers is a considerably more difficult problem. Helioseismology data [45] suggest a maximum of the rotational frequency (i.e., a minimum of the rotational period) in the equatorial zone of the convection layer. It is located at a depth $r \approx (0.93–0.94)R_0$ and corresponds to a *sidereal* rotational frequency of 467.3–470.1 nHz; i.e., to a *synodic* rotational period of 26.57–26.40 days. The period increases from this layer toward the center or surface of the Sun. The *sidereal* rotational frequency is 450 nHz (i.e., the synodic period is 27.67 days) at the solar surface and near the base of the convection zone. If the periods observed on the surface are interpreted as consequences of the rotation law for the generation region, the region of generation of the four-sector structure could be located both above and below the generation region for the two-sector structure. The presence of the 2–3-year oscillations in the neutrino flux [36–38] seems to provide an argument in favor of deeper localization of the generation region for the four-sector structure. On the other hand, the four-sector structure, 2–3-year oscillations, and higher rotational periods are associated with local fields and relatively small large-scale cells. Accordingly, the generation region for the four-sector structure should be localized in higher layers [46]. This dilemma probably can be resolved by analysis of the latitude dependence of the characteristics of the sector structures. This is precisely the aim of our next paper.

The results of [1, 2] can be interpreted as a rise of the generation region for the large-scale magnetic field to higher layers during the powerful 18th and 19th cycles. As a result, independent of any mutual localization, the rotational period of the two-sector structure should increase, in agreement with our results. On the other hand, the decrease in the period T_{34} observed at this time (Fig. 7) seems to provide an argument in favor of deeper localization of the four-sector structure.

ACKNOWLEDGMENTS

We thank V. I. Makarov for presentation of observational material (Hα maps) and G. Gaziev for help with the primary digital processing. This work was supported by the Russian Foundation for Basic Research (project code 99-02-18346).

REFERENCES

1. V. N. Obridko and B. D. Shel'ting, *Current Problems in the Solar Cycle* [in Russian], Ed. by V. I. Makarov and V. N. Obridko (GAO, St. Petersburg, 1997), p. 193.
2. V. N. Obridko and B. D. Shel'ting, Solar Phys. **184**, 187 (1999).
3. V. N. Obridko and B. D. Shel'ting, *New Cycle of Solar Activity: Observational and Theoretical Aspects* [in Russian], Ed. by V. I. Makarov and V. N. Obridko (GAO, St. Petersburg, 1998), p. 137.
4. J. T. Hoeksema, J. M. Wilcox, and P. H. Sherrer, J. Geophys. Res. **87**, 10331 (1982).
5. J. T. Hoeksema, J. M. Wilcox, and P. H. Sherrer, J. Geophys. Res. **88**, 9910 (1983).
6. J. T. Hoeksema and P. H. Scherrer, *Solar Magnetic Field–1976 Through 1985* (WCDA, Boulder, 1986).
7. J. T. Hoeksema, *Solar Magnetic Field–1985 Through 1990* (WCDA, Boulder, 1991).
8. L. Svalgaard, Dan. Meteorol. Inst. Geophys., Paper R-29 (1972), p. 36.
9. L. Svalgaard, Stanford Univ. Inst. Plasma Res. Rep., No. 648 (1976).
10. L. Svalgaard and J. M. Wilcox, Solar Phys. **41**, 461 (1975).
11. L. Svalgaard, T. L. Duvall, Jr., and P. H. Scherrer, Solar Phys. **58**, 225 (1978).
12. S. M. Mansurov, G. S. Mansurov, and L. G. Mansurova, Antarktika, No. 15, 16 (1976).
13. J. M. Wilcox and N. F. Ness, J. Geophys. Res. **70** (23), 5793 (1965).
14. J. M. Wilcox and N. F. Ness, Solar Phys. **1**, 437 (1967).
15. V. N. Obridko, *Problems in Cosmic Electrodynamics* [in Russian], Ed. by É. I. Mogilevskiĭ (Nauka, Moscow, 1981), p. 21.
16. V. N. Obridko and L. I. Starkova, *Problems in Cosmic Electrodynamics* [in Russian], Ed. by É. I. Mogilevskiĭ (Nauka, Moscow, 1981), p. 29.
17. G. V. Kuklin and V. N. Obridko, Preprint SibIZMIR (Siberian Institute of Terrestrial Magnetism, the Ionosphere, and Radiowave Propagation, Irkutsk, 1982).
18. V. N. Obridko, Soln. Dannye, No. 11, 54 (1984).
19. G. V. Kuklin and V. N. Obridko, *The Physics of Solar Activity* [in Russian], Ed. by É. I. Mogilevskiĭ (Nauka, Moscow, 1988), p. 146.
20. L. Svalgaard, Geophys. Papers, R-29 (Danish Meteorol. Inst., 1972).
21. J. M. Wilcox and D. S. Colburn, J. Geophys. Res. **74** (9), 2388 (1969).
22. J. M. Wilcox and D. S. Colburn, J. Geophys. Res. **75** (31), 6366 (1970).
23. L. Svalgaard, J. M. Wilcox, and Th. L. Duvall, Solar Phys. **37**, 157 (1974).
24. G. V. Kuklin, V. N. Obridko, and Yu. I. Vitinsky, Soln. Dannye, No. 3, 56 (1986).
25. G. Kuklin, V. N. Obridko, and Yu. Vitinsky, *Solar Terrestrial Predictions: Proceedings of a Workshop at Leura, Australia, October 16–20, 1989*, **1**, 474.
26. G. V. Kuklin, V. N. Obridko, and Yu. I. Vitinskiĭ, *XIII Consulative Meeting on Solar Physics* [in Russian] (Nauka, Siberian division, 1989), **1**, p. 321.
27. Yu. I. Vitinskiĭ, Soln. Dannye, No. 2, 90 (1991).
28. B. B. Benevolenskaya and V. I. Makarov, Soln. Dannye, No. 2, 89 (1991).
29. V. I. Makarov, V. V. Makarova, and A. G. Tlatov, Soln. Dannye, No. 2, 89 (1991).
30. I. V. Ivanov, Soln. Dannye, No. 2, 91 (1991).
31. G. V. Kuklin and L. A. Plyusnina, Soln. Dannye, No. 2, 95 (1991).
32. G. S. Ivanov-Kholodnyi and V. E. Chertoprud, Soln. Dannye, No. 2, 96 (1991).
33. D. I. Ponyavin, Soln. Dannye, No. 2, 99 (1991).
34. Yu. R. Rivin, *Cyclicity on the Earth and Sun* [in Russian] (Nauka, Moscow, 1989).
35. Yu. R. Rivin and V. N. Obridko, Astron. Zh. **69**, 1083 (1992).
36. V. N. Obridko and Yu. R. Rivin, Izv. Ross. Akad. Nauk, Ser. Fiz. **59** (9), 110 (1995).
37. V. N. Obridko and Yu. R. Rivin, Astron. Astrophys. **308**, 951 (1996).
38. V. N. Obridko and Yu. R. Rivin, Astron. Zh. **74**, 83 (1997).
39. V. I. Makarov, K. S. Tavastsherna, A. G. Tlatov, *et al. New Cycle of Solar Activity: Observational and Theoretical Aspects* [in Russian] (GAO, St. Petersburg, 1998), p. 115.
40. K. Labitzke and H. Van Loon, Ann. Geophys. **11**, 1084 (1993).
41. V. I. Makarov and A. G. Tlatov, Astron. Zh. **74**, 474 (1997).
42. P. V. Kishcha and I. V. Dmitrieva, *Current Problems in the Solar Cycle* [in Russian] (GAO, St. Petersburg, 1997), p. 116.
43. I. V. Dmitrieva, E. P. Zaborova, and V. N. Obridko, Astron. Astrophys. Trans. **16**, 133 (1998).
44. I. V. Kishcha and I. V. Dmitrieva, Geomagn. Aéron., 1999 (in press).
45. J. Schou, *et al.*, Astrophys. J. **505**, 390 (1998).
46. E. E. Benevolenskaya, Astrophys. J. Lett. **509** (1), L49 (1998).

Translated by Yu. Dumin

Astronomy Reports, Vol. 44, No. 2, 2000, pp. 112–121. Translated from Astronomicheskiĭ Zhurnal, Vol. 77, No. 2, 2000, pp. 134–143.

On Stereoimages of Some Structures in the Solar Atmosphere

A. A. Vedenov*, V. A. Koutvitsky, S. Koutchmy***, M. M. Molodensky**, and V. N. Oraevsky****

**Troitsk Institute for Innovation and Thermonuclear Research, Troitsk, Moscow oblast, 142092 Russia*

***Institute of Terrestrial Magnetism, Ionosphere, and Radiowave Propagation, Russian Academy of Sciences, Troitsk, Moscow oblast, 142092 Russia*

****Institut d'Astrophysique de Paris, CNRS, 98bis Bd. Arago, Paris, 75014 France*

Received December 23, 1998

Abstract—Three-dimensional structures in the solar chromosphere and corona are considered. It is demonstrated that two photoheliograms separated by ~1 day can be used (using computer-graphics methods) to construct a stereo image of the Sun. The algorithm for this is presented and carried out for H_α images of the total disk. A bulge in the equatorial region resulting from the differential rotation of the Sun can be seen in the stereo image. Structures called Whitney pleats in catastrophe theory are observed in the solar corona. Such structures are encountered in prominences. The well-known helmets (or streamers) are pleats of heliospheric plasma sheets. Isophotes for such a sheet and the degree of polarization of the radiation in the pleat are calculated and compared with observational data. © *2000 MAIK "Nauka/Interperiodica".*

1. INTRODUCTION

To construct physical models of coronal structures, we must know their real three-dimensional shapes. A number of computer-graphics methods have been developed to construct stereo images of various three-dimensional objects observed both in space and under laboratory conditions (see, for example, [1, 2]). Special attention has been paid to cases when incomplete information about the 3D structures is obtained from observations. In such cases, additional data on the objects under investigation are used. In particular, for the solar atmosphere, we can use model concepts of the structure and physical conditions in the solar chromosphere and corona, together with photographic images.

In some cases, one can construct 3D images using the stereo effect due to the rotation of the Sun. Koutchmy and Molodensky [3] used this approach to reconstruct ray structures observed during the 1991 eclipse near the western limb.

Polar regions, where polar plumes are observed, are of considerable interest. One problem relating to these structures is whether they uniformly fill the polar region or whether there is some region where they are predominantly concentrated. Using polarization observations, Saito [4] concluded that the Sun has no polar plumes near its poles. Eclipse polarization observations are quite difficult, so that this result is the only one of its kind up to the present time; i.e., it has not been either confirmed or rejected.

The main problem is that, up to now, polar plumes have been observed only during solar eclipses. However, the near-Earth spacecraft SOHO is currently providing continuous information about the white-light corona and resolving the above question using SOHO data is an important task connected with out-of-eclipse observations of the white-light corona.

Modeling the surface where the radial field changes sign, where a heliospheric sheet of dense plasma is located, showed that the folds and pleats of the surface formed by its projection onto the plane of the sky correspond to structures known as coronal helmets [5]. Therefore, it is not necessary to develop a theory for these so-called "streamers": they are simply the result of projecting a smooth curved surface onto a plane.

Moreover, the characteristic features of such projections are well-known to mathematicians. In particular, singularities in the vicinity of the vertices of such helmets (or pleats, in the notation adopted in catastrophe theory [6]) are described by a half-cubic parabola, $y = x^{3/2}$.

A stereo image of the solar disk at soft X-ray energies derived from data from the YOHKOH satellite was considered by Batchelor [7] in order to determine the height of bright X-ray points above the solar surface when they are projected onto the disk. In the context of such problems, it is important to answer the question of what is really observed when two spectroheliograms are used as a stereo pair.

1063-7729/00/4402-0112$20.00 © 2000 MAIK "Nauka/Interperiodica"

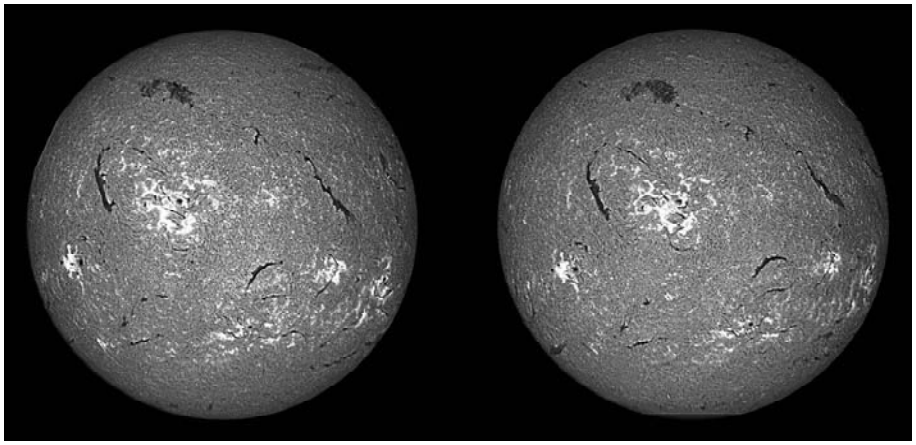

Fig. 1. H_α stereo image of the solar disk obtained using computer-graphics methods (the H_α filtergrams were kindly presented by B. Ioshpa).

2. STEREO IMAGES OF THE SOLAR DISK

We used two H_α photoheliograms of the total disk taken one day apart (Fig. 1), oriented so that the baseline of the stereo image was perpendicular to the solar rotation axis (see Appendix). As a result of the mutual positioning of these images, we can clearly see that several structures underwent substantial variations, including filaments and the chromospheric network. On the other hand, active regions, sunspots, and flocculi fully retained their shapes, and an observer's eyes are most attracted by precisely these structures. The solar disk turned out not to be spherical. Its shape is quite interesting: One can see a bulge extended in longitude in the equatorial region on the surface of the sphere.

Using spherical coordinates fixed to the Sun (with the z axis along the axis of rotation), we have $\mathbf{r} = R(\sin\theta\cos\varphi, \sin\theta\sin\varphi, \cos\varphi)$ and the displacement of the chromospheric surface over a time interval δt is

$$\delta\mathbf{r} = \delta t[\boldsymbol{\omega}\mathbf{r}]. \quad (1)$$

In projection onto the plane of the sky (with the y axis directed toward the observer), the displacements are

$$\delta\mathbf{r}_1 = [\mathbf{e}_y[\delta\mathbf{r}\mathbf{e}_y]]. \quad (2)$$

If we neglect the proper motions of the filaments, filament channels, active regions, and chromospheric structures, expression (2) determines the displacements of features on the disk. Substituting the expressions for $\mathbf{r}$ and $\delta\mathbf{r}$ into (1), we obtain

$$\delta\mathbf{r} = R\delta t\begin{pmatrix} e_x & e_y & e_z \\ 0 & 0 & \omega \\ \sin\theta\cos\varphi & \sin\theta\sin\varphi & \cos\theta \end{pmatrix} \quad (3)$$

$$= R\delta t(-\omega\sin\theta\sin\varphi, \omega\sin\theta\cos\varphi, 0),$$

where $\delta\mathbf{r}_1 = R\omega\delta t(-\sin\theta\sin\varphi, 0, 0)$.

As we can see from (3), the displacements at the limb ($\varphi = 0, \pi$) are equal to zero, whereas those in the hemisphere closest to the observer ($\pi \le \varphi \le 2\pi$) are positive and directed along the x axis. The maximum displacements occur at the meridian passing through the observer's coordinates $\left(\varphi = \frac{3}{2}\pi\right)$.

In the case of small displacements $|\delta\mathbf{r}_1| \ll R$, the two eyes of an observer can recognize differences between the two images and reproduce the 3D image of the object. In this case, these differences are naturally perceived as two different projections (for one eye and the other). Of course, the two images are ascribed to the same time. In the case of a sphere, the third component of the image $R\sin\theta\sin\varphi = y$ can be derived starting from expression (3).

Note that y is proportional to the displacement (3), and this is true, for example, for any surface that can be written in the form

$$\mathbf{r} = R(\sin\theta\cos\varphi, \sin\theta\sin\varphi, \cos\varphi),$$

if we assume that $R = R(\theta, \varphi)$. It is evident that it is very important to orient the stereo pair so that its baseline is directed along the axis perpendicular to $\boldsymbol{\omega}$ (in the case under consideration, along the x axis).

It is known that the Sun undergoes differential rotation [8]:

$$\omega = \omega_0(1 + \epsilon\sin^2\theta), \quad (\epsilon \sim 0.2). \quad (4)$$

Thus, instead of (3), we have

$$\delta r_{1x} = -\delta t R_1\omega_0\sin\theta\sin\varphi, \quad (5)$$

where $R_1 = R(1 + \epsilon\sin^2\theta)$. Precisely this picture is actually observed in stereo pairs composed of H_α filtergrams of the chromosphere. As noted above, the stereo pairs clearly show that the solar surface is not spherical. Figure 1 presents an example of such a stereo pair obtained using computer graphics. The corresponding formulas are given in the Appendix.

3. 3D IMAGES OF CORONAL STRUCTURES

The predominant direction of coronal rays, polar plumes, and other coronal structures is usually radial. Therefore, no arrangement of them is convenient for determining their spatial distribution. In fact, we can fix only the component of displacement that is perpendicular to the ray itself and parallel to the plane of the sky.

Since the direction of a coronal ray is characterized by the vector **r**, we obtain the displacement (2); the projection of this displacement onto the plane of the sky is

$$\delta\mathbf{r}_{pr} = \delta\mathbf{r} - \mathbf{e}_y(\delta\mathbf{r}\mathbf{e}_y). \quad (6)$$

On the other hand, the projection of the ray onto the plane of the sky is

$$\mathbf{r}_{pr} = \mathbf{r} - \mathbf{e}_y(\mathbf{r}\mathbf{e}_y). \quad (7)$$

Thus, the displacement perpendicular to $\mathbf{r}_{np}$ is

$$\delta\mathbf{r}_{obs} = \delta\mathbf{r}_{pr} - \mathbf{r}_{pr}(\delta\mathbf{r}_{pr}\mathbf{r}_{pr})/(r_{pr})^2. \quad (8)$$

In a spherical coordinate system, these formulas take the form

$$\begin{aligned}\mathbf{r}_{pr} &= r(\sin\theta\cos\varphi, 0, \cos\theta)\\ \delta\mathbf{r}_{pr} &= r\omega\delta t(-\sin\theta\sin\varphi, 0, 0).\end{aligned} \quad (9)$$

After substituting these expressions into (8), we have

$$\delta\mathbf{r}_{obs} = r\omega\delta t\left\{(-\sin\theta\sin\varphi, 0, 0) + (\sin\theta\cos\varphi, 0, \cos\theta)\frac{\sin^2\theta\cos\varphi\sin\varphi}{\sin^2\theta\cos^2\varphi + \cos^2\theta}\right\}. \quad (10)$$

It follows from (10) that

$$\delta\mathbf{r}_{obs} = \frac{r\omega\delta t}{2}\frac{\sin 2\theta\sin\varphi}{\sqrt{\sin^2\theta\cos^2\varphi + \cos^2\theta}}. \quad (11)$$

It is easy to see that the effect of the displacement is maximum near the disk center, and the region of large displacements (near the maximum) is localized in a narrow zone with respect to φ and in a relatively wide zone with respect to θ. For practical purposes (i.e., determining the locations of polar plumes), we should consider $\theta \sim 30°$ and 150°, corresponding to the boundaries of polar plumes in the corona. The dependence of the displacements on longitude for these values of θ is a function that is equal to zero at the limb and slowly increases toward the equator, with a characteristic half-width $\sim\pi/4$. This behavior is probably the reason we failed in our attempt to determine the 3D structure of polar plumes. During the observation period, the region of polar plumes extended to $\theta \leq 20°$. In accordance with (11), this value is clearly insufficient to obtain a stereo effect.

4. THE INVERSE PROBLEM

Molodensky *et al.* is [5] calculation for the corona on November 3, 1994, showed that its structure is well described by a model with a thin, luminous sheet. It is known that the optical depth in the corona does not exceed 10^{-6}, so that this model seems natural. In addition, all possible efforts are undertaken in modern observations to suppress the radial component of the radiation-density gradient, in order to exclude the isotropic radiation corresponding to the hydrostatic-equilibrium component, and also to suppress the dependence of the dilution coefficient on the distance. After eliminating the radial component of the radiation-density gradient, we can see emission from a heliospheric sheet, whose structure is quite complicated. However, the emission pattern is appreciably smoother at $r > 2R_\odot$, and the inverse problem can be formulated for such distances (i.e., determining the shape of the emitting layer from its radiation). Figure 2 shows the superposition of two images: the image of the corona on June 30, 1973, obtained by Koutchmy (for distances from the limb $\leq 2R_\odot$) and an image of the outermost corona obtained by the Los Alamos National Laboratory group [9]. We can see that, at large distances, the corona (heliospheric sheet) is made up of a set of approximately radial rays.

Let us introduce a cylindrical coordinate system whose origin is at the center of the Sun, with the $z = 0$ plane coinciding with the plane of the sky. The azimuth angle is denoted by p ($0 \leq p < 2\pi$) and the distance from the current point to the Sun's center by r. Let $d(r, p)$ be the thickness of the layer, $\gamma(r, p)$ the angle between the normal to the layer and the line of sight, which coincides with the unit vector $\mathbf{e}_z$, $f(r, p)$ the layer radiation density at the point (r, p), which is known from observations, and $z = \chi(r, p)$ a function describing the shape of the layer.

We have the following relation between the introduced quantities:

$$\frac{d(r, p)}{|\cos\gamma|} = f(r, p). \quad (12)$$

Using the notation described above,

$$\cos\gamma = \frac{-\mathbf{e}_z\nabla(\chi - z)}{|\nabla(\chi - z)|},$$
$$\frac{1}{|\cos\gamma|} = |\nabla(\chi - z)| = \sqrt{1 + \left(\frac{\partial\chi}{\partial r}\right)^2 + \left(\frac{1}{r}\frac{\partial\chi}{\partial p}\right)^2}, \quad (13)$$

and, consequently,

$$d\sqrt{1 + \left(\frac{\partial\chi}{\partial r}\right)^2 + \left(\frac{1}{r}\frac{\partial\chi}{\partial p}\right)^2} = f(r, p). \quad (14)$$

As we can see in Fig. 2, the following inequality holds in almost all cases:

$$\left(\frac{\partial\chi}{\partial r}\right)^2 \ll \left(\frac{1}{r}\frac{\partial\chi}{\partial p}\right)^2.$$

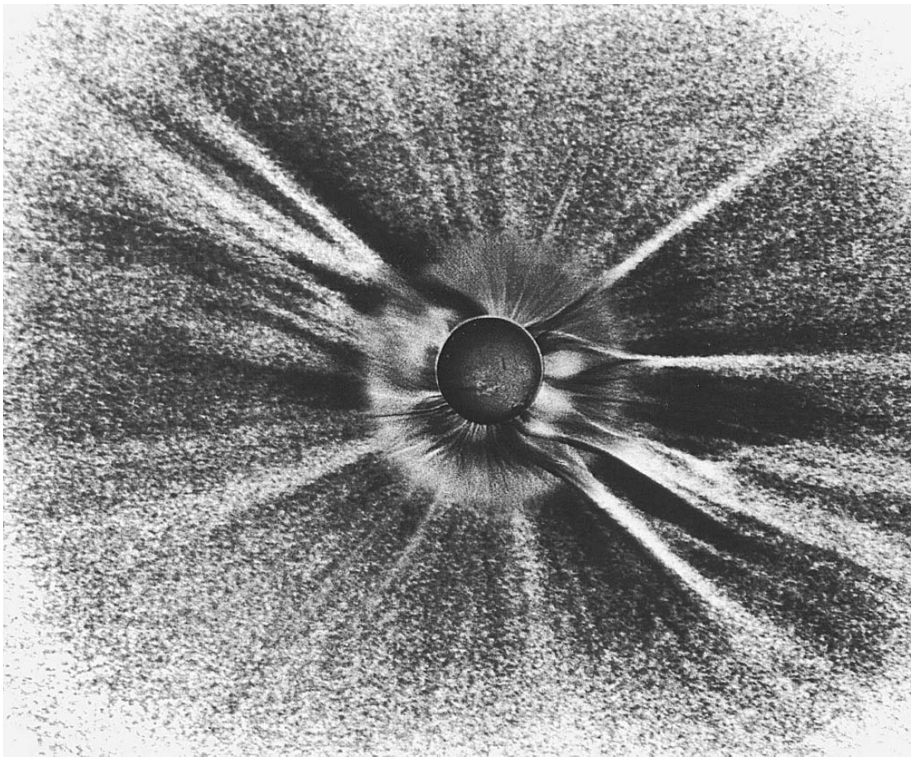

Fig. 2. Image of the corona on June 30, 1973, based on the observations of S. Koutchmy and a heliospheric sheet from observations by Keller and Liebenberg in 1981 [9].

Neglecting the derivative of χ with respect to r in the square root, we obtain equation (12) for χ with a parametric dependence on r:

$$f^2 - d^2 = \frac{d^2}{r^2}\left(\frac{\partial\chi}{\partial p}\right)^2,$$

i.e., $\partial\chi/\partial x = \sqrt{f^2/d^2 - 1}$, where $x = rp$. The solution to this equation is

$$\chi = \int\sqrt{f^2/d^2 - 1}\,dx. \qquad (15)$$

Observations [9] indicate that the number of extreme (or inflection points) is of the order of ten. Therefore, the solution turns out to be multivalued, even if we take into account the condition $\chi(r, 0) = \chi(r, 2\pi)$.

We can see in Fig. 2 that, as the distance from the limb decreases to ~$2R_\odot$, pleats and folds form in the heliospheric sheet. Consequently, beginning from this distance, expression (12) and the subsequent formulas cannot be used to solve the inverse problem.

On the other hand, as noted in the Introduction, a classical Whitney pleat can be constructed quite simply. For example, Fig. 3a depicts a fragment of a coronal helmet, and Fig. 3b shows a pleat (with appropriately chosen scales along the x and y axes). We can see that the model describes the structure well—at least the region near the helmet vertex. A three-dimensional image of the corresponding surface is presented in Fig. 3c. The correspondence between Figs. 3a and 3b follows from the fact that it is precisely the plasma on the $B_r = 0$ surface that emits efficiently, and singular points in the form of Whitney pleats form when an arbitrary smooth surface is projected onto the plane of the sky.

Another characteristic feature of the $B_r = 0$ surface is the existence of quiet prominences: The relation between the thickness, height, and length of quiet filaments is such that they are often described as "curtains" over the polarity-reversal line in the chromosphere. As a result, structures in the form of pleats can be expected under certain conditions in the filaments—namely, if a filament is observed end-on, which is possible when it is close to the limb. Figure 4a presents a filament with this orientation, and a model of the corresponding $B_r = 0$ surface is shown in Fig. 4b. The folds follow the shape of the filament, and a filament in the form of "a house of cards" is easily transformed into a smooth surface.

5. POLARIZATION OF CORONAL STRUCTURES

The general similarity between helmet shapes and Whitney pleats does not constitute unambiguous proof that the former are really projections of a smooth $B_r = 0$ surface (more precisely, a plasma sheet with increased plasma density) onto the plane of the sky. However, there is independent information about the

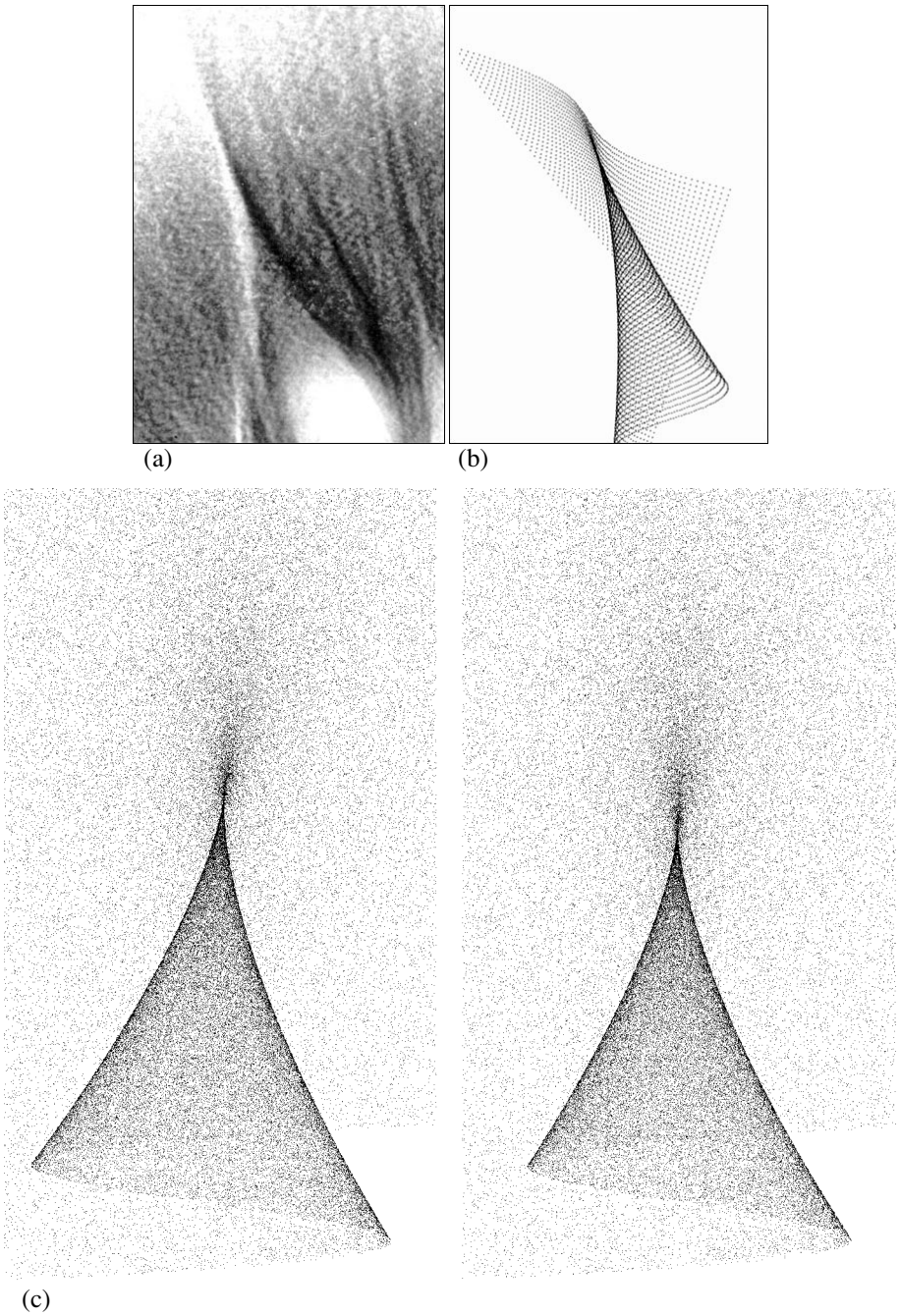

Fig. 3. (a) A fragment of a coronal helmet, (b) a pleat of the $B_r = 0$ surface, and (c) a 3D image of this pleat.

three-dimensional structure, based on the degree of polarization of the radiation.

We calculated the degree of polarization for a classical Whitney pleat (Fig. 5). The surface of the Whitney pleat was rotated about the ray axis through 60° and then inclined 30° toward the observer. The emitting layer had a constant thickness $d = 0.6$ and was illuminated by a point light source with coordinates $x = 0$, $y = -7.5$. We assumed that the light was scattered only by electrons, whose density, for simplicity, we chose to be constant. In this case, the intensity of the emission at each point of the plane of the sky is proportional to the optical depth of the plasma along the line of sight to the observer. The emission isophotes are presented in Fig. 5a and contours of the degree of polarization in Fig. 5b. We can see in Fig. 5a that the bright emission continues beyond the pleat, in the form of a diffuse ray. Figure 5b shows that the maximum degree of polarization occurs along the ray and that variations in the degree of polarization are maximum near the folds. Koutchmy *et al.* [10]

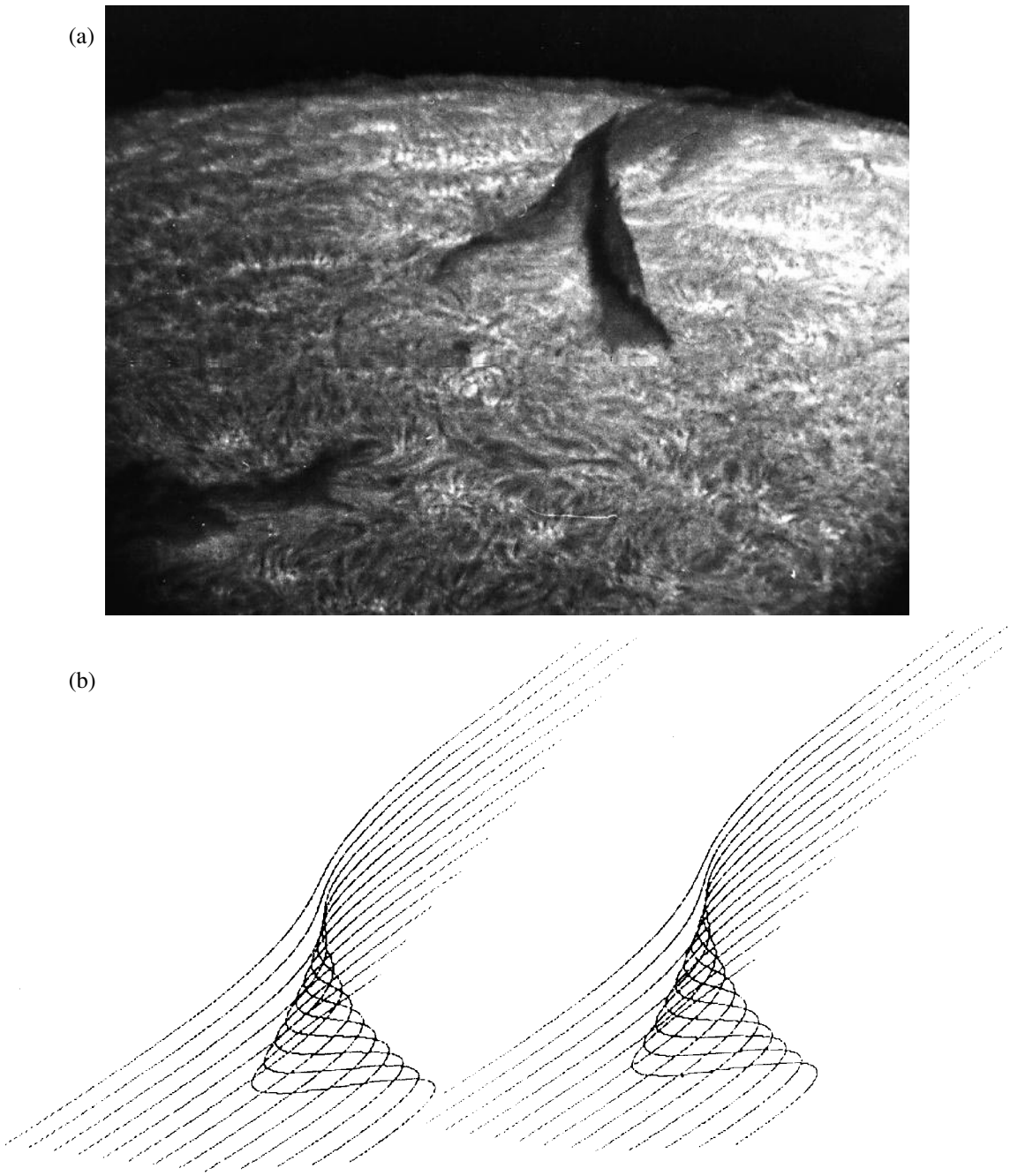

Fig. 4. (a) A quiet filament near the limb (kindly presented by V. Makarov) and (b) a model of the $B_r = 0$ surface.

obtained contours of the degree of polarization for the corona on June 30, 1973. These data show that most variations in the degree of polarization occur near the helmet vertices. Since the degree of polarization of the emission from a volume element depends on the angle of scattering of the photospheric radiation, it is evident that the maximum variation in the degree of polarization with azimuth should be associated with pleat points.

The aim of the calculations presented in Figs. 5a and 5b is to compare the emission of a pleat with observational data. At the same time, the inverse problem can be formulated for the model described above, namely, to determine the shape of the $B_r = 0$ surface from the distribution of the degree of polarization on the plane of the sky. This problem is similar to that considered in Section 4. The only difference is that calculation of the surface shape does not depend on our assumptions about the distribution of density and thickness in the emitting layer.

In fact, if we directly associate the variations in density and thickness of the layer in the problem from Sec-

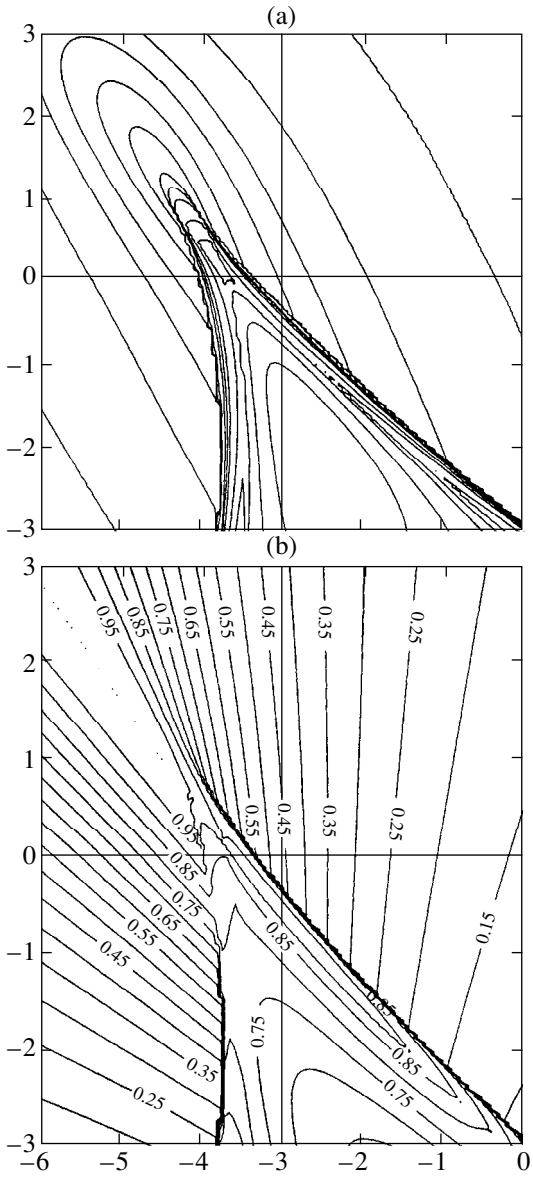

Fig. 5. (a) Isophotes of the region near a pleat for a sheet with finite thickness and (b) contours of the degree of polarization for the same model. The Sun's center is at the point $x = 0$, $y = -7.5$. The axis of the helmet is radial, lies in the meridional plane 60° to the east of the central meridian and is directed at an angle $\varphi = 60°$ to the equatorial plane *XZ*. In both cases, the thickness of the emitting layer is 0.6.

tion 4 with the derivative of χ with respect to the angular coordinate [see expression (15)], the degree of polarization describes the deviation of an element of the emitting region from the plane perpendicular to the line of sight and passing through the center of the Sun. Below, we consider examples corresponding to both problems.

(1) Let photometric sections of the ray structure in azimuth at a distance of ~$2R_\odot$ from the limb (Fig. 2) be described by the functions $f(x) = [1 + (a_i^2 + x^2)^{-2}]^{1/2}$, where, as in the above formulas, $x = rp$, p is the azimuth angle, and a_i are constants. Figure 6a shows the corresponding family of curves f_i for $a_i = 0.3$, 0.5, and 0.7. Substituting this expression for $f(x)$ into (15) and integrating yields $\chi_1 = \int \frac{dx}{a_i^2 + x^2} = \frac{1}{a_i}\arctan\frac{x}{a_i}$. The corresponding curves are presented in Fig. 6b. The set of photometric sections f_i can be identified with the neighborhood of the Whitney pleat: The section nears the pleat when a_i^2 decreases and is discontinuous at the point $x = 0$ when $a_i = 0$. The corresponding shape of the layer is given by the function $\chi_1(x)$, which is a solution of equation (14). In the vicinity of the point $x = 0$, the curve tends to become steeper as a^2 decreases; when $a \longrightarrow 0$, $f_1(x)$ becomes discontinuous when the line of sight is tangent to the $B_r = 0$ surface.

(2) Koutchmy, Picat, and Dantel [10] solved the second problem in general form and obtained a numerical solution for the entire structure of the corona on November 3, 1994. Let us consider an analytical model for the neighborhood of a Whitney pleat. The following relation was used in [10] (see formula (4) in that paper):

$$P = P_{\max}\left(1 - k\frac{\chi_2^2}{r^2} + \ldots\right), \qquad (16)$$

where P is the degree of polarization in the K corona, χ_2 is the deviation of an element of the emitting layer from the plane of the sky, $P_{\max}$ is the maximum degree of polarization a given distance r from the Sun's center (in the same plane), and k is a coefficient that depends only on r. It follows from (16) that

$$\chi_2 = \pm\frac{r}{\sqrt{k}}(P_{\max} - P)^{1/2}. \qquad (17)$$

The two signs in front of the square root in the above expression correspond to the two possibilities for the surface $\chi_2 > 0$ and $\chi_2 \le 0$. We have no way to determine the sign of χ_2 based only on polarization observations.

In the case of Thomson scattering of photons by electrons in the corona, the maximum degree of polarization $r = 2R_\odot$ from the limb is $P_{\max} = 0.8$ [11]. A map of the degree of polarization of the corona on June 30, 1973 (the most reliable measurement among those known to us), is presented in [10]. The degree of polarization in a ray at the northwest limb changes continuously from 0.12 to 0.28 as the azimuth changes by several degrees of arc (~5°–10°) [10]. In accordance with the above considerations, let us substitute $P_{\max} = 0.8$, $P = 0.20 + 0.08\tanh\frac{x}{a_i}$, $a_i = 1.0$, 0.3, and 0.1 into (17), where, as before, $x = rp$, p is the azimuth angle, and a and c are two constants, with a corresponding to the steepness of χ_2 and c to the amplitude of the deviation

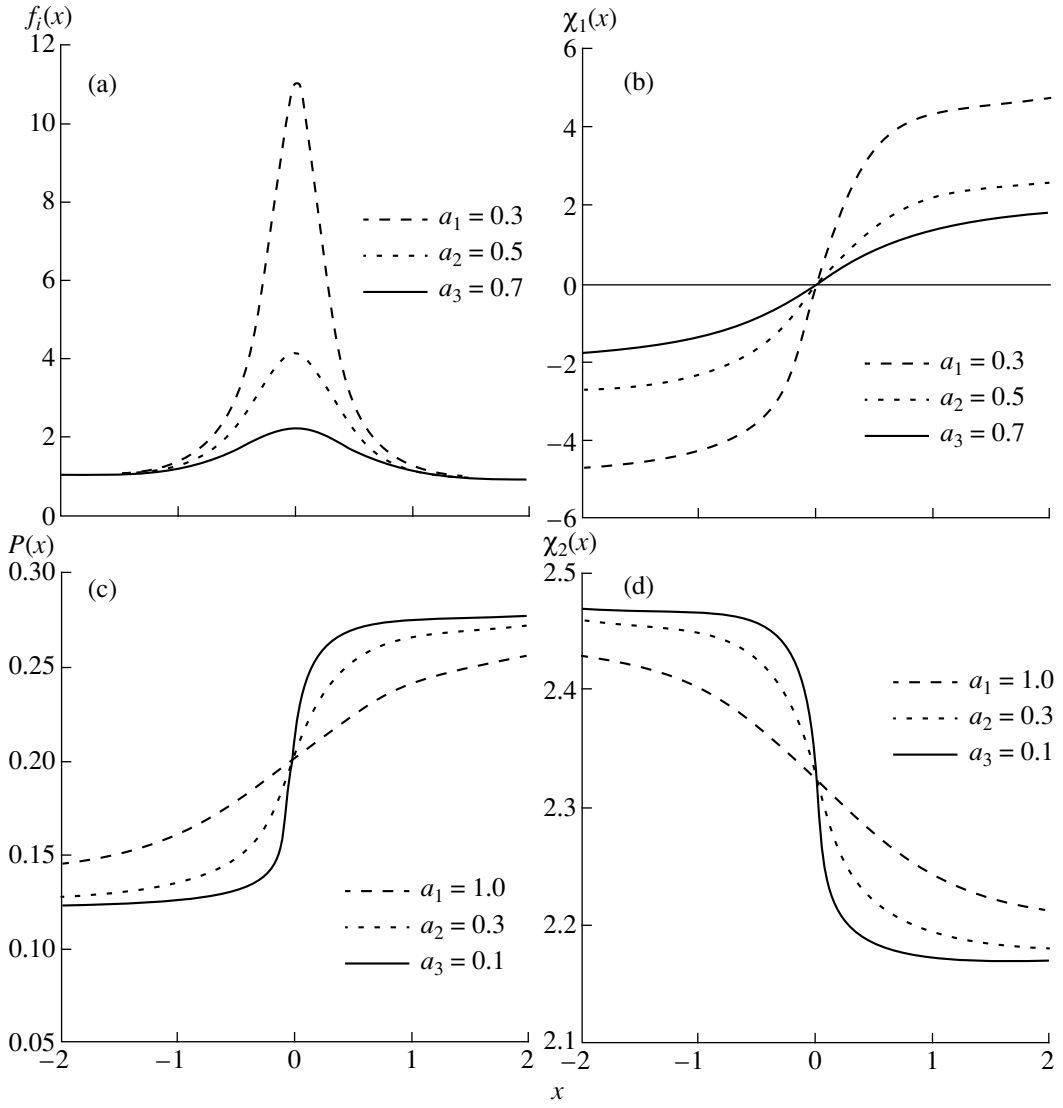

Fig. 6. (a) A set of model sections for a coronal ray, (b) shape of the emitting layer derived from these distributions, (c) approximation of the distributions of the degree of polarization near the axis of the coronal ray in the northwest region of the corona on June 30, 1973 [10], and (d) shape of the emitting layer derived from the above distributions.

of χ_2 from the plane of the sky. These curves are drawn in Figs. 6c and 6d.

Thus, both formulations of the problem of finding the $B_r = 0$ surface that determines the structure of coronal rays lead to qualitatively very similar functions $\chi(x)$ near the pleat: In both cases, the surface is represented by a function whose rate of growth increases as we approach the pleat.

6. CONCLUSION

The above considerations connected with the three-dimensional structure of basic coronal helmet formations (namely, the structure of folds and pleats and comparison with observations, including polarization data) are supported by some other data. It has been shown that heliospheric sheets possess not only radial folds but also folds that considerably deviate from the radial direction. The structure of the corona on November 3, 1994, is well described by the folds of the sheet reconstructed by Molodensky *et al.* [5] from synoptic-map data for this date.

However, there are direct observations that could lead to fundamentally new results. Observations using a long baseline between two spacecraft are currently being planned. If this baseline is such that the angle between the two spacecraft with its vertex at the Sun's center is of the order of a radian, then, in addition to observations of the stereo effect for individual structures in the solar atmosphere and for the entire Sun, we should be able to obtain direct information about the nature of helmets, polar plumes, and coronal rays.

Simultaneous observations from different points will give a genuine stereo effect (compared to the quasi-stereo effect obtained via the rotation of the object observed) and will enable us to distinguish folds and pleats of the $B_r = 0$ surface from real, dense plasma structures in some ray-like objects.

This last possibility is connected with the fact that there is a fundamental difference between observations of folds (and pleats) using small and large baselines. It is known [6] that pleats and folds are stable with respect to small perturbations of the surface itself and small variations in the direction of projection of the surface onto the plane of the sky. (In particular, this is why it is possible to construct stereo images of a surface.) However, in the case of large angles (~1 rad), such projections are considerably different: Pleats and folds disappear in some places and appear in others. This behavior can provide proof that a structure under consideration represents a fold of a smooth curved surface, rather than a local increase in the plasma density. Therefore, observations using multiple spacecraft can answer several important questions about the nature of coronal structures.

ACKNOWLEDGMENTS

This work was supported by the Russian Foundation for Basic Research (project code 99-02-16360). We are grateful to V.I. Makarov and B.A. Ioshpa for the presented H_α filtergrams and to M.A. Livshits for useful comments.

APPENDIX

If we have two images of the Sun separated by a small time interval ($t \sim 1$ day), after certain transformations, we can construct a single stereo image [7]. We can formulate two problems: determinating the direction for the baseline of the stereo image and taking into account the inclination of the rotation axis with respect to the ecliptic plane. We shall consider both these problems.

(1) Let us have two photoheliograms with small features (e.g., spots). The coordinates of spots i in the first photoheliogram are

$$\mathbf{r}_i = (x_i, y_i, \sqrt{1 - x_i^2 - y_i^2}), \tag{A1}$$

where $R_\odot = 1$.

After the Sun has rotated through a small angle $\Omega t = w \gg 1$, the spatial displacement of the spots is $[\mathbf{w}\mathbf{r}_i]$, and the coordinates of the shifted spots are determined by the vector

$$\mathbf{r}_i' = \mathbf{r}_i + [\mathbf{w}\mathbf{r}_i]. \tag{A2}$$

The centers of the two photoheliograms can be superimposed quite accurately, but the directions of their equators aligned only approximately. We denote the small residual angle resulting from the superposition of the equators in the two photoheliograms φ. Then, the total displacement $\delta\mathbf{r}_i = \mathbf{r}_{2i} - \mathbf{r}_i$ is

$$\delta\mathbf{r}_i = \varphi[\mathbf{e}_z\mathbf{r}_i'] + [\mathbf{w}\mathbf{r}_i]. \tag{A3}$$

Neglecting the product of the two small angles φw in the first term on the right-hand side, we can rewrite (A3) in the form

$$\delta\mathbf{r}_i = [(\mathbf{w} + \mathbf{e}_z\varphi)\mathbf{r}_i]. \tag{A4}$$

The same relation will be valid for spot k. Taking the x and y components of (A4) and adding the z component for spot k, we obtain a system of three equations for $\mathbf{w} + \mathbf{e}_z\varphi$:

$$\begin{aligned} w_y z_i - (w_z + \varphi) y_i &= \delta r_{ix}, \\ (w_z + \varphi) x_i - w_x z_i &= \delta r_{iy}, \\ w_x y_k - w_y x_k &= \delta r_{kz}, \end{aligned} \tag{A5}$$

whose determinant is equal to

$$\mathrm{Det} = \begin{pmatrix} 0 & z_i & -y_i \\ -z_i & 0 & x_i \\ y_k & -x_k & 0 \end{pmatrix} = z_i(x_i y_i - x_k y_i). \tag{A6}$$

As we can see from (A6), this system of equations is soluble if $z_i \neq 0$ (i.e., spot i is not located at the limb), and if $\dfrac{x_i}{x_k} \neq \dfrac{y_i}{y_k}$ (i.e., spots i and k are not located at the same diameter). In this case, the unknown variables in (A5) can be found in the form

$$\begin{aligned} w_x\mathrm{Det} &= \delta r_{ix} x_i x_k + \delta r_{kz} z_i x_i + \delta r_{iy} y_i x_k, \\ w_y\mathrm{Det} &= \delta r_{ix} x_i y_k + \delta r_{kz} z_i y_i + \delta r_{iy} y_i y_k, \\ (w_z + \varphi)\mathrm{Det} &= -\delta r_{ix} z_i x_k + \delta r_{kz} z_i^2 + \delta r_{iy} z_i y_k. \end{aligned} \tag{A7}$$

The direction of the stereo-pair baseline is determined by the expression $\tan\beta = w_y/w_x$, where the angle β is measured from x axis. Note that (A3) yields different values of w for features at different heliographic latitudes; therefore, they should be denoted by the indices i and k. The remaining two equations of the form (A4) for the i components of spot k together with z component of spot i also form a system of three equations in $\mathbf{w}_k + \mathbf{e}_z\varphi$. If we make the exchange $i \longleftrightarrow k$, this system of equations coincides exactly with (A4), and we can immediately obtain its solution from (A7). Thus, we obtain a solution to the first problem formulated above.

(2) Since the angle between the line of sight and the solar rotation axis is known, and its maximum difference from 90° is 7.5°, $|w_z| \approx |w|$. The dependence of w on θ is also known [in accordance with the law of differential rotation $\Omega = \Omega_0(1 + 0.2\sin^2\Theta)$]. Therefore, from (A5), we can find φ—the angle by which the second photoheliogram is rotated with respect to the first one. By rotating it through an angle $-\varphi$, we obtain the

required stereo image if $w_z = w$ during the observation period.

Finally, using computer graphics, we can introduce a correction for the case $w_z \neq w$. The coordinates of all points in both images must be displaced by the vector $-w_z[\mathbf{e}_x\mathbf{r}_i]$ projected onto the *xy* plane:

$$\delta\mathbf{r}_i'' = -w_z[\mathbf{e}_z[[\mathbf{e}_x\mathbf{r}_i]\mathbf{e}_z]] = \mathbf{e}_y w_z\sqrt{1 - x_i^2 - y_i^2}. \quad \text{(A8)}$$

This yields a solution to the second problem formulated above.

REFERENCES

1. A. A. Vedenov, Usp. Fiz. Nauk **164**, 967 (1994).
2. A. A. Vedenov, J. Tech. Phys. Polish Acad. Sci. **38**, 349 (1997).
3. S. Koutchmy and M. Molodensky, Nature **360**, 717 (1992).
4. K. Saito, Ann. Tokyo Aston. Obs. Second Series **XII** (2), 53 (1970).
5. M. M. Molodensky, L. I. Starkova, S. Koutchmy, *et al.*, *Solar Drivers of Interplanetary and Terrestrial Disturbances*, ASP Conf. Ser. **95**, 385 (1996).
6. V. I. Arnold, *Mathematical Methods of Classical Mechanics*, 2nd ed. (Springer, New York, 1989; Mir, Moscow, 1989).
7. D. Batchelor, Solar Phys. **155**, 57 (1994).
8. C. W. Allen, *Astrophysical Quantities* (The Athlone, London, 1973; Mir, Moscow, 1977).
9. C. F. Keller and D. Liebenberg, Los Alamos Science **2**, 4 (1981).
10. S. Koutchmy, J. Picat, and M. Dantel, Astron. Astrophys. **59**, 349 (1977).
11. S. Koutchmy and K. Schatten, Solar Phys. **17**, 117 (1971).

Translated by Yu. Dumin

Astronomy Reports, Vol. 44, No. 2, 2000, pp. 122–137. Translated from Astronomicheskiĭ Zhurnal, Vol. 77, No. 2, 2000, pp. 144–160.

Effects of Instability of the Earth and Celestial Coordinate Systems on Earth Orientation Parameters

V. E. Zharov, M. V. Sazhin, and N. A. Chuĭkova

Sternberg Astronomical Institute, Universitetskiĭ pr. 13, Moscow, 119899 Russia

Received December 23, 1998

Abstract—Unknown secular and long-term changes in the Earth orientation parameters attributed to instability (possible rotation) of both the Earth and celestial coordinate systems (ECS and CCS) are studied. Rotation of the CCS due to changes in the coordinates of extragalactic sources resulting from gravitational lensing can lead to errors of the order of several microarcseconds in the orientation parameters. The rotation of the ECS due to the crust pressing on the mantle diminishes the tidal retardation of the Earth's rotation and produces long-term variations in the duration of the day (with a period of about 1500 years) and in the motion of the pole relative to the Earth's surface. *© 2000 MAIK "Nauka/Interperiodica".*

1. INTRODUCTION

One of the main goals of astrometric observations is determining the Earth and celestial coordinate systems (ECS and CCS, respectively) and their mutual positions as a function of time, determined by the Earth orientation parameters (precession, nutation, polar motion, and angular rotation). The correctness of interpretations of observations in astrometry and geodesy, as well as in other Earth sciences (celestial mechanics, stellar astronomy, geodynamics, geophysics, space navigation, etc.) relies on the precision of such measurements. Since January 1, 1998, the CCS has been defined by the *RSC(WGRF)95R01* catalog [1], which contains the J2000.0 coordinates for 608 extragalactic sources. The geocentric rectangular coordinates of more than 500 stations at 290 observation points define the ECS [2].

The ECS and CCS are of fundamental importance for theories of precession and nutation and studies of geotectonics and deformations of the Earth's crust, as well as for space geodesy and navigation. To ensure correct interpretation of determinations of the Earth rotation parameters, deformations of the Earth's surface, etc. with precision 0.1 milliarcsecond (mas) or better, the errors in the realizations of the ECS and CCS must be below this level. Since the specification of the CCS and ECS is fundamental to this work, Section 2 briefly summarizes the basic definitions of both systems adopted by the International Earth Rotation Service (IERS).

Achievement of the necessary precision requires the use of modern observing techniques such as Very Long Baseline Interferometry (VLBI), global positioning systems (GPS), laser range finders, and so on. Observations performed over the last 15 years have demonstrated that the theories for the Earth's precession and nutation adopted by the International Astronomy Union in 1980 have very poor accuracy.

If the CCS and ECS are well defined and stable, it is sufficient to know the three angles Ψ, Φ, and Θ (Fig. 1) in order to make a transformation from one coordinate system to the other. However, astrometry traditionally treats this transformation as the multiplication of several matrixes [4]:

$$\mathbf{r}_{\mathrm{CCS}} = PNSR\mathbf{r}_{\mathrm{ECS}}, \quad (1)$$

where P is the precession matrix, which depends on the three angles z_A, θ_A, and ζ_A, which determine the positions of the average equinox and equator on a given date relative to the average equinox and equator of the starting epoch; N is the nutation matrix, which consists of the three matrixes

$$N = R_1(-\epsilon_A)R_3(\Delta\psi)R_1(\epsilon_A + \Delta\epsilon),$$

where ϵ_A is the inclination of the ecliptic to the equator for epoch J2000.0; and $\Delta\psi$ and $\Delta\epsilon$ are the nutation components in longitude and inclination.

The matrix S describes the Earth's diurnal rotation about the axis OP_t, to which the ECS x, y, z are fixed. The OP_t axis is called the celestial ephemeris pole, and, in general, differs from the axis of the Earth's figure. The coordinates of the point P_t in the ECS are called the coordinates of the pole x_p, y_p. Then,

$$S = R_3(-\mathrm{GST}), \quad R = R_1(y_p)R_2(x_p),$$

where GST is Greenwich sidereal time and the rotation matrixes R_1, R_2, and R_3 denote a rotation by an angle α about the axes x, y, and z, respectively, so that

$$R_1(\alpha) = \begin{pmatrix} 1 & 0 & 0 \\ 0 & \cos\alpha & \sin\alpha \\ 0 & -\sin\alpha & \cos\alpha \end{pmatrix},$$

1063-7729/00/4402-0122$20.00 © 2000 MAIK "Nauka/Interperiodica"

$$R_2(\alpha) = \begin{pmatrix} \cos\alpha & 0 & -\sin\alpha \\ 0 & 1 & 0 \\ \sin\alpha & 0 & \cos\alpha \end{pmatrix},$$

$$R_3(\alpha) = \begin{pmatrix} \cos\alpha & \sin\alpha & 0 \\ -\sin\alpha & \cos\alpha & 0 \\ 0 & 0 & 1 \end{pmatrix}.$$

The motion of the ECS with respect to the inertial reference frame *X*, *Y*, *Z* (Fig. 1) is described by the adopted nutation and precession theories.

It follows from transformation (1) that, first, the observations determine the position of the celestial ephemeris pole but not the instantaneous axis of the Earth's rotation, and, second, there must be some relations between the angles, since there are more angles than formally required. Therefore, the observations can determine the Earth's orientation but not the origin (external or internal) of a change in orientation. In other words, a possible rotation of the ECS or CCS can be interpreted either as an inaccuracy of the precession theory or as a correction to Universal Time, for example (see Section 3).

The real position of the celestial ephemeris pole P_0 differs from its theoretical position P_t due to errors in the precession and nutation theories. Since the duration of the series of VLBI observations is about 15 years, it is usual to attribute the difference between P_0 and P_t to errors in the nutation theory and to find corrections to the nutation in longitude $\delta(\Delta\psi)$ and inclination $\delta(\Delta\epsilon)$. Estimates of a linear trend—i.e., corrections to the lunar–solar precession—are possible in this case only on the basis of some theoretical reasoning [5]. Measurements of $\delta(\Delta\psi)$ and $\delta(\Delta\epsilon)$ form the basic material for constructing new nutation theories.

In our work, we present a theory for instability (i.e., possible rotation) of the CCS and ECS that has thus far been neglected in theories of precession and nutation. We study new long-term and secular changes in the parameters relating the CCS and ECS, both of which can rotate (see Sections 4–6).

The rotation of the CCS due to weak gravitational lensing (gravitational refraction) of the light of the reference sources by stars and dark Galactic bodies can lead to detectable changes in their coordinates [6], comparable with the precision of VLBI observations. Since the distribution of the reference radio sources is not uniform and the Galactic gravitational field is not stationary, rotations of the CCS are possible [7]. Since the CCS is assumed to be stable, rotations of the CCS can be interpreted as errors in the precession theory. The expected rotation of the CCS due to gravitational refraction is calculated in Section 4.

The reason for the rotation in the ECS is that existing theories for the Earth's rotation are constructed based on the Tisserand axes for the Earth's mantle [8]. In practice, these coordinate axes are taken to be the Tisserand axes for the Earth's crust (there must be no components of the total rotation in the velocities of stations on the Earth's surface). However, long-term variations in the Earth's rotation can include the effects of presumed rotation of the crust with reference to the mantle, due to the boundary layer of reduced viscosity between them. Therefore, the rotation of the crust with respect to the mantle produces a rotation of the Tisserand axes, which is usually not reflected in theories of the Earth's rotation. Sections 5 and 6 present the mathematical basis for this hypothesis, some estimates of the expected effect, and a comparison of the theory with astronomical observations.

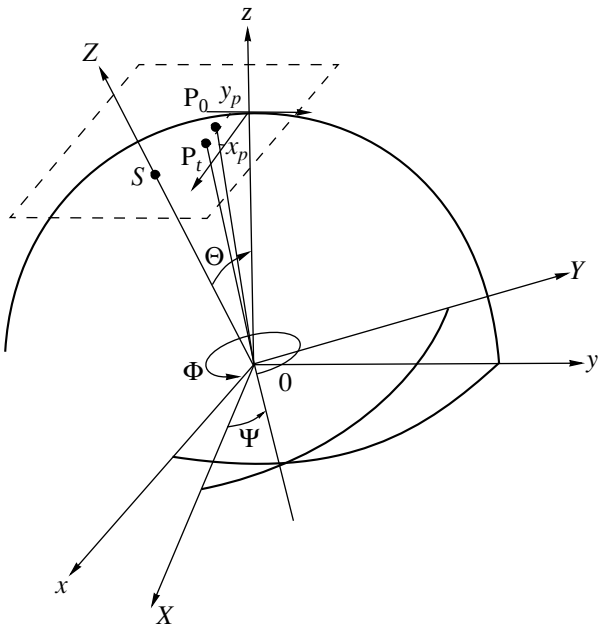

Fig. 1. Orientation of the Earth coordinate system *xyz* with respect to the celestial coordinate system *XYZ*.

Section 7 presents a discussion of our results.

2. DEFINITIONS OF THE EARTH AND CELESTIAL COORDINATE SYSTEMS

An ideal celestial system of coordinates should be inertial. However, the concept of an inertial coordinate is rather formal and abstract. In practice, we work with a quasi-inertial system that can be assumed to some accuracy to be inertial over a given time interval in a given region of space. The coordinates of celestial bodies assumed to be stationary or moving with respect to the CCS in accordance with an accurate theory can provide a practical realization of the CCS.

Since January 1, 1998, the CCS has been defined by the coordinates of 608 sources that determine the equator and equinox for epoch J2000.0 (the *RSC(WGRF)95R01* catalog). The coordinates of these sources with respect to

reference systems were calculated via VLBI observations by an IAU working group on reference systems [1].

Another realization of the CCS is provided by the *RSC(IERS)95C02* catalog [9], in which VLBI catalogs of radio sources independently obtained by various groups were used to calculate the source coordinates. It is shown in [1] that these two systems are equivalent to within less than 20 μarcsec. The axes of each system are stable to within 20 μarcsec. Thus, this defines the current precision of the CCS.

The origin of the CCS is at the barycenter of the solar system, and the directions of its axes are fixed by the coordinates of quasars. The x axis is defined by the right ascension of the quasar 3C273B ($12^h29^m6\overset{s}{.}6997$) for epoch J2000.0 [10]. On average, the errors in the source coordinates are 0.2 mas [1]. The stability of the CCS is limited by the proper motions of individual sources. The term "proper motions" is used to describe changes in the right ascensions and declinations of the sources due to changes in their structure and variability. The coordinates of some sources (P0528+134, P0823+033, and others) vary by several tenths of mas per year [11]. These sources are included in the catalog for use in space navigation and also in order to study their proper motions via comparison of their coordinates with those of "stationary" sources. In addition, increasing the number of sources provides a more uniform distribution of sources over the celestial sphere.

To increase the stability of the system, so-called defining sources are used. These sources have been observed over a long time and have no appreciable structure. Therefore, their coordinates are determined with the highest precision.

The Cartesian coordinate system of the Earth (i.e., fixed to the Earth's body in some well-defined way) is specified by the positions of observing stations, whose coordinates are known to within about 1 cm. The center of the ECS coincides with the center of mass of the Earth, including the oceans and atmosphere. If the Earth were an absolutely rigid body, every mass element dM with radius vector $\mathbf{r}$ would rotate with the same angular velocity $\mathbf{\Omega}$ in an inertial coordinate frame. The velocity of this element in space would be $d\mathbf{r}/dt = \mathbf{\Omega} \times \mathbf{r}$. In this case, the ECS could be chosen arbitrarily, though it would be reasonable to direct the axes along the main inertial axes of the Earth.

Since the Earth can deform, the velocity of each element consists of its rotation velocity and deformation velocity $\mathbf{v}$:

$$d\mathbf{r}/dt = \mathbf{\Omega} \times \mathbf{r} + \mathbf{v}.$$

In accordance with elasticity theory, the deformation velocity field $\mathbf{v}$ is equivalent to rotation of the body with some angular velocity [8]. There is only one coordinate system that can distinguish between rotation and deformation: a system of Tisserand axes. The velocity field $\mathbf{v}$ determines the relative angular momentum

$$h = \int_V \mathbf{r} \times \mathbf{v} dM,$$

where V is the deformed volume of the Earth. The Tisserand axes are defined by the condition $h = 0$ or $\int_V \mathbf{v}^2 dM = \min$ [8]. If V is the volume occupied by the crust and mantle, the condition $h = 0$ determines the Earth's rotation vector $\mathbf{\Omega}$ with respect to the Tisserand axes for the mean mantle [12].

Thus, to determine the ECS, in addition to the coordinates of observing stations, we must know the stations' velocities due to plate motions, as well as to tidal and compressional deformations. The velocities of the stations are known to within 3 mm/yr, on average.

According to the IERS [4], the ECS axes are defined to be the Tisserand axes for the crust; i.e., it is assumed that the ECS does not rotate with respect to the crust. If we suppose that the Earth's crust and mantle are rigidly connected, there is no difference between these two systems. However, geophysical data provide evidence for significant changes of the crustal rocks at the Mohorovicic discontinuity (the boundary between the crust and mantle). This suggests the presence of a thin layer of reduced viscosity separating the crust and mantle [13], with tangential motions along this layer being possible.

3. INSTABILITY OF THE CCS AND ECS AND ITS EFFECT ON THE EARTH ORIENTATION PARAMETERS

Let us assume that the CCS rotates over the time interval between two epochs t_1 and t_2 and that the relation between these two CCS's takes the form

$$[\mathrm{CCS}](t_2) = R_1(\alpha_1)R_2(\alpha_2)R_3(\alpha_3)[\mathrm{CCS}](t_1).$$

The ECS suffers a similar rotation

$$[\mathrm{ECS}](t_2) = R_1(\beta_1)R_2(\beta_2)R_3(\beta_3)[\mathrm{ECS}](t_1).$$

If we assume when transforming the ECS to the CCS using (1) that precession and nutation do not change between the epochs, a rotation in the CCS and ECS yields changes in all the Earth orientation parameters [14]:

$$\begin{aligned} \delta x &= \beta_2 - \alpha_1 \sin\theta + \alpha_2 \cos\theta, \\ \delta y &= \beta_1 + \alpha_1 \cos\theta + \alpha_2 \sin\theta, \\ k\delta(\mathrm{UT1}) &= -\beta_3 + \alpha_3, \\ \delta(\Delta\psi) &= \alpha_2 / \sin\epsilon_A, \\ \delta(\Delta\epsilon_A) &= -\alpha_1, \end{aligned} \qquad (2)$$

where θ is sidereal time and k is the factor for converting from universal time to sidereal time. Thus, a rota-

tion of the ECS yields a constant shift while a rotation of the CCS leads to diurnal variations in the polar motion. Universal time will be also shifted, but we will not be able to distinguish between a rotation of the CCS or ECS. The position of the celestial ephemeris pole will likewise be shifted by a constant amount determined by the rotation of the CCS.

A change in the precession is equivalent to a rotation of the ECS. This point is considered in [8] in detail. The relation between the new and old ECS's is expressed by a small rotation around the *Oz* axis and can be mathematically described as a shift in the zero of longitude. Changes in the polar motion are expressed by the appearance of diurnal components, whose amplitude linearly grows with time, and also by changes in Universal time UT1 with a constant rate.

Let us now consider possible origins of rotation of the CCS.

4. MICROSECOND INSTABILITY OF THE CCS

We will explain based on simple arguments the main origins of possible rotation of the CCS. In astronomy, a reference frame is realized by some number of astronomical reference objects, with the physical times of their observations being fixed in a given time system. The modern reference frame uses extragalactic radio sources (quasars and radio galaxies) with small transverse velocities as reference objects, thereby minimizing the rotation of the coordinate frame due to their proper motion in space. The light from quasars moves along curved trajectories determined by the gravitational fields of bodies in our Galaxy. Since the motion of these bodies consists of the regular motion around the Galactic center and peculiar motions, the pattern of the gravitational fields is not stationary. Consequently, the trajectory of light from a quasar to the observer also becomes nonstationary. The position of the quasar in the sky fluctuates. The r.m.s. of these fluctuations of quasar positions corresponds to a certain fundamental limit in the precision of quasar coordinates. We will consider the effect of the gravitational fields of stars on the apparent positions of quasars, though the contribution of the gravitational fields of dark bodies in the Galaxy could play a larger role [15].

4.1. Changes in quasar coordinates due to gravitational refraction. The gravitational field of a body (lens) B bends trajectories of light rays from a source S passing nearby it. Therefore, in this case, the direction of the arrival of the light does not coincide with the line connecting the source and observer; i.e., the apparent position of the quasar S_a differs from its true position B. The proper motion of the body S_t changes the angular distance between S_t and B, which is observed as a change in the apparent position S_a of the quasar on the celestial sphere.

Let us consider this effect in more detail. The theory of gravitational lensing (see, for example, [16]) shows that the equation for a spherically symmetrical point lens has two real roots:

$$\varphi_1 = \frac{1}{2}\varphi + \frac{1}{2}\sqrt{\varphi^2 + 4\varphi_e^2}, \quad (3)$$

$$\varphi_2 = \frac{1}{2}\varphi - \frac{1}{2}\sqrt{\varphi^2 + 4\varphi_e^2}, \quad (4)$$

where φ is the angular distance between the body B and the true position of the source S_t, and φ_e is the angle of the Einstein cone, determined by the expression

$$\varphi_e^2 = \frac{4GM_b}{c^2}\frac{L_{bs}}{(L_{bs}+L_{ob})L_{ob}},$$

where G is the gravitational constant, c the speed of light, M_b the mass of the body B, and L_{bs} and L_{ob} the distances from the quasar to the star and from the star to the observer, respectively. The lensing results in two images of the quasar S_1 and S_2, with the angular distances between them and the source S being φ_1 and φ_2.

For weak refraction, when $\varphi > \varphi_e$, the intensity of the second image is much weaker than that of the first image. Therefore, we will assume that the second image is not observed. Further, in order to preserve a unified set of notations, we denote the angular distance between the apparent position of the quasar and the star $\varphi_a = \varphi_1$.

To determine the difference between the apparent (α_a, δ_a) and true (α_t, δ_t) coordinates of the quasar, we use equation (3) and the sine theorem for spherical astronomy:

$$\frac{\sin\varphi_a}{\sin(\alpha_a - \alpha_b)} = \frac{\cos\delta_b}{\sin\gamma}, \quad (5)$$

$$\frac{\sin(\varphi_a - \varphi)}{\sin(\alpha_a - \alpha_t)} = \frac{\cos\delta_t}{\sin\gamma}, \quad (6)$$

where γ is the angular distance connecting the quasar and the star B with coordinates (α_b, δ_b). Let the difference between the apparent and true right ascensions of the quasar be $\Delta\alpha = \alpha_a - \alpha_t$ (and similarly for the difference in declinations $\Delta\delta = \delta_a - \delta_t$). For a small angle $\Delta\alpha$—i.e., $\sin\Delta\alpha \approx \Delta\alpha$—we obtain from (6)

$$\sin\gamma = \Delta\alpha\frac{\cos\delta_t}{\sin(\varphi_a - \varphi)}.$$

We find from expression (3) $\varphi_a - \varphi = \varphi_e^2/\varphi_a$. Substituting $\sin\gamma$ into (5) yields

$$\Delta\alpha \approx \frac{\sin(\varphi_e^2/\varphi_a)}{\sin\varphi_a}\frac{\cos\delta_b}{\cos\delta_a}\sin(\alpha_a - \alpha_b).$$

Table 1. Coordinates of quasars and stars

Source	Right ascension	Declination	Errors		Classification	z φ_a, arcsec	m
			10^{-6} s	10^{-6} arcsec			
0007+106	$0^h10^m31.005871^s$	10°58′29.50408″	18	420	G	0.090	15.4
	0 10 31.010	10 58 29.857				0.278	14.7
0111+021	1 13 43.144949	2 22 17.31639	14	380	A	0.047	16.3
	1 13 43.127	2 22 17.750				0.556	13.8
0735+178	7 38 7.393743	17 42 18.99868	3	50	L	>0.424	16.2
	7 38 7.374	17 42 18.968				0.278	14.3
0912+297	9 15 52.401619	29 33 24.04293	17	340	L		16.4
	9 15 52.405	29 33 23.549				0.482	15.3
	9 15 53.940	29 32 40.016				48.387	11.3

Classifications: G = galaxy, L = BL Lac, A = other.

Since $\sin(\varphi_e^2/\varphi_a)/\sin\varphi_a \approx (\varphi_e/\varphi_a)^2$, we obtain

$$\Delta\alpha = \left(\frac{\varphi_e}{\varphi_a}\right)^2 \frac{\cos\delta_b}{\cos\delta_a}\sin(\alpha_a - \alpha_b). \quad (7)$$

We can find the shift of the quasar in declination using the following equations for spherical astronomy:

$$\sin\delta_t = \cos(\varphi_a - \varphi)\sin\delta_a + \sin(\varphi_a - \varphi)\cos\delta_a\cos\gamma,$$

$$\sin\delta_b = \cos\varphi_a\sin\delta_a + \sin\varphi_a\cos\delta_a\cos\gamma.$$

The first equation yields

$$\Delta\delta \approx -\frac{\varphi_e^2}{\varphi_a}\cos\gamma.$$

Eliminating $\cos\gamma$ using the second equation, we obtain the declination shift of the quasar

$$\Delta\delta \approx -\left(\frac{\varphi_e}{\varphi_a}\right)^2 \frac{\sin\delta_b - \cos\varphi_a\sin\delta_a}{\cos\delta_a}, \quad (8)$$

where

$$\cos\varphi_a = \sin\delta_b\sin\delta_a + \cos\delta_b\cos\delta_a\cos(\alpha_a - \alpha_b). \quad (9)$$

It follows from equations (7) and (8) that the gravitational refraction moves the apparent position of the quasar away from the star. The magnitude of this effect is determined by the angular distance between the quasar and star, rather then by the mass of the star: $\Delta\alpha$ and $\Delta\delta$ are proportional to M_b and inversely proportional to φ_a^2.

4.2. Changes in the coordinates of reference quasars and rotation of the CCS. We used the *RSC(IERS)95C02* and *RSC(WGRF)95R01* catalogs referred to above to verify the effect of gravitational refraction on the stability of the CCS. The catalogs contain 607 and 608 objects, respectively. The radio sources are uniformly distributed over the sky between declinations –85° and +85°. The uncertainties in the coordinates are within the limits 50–2000 μarcsec.

Gravitational refraction changes the coordinates of all sources in time, which can be interpreted as a small rotation of the coordinate system. To estimate this rotation of the CCS, we use only the defining sources, which are the most compact objects. There are 236 such sources in the *RSC(IERS)95C02* and 212 in the *RSC(WGRF)9501* catalog, with 117 sources being common between the two. We used the Guide Star Catalog (GSC) [17] to identify visible stars.

In these catalogs, we searched for stars whose angular distances from the selected quasars did not exceed 1′. There are 30 such neighbor stars for 25 quasars in the first catalog and 65 neighbor stars for 58 quasars in the second catalog. For the overwhelming majority of stars, no characteristics are known that could enable us to estimate their distances or masses.

Table 1 presents the coordinates of four radio sources (0007+106, 0111+021, 0735+178, and 0912+297) from the *RSC(IERS)95C02* catalog with their classifications, redshifts z, magnitudes, and the angular distances from stars φ_a that are less than 1″. It is possible that the GSC actually gives the coordinates of the optical images of the radio sources. However, this is unlikely, since the magnitudes of the three last sources and those of the proposed optical images differ by more than unity. Since both the masses and distances to the stars are unknown, we estimated the changes in the coordinates of these quasars for $M_b/M_\odot = 5$ ($M_\odot$ is the mass of the Sun) and $L_{ob} = 500$ pc. The resulting shifts in right ascension and declination (in microarcsec) are –39.8 and 219.6, –82.4 and 133.7, –293.6 and –30.5, and 18.1 and –160.5, respectively.

As kindly reported to us by M. Eubanks, the measured proper motions of these sources are 475.6 ± 400.2, 35.3 ± 75.2, 96.3 ± 11.4, and 186.1 ± 173.4 μarcsec. We can see that the effect of gravitational lensing can entirely explain these proper motions. Therefore, one

possible origin for the shift in the centroid of the radio brightness of the radio source with time could be the motion of the lensing star.

In one case, we can calculate rather accurately the variation of the coordinates of a radio source in time. The B8III star 59803 from the *HIPPARCOS* catalog [18] with a mass of $M_b \sim 10M_\odot$, proper motion $\mu_\alpha^* = -159.58 \pm 0.66$ mas and $\mu_\delta = 22.31 \pm 0.54$ mas, and parallax $\pi = 19.78 \pm 0.81$ mas leads to changes in the apparent coordinates of the quasar 1213–172 (Fig. 2). Since the angular distance between the star and quasar is approximately 51″, the effect of gravitational lensing is rather small.

To estimate the rotation of the CCS produced by gravitational refraction, we introduce the vector $\mathbf{\Theta} = (\theta_1, \theta_2, \theta_3)$, which determines the rotation of the coordinate frame via the formula

$$\mathbf{r}_i' = \begin{pmatrix} 1 & -\theta_3 & \theta_2 \\ \theta_3 & 1 & -\theta_1 \\ -\theta_2 & \theta_1 & 1 \end{pmatrix} \mathbf{r}_i, \qquad (10)$$

where $\mathbf{r}_i$ and $\mathbf{r}_i'$ are unit radius vectors of the ith source before and after the gravitational deflection of the light. To estimate the distance L_{ob} to the star, we use the mass–luminosity relation

$$\log\frac{L_b}{L_\odot} = 3.5\log\frac{M_b}{M_\odot},$$

where L_s and $L_\odot$ are the luminosities of the star and the Sun, respectively. We chose the mass of each star randomly in the range 0.5–30 $M_\odot$ in accordance with a Salpeter mass function $dn/dM_b \sim M_b^{-2.35}$. The distance L_{ob} is determined by the equation

$$\log L_{ob} + 0.2aL_{ob} = 0.2(m + 0.26) + 1.75\log(M_b/M_\odot). \qquad (11)$$

Since the magnitudes m are in the range 11.3–16.2, the distances to the stars are limited to 100–5500 pc. We have derived equation (11) assuming that interstellar absorption near the Sun is 1.9^m/kpc [19].

We find that, for various mass functions, $\mathbf{\Theta} = -0.08 \pm 0.02$, -0.47 ± 0.03, and -0.36 ± 0.03 μarcsec for the *RSC(WGRF)95C02* catalog and $\mathbf{\Theta} = -0.07 \pm 0.05$, -1.19 ± 0.10, and -0.01 ± 0.01 μarcsec for the *RSC(WGRF)95R01* catalog. The small errors support our conclusion that the determining role is played by the relative position of the stars relative to the nearby reference radio sources, rather than by the stars' masses. Gravitational refraction prevents coincidence of the CCS axes for the two catalogs to better than 1 μarcsec. To estimate the time variations in $\mathbf{\Theta}$, we assumed the stars' proper motions are in the range –100 to +100 μarcsec/year. These are below the precision of current observations, enabling us to consider the stars stationary. Assuming various distributions for the proper motions, we found that the derivative of $\mathbf{\Theta}$ with respect to time (or the rotation of the real CCS with respect to an ideal CCS) is about 1 μarcsec over 20 years but can reach 1 μarcsec/year.

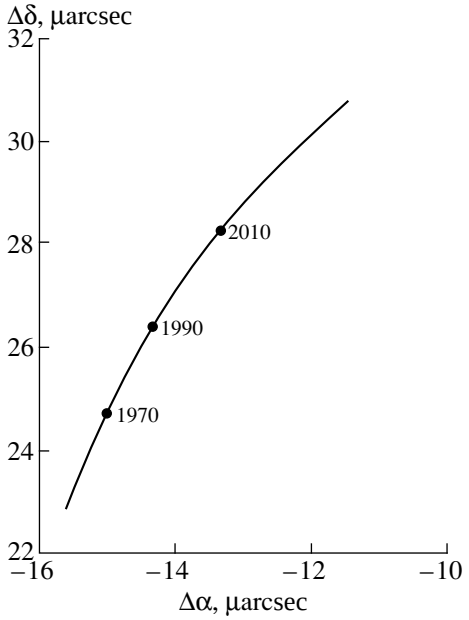

Fig. 2. Changes in coordinates of the radio source 1213–172 due to gravitational lensing.

Thus, the current instability of the CCS due to gravitational refraction cannot be detected experimentally. Nevertheless, we can draw the following important conclusions.

(1) The nonstationary gravitational field of the Galaxy gives rise to fluctuations in the coordinates of reference sources, making it impossible to realize an inertial CCS. This gravitational refraction introduces noise; the random rotations of the CCS are of the order of 10^{-12}. This represents a lower limit, since we have taken into account only the gravitational fields of visible stars. Allowing for the presence of dark Galactic bodies increases this value by a factor of 5–10 [15].

(2) Gravitational lensing can change the apparent coordinates not only of radio sources but also of stars. Therefore, the star catalogs planned in the GAIA and SIM programs will also be unstable at the microarcsec level.

(3) According to (2), the instability of the CCS introduces an error of the order of 1 μarcsec in the observed nutation. Therefore, this is the limit of accuracy for measurements of nutation terms.

5. KINEMATIC APPROACH TO INSTABILITY OF THE ECS

This section examines the effect on the Earth orientation parameters of possible rotations of the crust with respect to the mantle, which are neglected in current theories of precession and nutation.

Let us assume that the deformation velocity fields in The crust and mantle differ. This means that the Tisserand axes for the crust and mantle do not coincide. In this case, the definition of the ECS—zero relative angular momentum of the crust—implies a rotation of the ECS with respect to the Tisserand axes of the mantle. We will consider the physical reasons for this rotation in the next section. Here, we obtain some kinematic relations between the nutation and motion of the pole, allowing for the rotation of the crust with respect to the mantle.

We consider the following coordinate systems (CS): the inertial frame X, Y, Z and the nutation frame x^0, y^0, z^0 with unit vectors $\mathbf{i}_1^0$, $\mathbf{i}_2^0$, $\mathbf{i}_3^0$ and with the z^0 axis being in the Z direction. Let the nutation CS rotate with a constant angular velocity Ω_0 about the z^0 axis. The rotation vector for the nutation CS has the components $\mathbf{\Omega}_0 = (0, 0, \Omega)$ in the inertial CS. Assume also that the CS x', y', z' is fixed to the mantle, while the CS x'', y'', z'' is fixed to the crust (i.e., by definition, it is the ECS). We denote the unit vectors of these systems $\mathbf{i}_1'$, $\mathbf{i}_2'$, $\mathbf{i}_3'$, and $\mathbf{i}_1''$, $\mathbf{i}_2''$, $\mathbf{i}_3''$, respectively.

Each vector can now be expressed using the coordinates in the systems fixed to the crust and mantle, and also using coordinates in the system x^0, y^0, z^0; that is, $\mathbf{r}' = A\mathbf{r}^0$, where the matrix A represents the transformation relating the unit vectors $\mathbf{i}_k^0$ $(k = 1, 2, 3)$ to the unit vectors $\mathbf{i}_k'$ of the rotated system [20].

Let us assume that the CS x', y', z' is rotated by a small angle with respect to the CS x^0, y^0, z^0. In this case, $A = I + \Theta'$ and $\mathbf{r}' = (I + \Theta')\mathbf{r}^0$, where I is the unit matrix and Θ' is the infinitesimal rotation matrix. This transformation can be expressed in the equivalent form

$$\mathbf{r}' = \mathbf{r}^0 - \mathbf{\Theta}' \times \mathbf{r}^0, \tag{12}$$

where $\mathbf{\Theta}'$ is a vector with the components Θ_1', Θ_2', Θ_3'.

If the CS x'', y'', z'' is rotated by a small angle with respect to the CS x', y', z', then

$$\mathbf{r}'' = \mathbf{r}' - \mathbf{\Theta}'' \times \mathbf{r}', \tag{13}$$

where $\mathbf{\Theta}''$ is a vector with components Θ_1'', Θ_2'', Θ_3''. Substituting (12) into (13) and neglecting quadratic terms, we obtain

$$\mathbf{r}'' \approx \mathbf{r}^0 - (\mathbf{\Theta}' + \mathbf{\Theta}'') \times \mathbf{r}^0. \tag{14}$$

Since expression (14) is valid for an arbitrary vector, we can write this transformation for the instantaneous Earth rotation vector Ω with components ω_1, ω_2, ω_3 in the CS x'', y'', z'' and $\mathbf{\Omega}^0 = (\omega_1^0, \omega_2^0, \omega_3^0)$ in the CS x^0, y^0, z^0:

$$\mathbf{\Omega} = \mathbf{\Omega}^0 - (\mathbf{\Theta}' + \mathbf{\Theta}'') \times \mathbf{\Omega}^0. \tag{15}$$

If $\dot{\Theta}' = d\mathbf{\Theta}'/dt$ and $\dot{\Theta}'' = d\mathbf{\Theta}''/dt$, we easily obtain

$$\mathbf{\Omega}^0 = \mathbf{\Omega}_0 + \dot{\Theta}' + \dot{\Theta}''. \tag{16}$$

We emphasize that formula (16) represents the instantaneous Earth-rotation vector in the inertial CS determined from observations on the surface of the Earth crust.

Substituting (16) into (15) and neglecting second-order terms yields

$$\mathbf{\Omega} = \mathbf{\Omega}_0 + \dot{\Theta}' + \dot{\Theta}'' - (\mathbf{\Theta}' + \mathbf{\Theta}'') \times \mathbf{\Omega}_0, \tag{17}$$

or

$$\begin{aligned} \omega_1 &= \dot{\Theta}_1' + \dot{\Theta}_1'' - (\Theta_2' + \Theta_2'')\Omega, \\ \omega_2 &= \dot{\Theta}_2' + \dot{\Theta}_2'' - (\Theta_1' + \Theta_1'')\Omega, \\ \omega_3 &= \dot{\Theta}_3' + \dot{\Theta}_3'' + \Omega, \end{aligned} \tag{18}$$

written in components. We can see from (18) that the crust's rotation affects measurements of both the coordinates of the pole and the angular velocity of rotation. We can also see that, to determine ω_1 and ω_2, we must know not only changes in Θ_1'' and Θ_2'', but also the initial angles. These angles will be estimated in the next section.

Let us use these expressions to take into account the effect of the crust's rotation on the polar motion. We assume for simplicity that $\Theta_3' = \Theta_3'' = 0$, since we are not interested in changes of the rotation velocity. Then, we can easily express the vectors in terms of complex numbers. If we introduce the complex number $w' = \Theta_1' + i\Theta_2'$, then $\mathbf{\Theta}' = w'\mathbf{i}_1^0$, since $i\mathbf{i}_1^0 = \mathbf{i}_2^0$. Similarly, $\mathbf{\Theta}'' = w''\mathbf{i}_1^0$ if $w'' = \Theta_1'' + i\Theta_2''$.

We denote $\mathbf{m}_R$ to be the motion of the instantaneous rotation axis with unit vector $\mathbf{i}_R$ with respect to the Tisserand axis z''. Traditionally, the vector $\mathbf{m}_R$ is called the polar motion; its components along the axes x and y are denoted m_1 and m_2 and can be found from the Euler–Liouville equations [8]. The quantities m_1 and m_2 differ from the quantities p_1 and p_2 calculated by the IERS (Fig. 1). If $\tilde{m}_R(t) = m_1(t) + im_2(t)$ and $\tilde{p}(t) = p_1(t) + ip_2(t)$,

$$\tilde{m}_R(t) = \tilde{p}(t) - \frac{i}{\Omega}\frac{d\tilde{p}(t)}{dt}.$$

Table 2. Nonequilibrium parameters of boundaries of the Earth

Boundary	$\Delta\sigma$, g/cm^3	A_{10}, km	A_{11}, km	B_{11}, km	A_{20}, km	A_{21}, km	B_{21}, km	A_{22}, km	B_{22}, km
1	2.67	0.40	0.38	0.24	0.25	0.20	0.18	–0.29	–0.06
2	0.30	–3.45	–2.60	–3.20	–3.25	–0.71	–1.63	2.04	1.44
3	0.39	0.25	–0.32	1.18	1.12	–0.75	0.21	0.20	–0.87
4	4.34	0.02	–0.06	0.17	–0.36	–0.28	0.05	0.47	–0.51

It is obvious that, for secular variations, $\tilde{m}_R(t) = \tilde{p}(t)$. Taking this into account, we obtain $\mathbf{m}_R = \mathbf{i}_R - \mathbf{i}_3''$. The main distinction of these equations from those commonly used is that the coordinates of the pole are measured with respect to the rotating CS x'', y'', z''.

Expressing the unit vectors $\mathbf{i}_R$ and $\mathbf{i}_3''$ in terms of the $\mathbf{i}_3^0$, we obtain the desired kinematic relation. This will be simplest to do for spectral notation. Since, in this case, $w \sim e^{\sigma t}$, $\dot{w} = i\sigma w$. Consequently, $\dot{\Theta}' = i\sigma_1\Theta'$ and $\dot{\Theta}'' = i\sigma_2\Theta''$.

Instead of expression (16), we obtain

$$\mathbf{\Omega}^0 = \Omega\mathbf{i}_3^0 + i(\sigma_1\Theta' + \sigma_2\Theta'').$$

Then, the unit vector $\mathbf{i}_R$ directed along the instantaneous rotation axis becomes

$$\mathbf{i}_R = \frac{\mathbf{\Omega}^0}{\Omega} = \mathbf{i}_3^0 + i\left(\frac{\sigma_1}{\Omega}\Theta' + \frac{\sigma_2}{\Omega}\Theta''\right). \qquad (19)$$

To determine the vector $\mathbf{i}_3''$, note that $\mathbf{i}_3'' = A^{-1}\mathbf{i}_3^0$ [20]. Up to linear terms, $A^{-1} = I - (\Theta' - \Theta'')$, so that

$$\mathbf{i}_3'' = \mathbf{i}_3^0 + (\mathbf{\Theta}' + \mathbf{\Theta}'') \times \mathbf{i}_3^0.$$

In complex notation, w' and w'', we obtain $\mathbf{i}_3'' = \mathbf{i}_3^0 - i(w' + w'')\mathbf{i}_1^0$.

Substituting for $\mathbf{i}_R$ and $\mathbf{i}_3''$ their corresponding values, we obtain the complex number $\tilde{m}_R = iw'(\sigma_1 + \Omega)/\Omega + iw''(\sigma_2 + \Omega)/\Omega$. Then, for free Euler motion with $\sigma_1 = \sigma_E$ and $\sigma_2 \ll \sigma_1$, $w' = \alpha e^{i\sigma_E t}$ and $w'' = \beta e^{i\sigma_2 t}$, we obtain

$$\tilde{m}_R = m_0 e^{i\sigma_E t} + i\beta - \beta\sigma_2 t,$$

where the complex amplitude m_0 of the Chandler motion is $m_0 = i\alpha(\sigma_E + \Omega)/\Omega$. This equation is equivalent to the two first equations of (18). We can clearly see that the rotation of the crust yields a secular motion of the pole.

Further, we will consider the possible origins of rotation of the crust with respect to the mantle and estimate the quantity $w'' = \Theta_1'' + i\Theta_2''$.

6. DYNAMIC APPROACH TO INSTABILITY OF THE ECS

Current models of the Earth's nutation [21, 22] are based on the following assumptions. The Earth rotates with a constant speed about the axis shared by three ellipsoidal shells: the mantle, the inner core, and the outer core. The mantle and the inner core are elastic. All shells are spherically stratified, and there are no dissipation processes. The surfaces of constant density are assumed to be surfaces of constant potential. These surfaces, including their boundaries, are assumed to be determined by the condition of hydrostatic equilibrium.

However, our investigations [23, 24] of the density boundaries of the Earth's shells (the relief R, Mohorovicic discontinuity, boundary at the depth d = 660 km, and core–mantle boundary C–M) show that, in expansions of the radius vectors of these boundaries in terms of spherical functions, both the harmonics A_{1k} and B_{1k} describing the displacement of the boundary with respect to the Earth's center of mass and the harmonics A_{2k} and B_{2k} indicating departure of the boundary from the equilibrium ellipsoid are very significant (Table 2).

If we know the density discontinuities $\Delta\sigma$ at the boundaries (from the PREM model [25] and our own studies of the Mohorovicic discontinuity), we can calculate the contribution of the boundaries to the Earth's nonequilibrium gravitational field using a simple layer model. We can estimate the contribution of the individual shells of the Earth to the nonequilibrium gravitational field assuming that their main contribution is produced by their nonequilibrium boundaries (irregularities inside the crust are included in the model for the equivalent relief R, and possible density irregularities due to convection in the upper mantle are taken into account when modeling the d = 660 km boundary). Then, using known formulas from gravitational theory, we can find the displacements x_0, y_0, z_0 of the shell centers of mass from the Earth's center of mass and also deviations of the shell moments of inertia from their equilibrium values A, B, and C.

We will demonstrate that a significant departure of the crust from hydrostatic equilibrium could be one origin for a large pressure torque that could lead to motion of the crust with respect to the mantle.

6.1. Modeling the earth's nonequilibrium field. We can represent the Earth's outer gravitational potential, derived from gravimetric and satellite observations, as the sum of two potentials $U_0 + \Delta U$, where U_0

Table 3. Nonequilibrium gravitational field of the Earth

Boundary	$\bar{C}_{10}$, 10^{-5}	$\bar{C}_{11}$, 10^{-5}	$\bar{D}_{11}$, 10^{-5}	$\bar{C}_{20}$, 10^{-5}	$\bar{C}_{21}$, 10^{-5}	$\bar{D}_{21}$, 10^{-5}	$\bar{C}_{22}$, 10^{-5}	$\bar{D}_{22}$, 10^{-5}
1	3.092	2.872	1.792	1.147	0.907	0.805	–1.310	–0.255
2	–3.297	–2.489	–3.059	–1.860	–0.407	–0.930	1.162	0.822
3	0.202	–0.256	0.936	0.477	–0.319	0.089	0.085	–0.373
4	0.043	–0.126	0.331	–0.235	–0.181	0.036	0.307	–0.333
Σ	0	0	0	–0.471	0	0	0.244	–0.139

is the Earth's potential for hydrostatic equilibrium and ΔU is the nonequilibrium potential.

We modeled the Earth's nonequilibrium potential as the sum of potentials of simple spherical layers situated at the main density boundaries detected inside the Earth via seismic observations: $\Delta U = \Sigma_i \Delta U_i$. The potential of each layer in outer space is presented as an expansion in spherical functions

$$\Delta U_i(r, \varphi, \lambda) = \frac{GM}{r} \times \sum_{n=2}^{\infty} \sum_{m=0}^{n} \left(\frac{a}{r}\right)^n (C_{nm}^i \cos m\lambda + D_{nm}^i \sin m\lambda) P_n^m(\sin\varphi),$$

where M and a are the Earth's mass and semi-major axis, while r, φ, and λ are the spherical coordinates of the observation point.

We have taken as the main density boundaries:

(1) The surface of the equivalent (uniform in density) relief R;

(2) The Mohorovicic discontinuity;

(3) The interface surface at a depth d = 660 km;

(4) The core–mantle boundary C–M.

The contribution of each of these shells to the Earth's nonequilibrium gravitational field is described by the formula

$$\begin{Bmatrix} C_{nm}^i \\ D_{nm}^i \end{Bmatrix} = \frac{3}{2n+1}\left(\frac{R_i}{a}\right)^{n+2} \frac{\Delta\sigma_i a^2}{\bar{\sigma}\bar{R}^3} \begin{Bmatrix} A_{nm}^i \\ B_{nm}^i \end{Bmatrix}, \qquad (20)$$

where $\bar{R}$ = 6369.4 km and $\bar{\sigma}$ = 5.517 g/cm^3 are the Earth's radius and average density, R_i and $\Delta\sigma_i$ are the average radii of the shells and their density discontinuities, and A_{nm}^i and B_{nm}^i are the coefficients of expansion of the shell reliefs (with respect to the hydrostatic surface) in terms of the spherical functions.

We have used our own results [23, 24] from the processing and harmonic analysis of observational data (topographic, petrologic, and seismic) as the expansion coefficients for the equivalent relief and the Mohorovicic surface. The coefficients for the relief of the 660-km interface surface were based on the assumption of hydrostatic equalization of the pressures at this depth

$$\Delta\sigma_3 \begin{Bmatrix} A_{nm}^3 \\ B_{nm}^3 \end{Bmatrix} = \Delta\sigma_1 \begin{Bmatrix} A_{nm}^1 \\ B_{nm}^1 \end{Bmatrix} + \frac{\Delta\sigma_2}{\sigma_3} \begin{Bmatrix} A_{nm}^2 \\ B_{nm}^2 \end{Bmatrix},$$

where $\Delta\sigma_1$ = 2.67 g/cm^3 and $\Delta\sigma_2$ = 0.30 g/cm^3. The expansion coefficients for the relief heights of the core–mantle boundary are then determined by the formula

$$\begin{Bmatrix} A_{nm}^4 \\ B_{nm}^4 \end{Bmatrix} = \frac{2n+1}{3}\left(\frac{a}{R_4}\right)^{n+2} \frac{\bar{\sigma}\bar{R}^3}{\Delta\sigma_4 a^2} \begin{Bmatrix} C_{nm}^4 \\ D_{nm}^4 \end{Bmatrix},$$

where

$$\begin{Bmatrix} C_{nm}^4 \\ D_{nm}^4 \end{Bmatrix} = \begin{Bmatrix} \Delta C_{nm} \\ D_{nm} \end{Bmatrix} - \begin{Bmatrix} C_{nm}^{1+2+3} \\ D_{nm}^{1+2+3} \end{Bmatrix}, \quad \Delta C_{nm} = C_{nm} - C_{nm}^{(0)},$$

C_{nm} and D_{nm} are the Stokes constants for the Earth, and $C_{nm}^{(0)}$ are the harmonic coefficients of the Earth's gravitational field for hydrostatic equilibrium: $\bar{C}_{20} = -4.7946 \times 10^{-4}$.

Table 3 presents the coefficients obtained using formula (20) for n = 1, 2 and normalized by the norm $k_{nm} = \sqrt{\varepsilon_m (2n+1)(n-m)!/(n+m)!}$, where $\varepsilon_0 = 1$ and $\varepsilon_{m>0} = 2$.

Since such modeling of the Earth's nonequilibrium field ascribes all possible density irregularities to the shell boundaries, the nonequilibrium gravitational field of each shell (crust, mantle, and core) is expressed in the form:

$$\text{crust—} \begin{Bmatrix} C_{nm} \\ D_{nm} \end{Bmatrix} = \begin{Bmatrix} C_{nm}^1 \\ D_{nm}^1 \end{Bmatrix} - \frac{\rho_{cr}}{\Delta\sigma_2} \begin{Bmatrix} C_{nm}^2 \\ D_{nm}^2 \end{Bmatrix},$$

$$\text{mantle—} \begin{Bmatrix} C_{nm} \\ D_{nm} \end{Bmatrix} = \frac{\rho_{m1}}{\Delta\sigma_2} \begin{Bmatrix} C_{nm}^2 \\ D_{nm}^2 \end{Bmatrix} + \begin{Bmatrix} C_{nm}^3 \\ D_{nm}^3 \end{Bmatrix} - \frac{\rho_{m2}}{\Delta\sigma_4} \begin{Bmatrix} C_{nm}^4 \\ D_{nm}^4 \end{Bmatrix},$$

$$\text{core—} \begin{Bmatrix} C_{nm} \\ D_{nm} \end{Bmatrix} = \frac{\rho_c}{\Delta\sigma_4} \begin{Bmatrix} C_{nm}^4 \\ D_{nm}^4 \end{Bmatrix}.$$

Table 4. Nonequilibrium gravitational field of the Earth's shells

	$\bar{C}_{10}$, 10^{-5}	$\bar{C}_{11}$, 10^{-5}	$\bar{D}_{11}$, 10^{-5}	$\bar{C}_{20}$, 10^{-5}	$\bar{C}_{21}$, 10^{-5}	$\bar{D}_{21}$, 10^{-5}	$\bar{C}_{22}$, 10^{-5}	$\bar{D}_{22}$, 10^{-5}
Crust	31.17	24.10	27.88	17.012	4.378	8.737	–11.222	–7.266
Mantle	–31.27	–23.81	–28.63	–16.947	–3.966	–8.820	10.766	7.887
Core	0.098	–0.287	0.754	–0.536	–0.413	0.082	0.700	–0.759
Σ	0	0	0	–0.471	0	0	0.244	–0.139

Table 5. Coordinates of centers of inertia and nonequilibrium moments of inertia of the Earth's shells with respect to its center of mass

	x_0, km	y_0, km	z_0, km	$\Delta\left(\frac{A+B}{2}-C\right)$, 10^{33} kg m^2	$B-A$, 10^{33} kg m^2	E, 10^{33} kg m^2	F, 10^{33} kg m^2	D, 10^{33} kg m^2
Crust	535	619	692	92.43	–70.40	13.73	27.41	–22.80
Mantle	–3.90	–4.69	–5.09	–92.08	67.54	–12.44	–27.67	24.74
Core	–0.10	0.26	0.03	–2.91	4.392	–1.30	0.26	–2.38

Here, $\rho_{cr} = 2.85$ g/cm^3 is the average density of the crust near the boundary with the mantle, $\rho_{m1} = 3.20$ g/cm^3 is the average density of the mantle near the boundary with the crust, $\rho_{m2} = 5.55$ g/cm^3 is the average density of the mantle near the boundary with the core, $\rho_c = 9.89$ g/cm^3 is the average density of the core near the boundary with the mantle, and $\Delta\sigma_4 = 4.34$ g/cm^3. The coefficients obtained are presented in Table 4.

6.2. Centers and moments of inertia for the earth's shells. Using the formulas of gravitational theory [26] expressing the first terms of the expansion of the gravitational potential of an arbitrary body in terms of the coordinates of its center of inertia and moment of inertia, we obtain for the Earth's shells

$$\begin{vmatrix}\Delta x\\ \Delta y\\ \Delta z\end{vmatrix} = \sqrt{3}a\begin{vmatrix}\bar{C}_{11}\\ \bar{D}_{11}\\ \bar{C}_{10}\end{vmatrix}\frac{M}{m},$$

where Δx, Δy, Δz are the coordinates of the shell centers of inertia in a reference frame fixed to the Earth's center of mass. Here, M is the Earth's total mass and m is the shell mass,

$$\Delta\left(\frac{A+B-2C}{2}\right) = \sqrt{5}Ma^2\Delta\bar{C}_{20},$$

$$\frac{B-A}{2} = \sqrt{\frac{5}{12}}Ma^2\bar{C}_{22}, \quad \begin{vmatrix}D\\ E\\ F\end{vmatrix} = \sqrt{\frac{5}{3}}Ma^2\begin{vmatrix}\bar{D}_{22}\\ \bar{C}_{21}\\ \bar{D}_{21}\end{vmatrix},$$

A, B, C, D, E, and F are the shell moments of inertia with respect to the Earth's center of mass. Table 5 presents the results obtained.

Using calculations for a standard Earth model ($A = 801 \times 10^{35}$ kg m^2 for the Earth as a whole, $A_f = 91.2 \times 10^{35}$ kg m^2 for the core, $A_{cr} \approx 2/3 m_{cr}\bar{a}_{cr} = 8.7 \times 10^{35}$ kg m^2 for the crust, and $A_m = A - A_f - A_{cr} = 701 \times 10^{35}$ kg m^2 for the mantle), we obtain the following corrections for the moments of inertia and dynamic compressions of the Earth's shells:

$$\Delta A = 0, \quad \Delta B = B - A,$$

$$\Delta C = \Delta(C-A) = -\sqrt{5}Ma^2\left(\Delta\bar{C}_{20} - \frac{1}{2\sqrt{3}}\bar{C}_{22}\right)$$

$$= \frac{B-A}{2} - \Delta\frac{A+B-2C}{2},$$

$$\Delta\varepsilon = \frac{\Delta\left(C - \frac{A+B}{2}\right)}{C} \approx \frac{(1-\varepsilon_0)\Delta\left(C-\frac{A+B}{2}\right)}{C},$$

where ε_0 is the equilibrium compression for the outer shell boundaries. Table 6 presents the results obtained for three-layer and two-layer models of the Earth.

Table 6 shows that the corrections to the moments of inertia of the crust and mantle are rather significant. Theories of the Earth's rotation neglect the crust, since its mass and moment of inertia are less than 1% of the Earth's total mass and moment of inertia. However, Table 6 shows that the corrections to the moments of inertia of the crust and mantle are nearly equal in absolute value and opposite in sign. For a two-layer model of the Earth (crust + mantle + core), this behavior disappears. Apparently, this model is applicable for short-term disturbances. In this case, the correction $\Delta\varepsilon$ for the dynamic compression of the core is the main one. We

Table 6. Corrections to the moments of inertia and compressions of the Earth's shells

	ΔB, 10^{33} kg m^2	ΔC, 10^{33} kg m^2	ΔE, 10^{33} kg m^2	ΔF, 10^{33} kg m^2	ΔD, 10^{33} kg m^2	ε_0	$\Delta\varepsilon$
Crust	–70.4	–127.6	13.7	27.4	–22.8	0.00334	–0.112 ± 0.42
Mantle	67.5	125.9	–12.4	–27.7	24.7	0.00337	0.00131 ± 0.00047
Core	4.4	5.1	–1.3	0.3	–2.4	0.00252	0.00032 ± 0.00024
Crust + mantle	–2.9	–1.8	1.3	–0.3	2.0	0.00337	0.0
Core	4.4	5.1	–1.3	0.3	–2.4	0.00252	0.00032 ± 0.00024

should keep in mind that, for a two-layer model of the Earth, this correction is an upper limit for the possible deviation of the core compression from its equilibrium value.

However, the crust can rotate with respect to the mantle if there is an asthenospheric boundary layer of reduced viscosity between them [29]. Since there is a significant deviation of the crust from hydrostatic equilibrium (Table 6), we argue that the crust must be taken into account in computations of long-term variations of the Earth's rotation. Below, we present a brief mathematical proof of this assertion and some numerical estimates.

6.3. Total torque of the non-hydrostatic crust pressing on the mantle. For the Earth in hydrostatic equilibrium, all pressure forces inside the Earth are normal to a level surface that coincides with the surfaces of equal density and pressure. Therefore, there are no torques producing relative rotations of the Earth's shells. Thus, we must take into account only the non-hydrostatic component of the crust pressing on the mantle when calculating torques that can produce relative rotation. This is mainly associated with the departure of the relief heights and mantle surface (the Mohorovicic surface M) from the corresponding surfaces for hydrostatic equilibrium. Density irregularities inside the crust are taken into account in the model for the equivalent (uniform in density) relief [24] and the model for the M depths [23].

Let us consider three orthogonal components of the total torque due to the crust pressing on the mantle: L_3 directed along the axis z of the Earth's rotation, and L_1 and L_2 directed along the axis x in the plane of the Greenwich meridian ($\lambda = 0°$) and the axis y ($\lambda = 90°$), respectively.

These components are determined by the formulas

$$L_{1,2,3} = \int_{-\pi/2}^{\pi/2}\int_{0}^{2\pi} l_{1,2,3} r_2^2 \cos\varphi\, d\lambda\, d\varphi,$$

where $l_{1,2,3} = (\mathbf{r}_2 \times \mathbf{p}_n)_{1,2,3}$ and $\mathbf{r}_2(\varphi, \lambda) = [R_2(1 - e\sin^2\varphi) + H_2(\varphi, \lambda)]\mathbf{i}_r$ is the mantle radius vector; $R_2 = 6348660$ m is the average radius of the M surface; $e = 0.00334$ is the hydrostatic compression; $\mathbf{p}_n(\varphi, \lambda) = -(p\cos\alpha)\mathbf{n}$ and $p(\varphi, \lambda) = (R_1/R_2)^2\sigma_1 H_1 g_1 - \sigma_2 H_2 g_2$ are the non-hydrostatic forces of the crust pressing on the mantle directed along the outer normal $\mathbf{n}$ of the mantle surface and along the inner normal of the level surface, respectively; $\alpha(\varphi, \lambda)$ is the inclination angle between the mantle and the level surface; $R_1 = 6369620$ m is the Earth's average radius;

$$H_{1,2}(\varphi, \lambda) = \sum_{n=1}^{N}\sum_{m=0}^{n} (A_{nm}^{(1,2)}\cos m\lambda + B_{nm}^{(1,2)}\sin m\lambda) P_n^m(\sin\varphi)$$

are the heights of the equivalent relief (index 1) and the Mohorovicic surface (index 2) with respect to the corresponding hydrostatic ellipsoids; $\sigma_1 = 2.67 \times 10^3$ kg/m^3 and $\sigma_2 = 2.85 \times 10^3$ kg/m^3 are the average densities of the crust;

$$g_{1,2}(\varphi, \lambda) = g_{1,2}^{(0)}(1 + \beta\sin^2\varphi) + \Delta g_{1,2}(\varphi, \lambda)$$

are the accelerations of gravity at the Earth's surface and near the mantle, respectively; and $\beta = 0.00530$.

After some manipulation, we obtain

$$l_1 = -p_n r_2(\gamma_\varphi \sin\lambda - \gamma_\lambda \sin\varphi\cos\lambda),$$

$$l_2 = +p_n r_2(\gamma_\varphi \cos\lambda + \gamma_\lambda \sin\varphi\sin\lambda),$$

$$l_3 = -p_n r_2 \gamma_\lambda \cos\varphi,$$

$$\cos\alpha = 1/\sqrt{1 + \gamma_\varphi^2 + \gamma_\lambda^2},$$

where $\gamma_\lambda = \dfrac{1}{r_2\cos\varphi}\dfrac{\partial H_2}{\partial\lambda}$ and $\gamma_\varphi = \dfrac{1}{r_2}\dfrac{\partial H_2}{\partial\varphi}$ are the longitudinal and latitudinal inclinations of M, respectively.

To estimate the possible effect, we use a linear approximation taking into account the fact that α, γ, β, H/R, and $(R_1 - R_2)/R$ are small parameters. Assuming that $\cos\alpha \approx 1 - (\gamma_\varphi^2 + \gamma_\lambda^2)/2 \approx 1$, $Hgr_2^2 \approx Hg^{(0)}R_2^2$, and $k = g_2\sigma_2/(g_1\sigma_1) = \text{const}$, we obtain

$$L_{1,2,3} = L_0(L_{1,2,3}^{(1)} - kL_{1,2,3}^{(2)}),$$

where $L_0 = \sigma_1 g_1^{(0)} R_2^2 = 1.052 \times 10^{18}$ kg/s^2,

$$L_1^{(1,2)} = \iint H_{1,2}\left(\frac{\partial H_2}{\partial\varphi}\sin\lambda\right.$$

$$-\frac{1}{\cos\varphi}\frac{\partial H_2}{\partial\lambda}\sin\varphi\cos\lambda\Big)\cos\varphi d\lambda d\varphi,$$

$$L_2^{(1,2)} = \iint H_{1,2}\Big(\frac{\partial H_2}{\partial\varphi}\cos\lambda$$

$$-\frac{1}{\cos\varphi}\frac{\partial H_2}{\partial\lambda}\sin\varphi\sin\lambda\Big)\cos\varphi d\lambda d\varphi,$$

$$L_3^{(1,2)} = \iint H_{1,2}\frac{\partial H_2}{\partial\lambda}\cos\varphi d\lambda d\varphi.$$

Integration and several transformations yield (taking into account the orthogonality of the spherical functions):

$$L_1^{(1,2)} = \sum_{n=1}^{N}\frac{\pi}{2n+1}\sum_{m=1}^{n}\delta_{m-1}\frac{(n+m)!}{(n-m)!}(A^{(2)}_{n,m-1}B^{(1,2)}_{n,m} - A^{(1,2)}_{n,m-1}B^{(2)}_{n,m} + A^{(2)}_{n,m}B^{(1,2)}_{n,m-1} - A^{(1,2)}_{n,m}B^{(2)}_{n,m-1}),$$

$$L_2^{(1,2)} = \sum_{n=1}^{N}\frac{-\pi}{2n+1}\sum_{m=1}^{n}\delta_{m-1}\frac{(n+m)!}{(n-m)!}(A^{(2)}_{n,m-1}A^{(1,2)}_{n,m} - A^{(1,2)}_{n,m-1}A^{(2)}_{n,m} - B^{(2)}_{n,m}B^{(1,2)}_{n,m-1} + B^{(1,2)}_{n,m}B^{(2)}_{n,m-1}),$$

$$L_3^{(1,2)} = \sum_{n=1}^{N}\frac{2\pi}{2n+1}\times\sum_{m=1}^{n}m\frac{(n+m)!}{(n-m)!}(A^{(1,2)}_{n,m}B^{(2)}_{n,m} - A^{(2)}_{n,m}B^{(1,2)}_{n,m}),$$

where $\delta_0 = 2$, $\delta_{m>0} = 1$. Hence, we see that $L^{(2)}_{1,2,3} = 0$, $L = L_0L_1$

Using the normalized coefficients

$$\begin{Bmatrix}\bar A_{nm}\\ \bar B_{nm}\end{Bmatrix} = \frac{1}{N_{nm}}\begin{Bmatrix}A_{nm}\\ B_{nm}\end{Bmatrix},\quad N_{nm} = \sqrt{\frac{2(2n+1)(n-m)!}{\delta_m(n+m)!}},$$

we obtain the following final form for the components of the torque due to the non-hydrostatic pressure of the crust on the mantle

$$L_1^{(1,2)} = 2\pi L_0\times\sum_{n=1}^{N}\sum_{m=1}^{n}\sqrt{\delta_{m-1}(n-m+1)(n+m)}(\bar A^{(2)}_{n,m-1}\bar B^{(1)}_{n,m} - \bar A^{(1)}_{n,m-1}\bar B^{(2)}_{n,m} + \bar A^{(2)}_{n,m}\bar B^{(1)}_{n,m-1} - \bar A^{(1)}_{n,m}\bar B^{(2)}_{n,m-1}),$$

$$L_2^{(1,2)} = -2\pi L_0\times\sum_{n=1}^{N}\sum_{m=1}^{n}\sqrt{\delta_{m-1}(n-m+1)(n+m)}(\bar A^{(2)}_{n,m-1}\bar A^{(1)}_{n,m} - \bar A^{(1)}_{n,m-1}\bar A^{(2)}_{n,m} - \bar B^{(2)}_{n,m}\bar B^{(1)}_{n,m-1} + \bar B^{(1)}_{n,m}\bar B^{(2)}_{n,m-1}),$$

$$L_3^{(1,2)} = 4\pi L_0\sum_{n=1}^{N}\sum_{m=1}^{n}m(\bar A^{(1)}_{n,m}\bar B^{(2)}_{n,m} - \bar A^{(2)}_{n,m}\bar B^{(1)}_{n,m}).$$

We can see that, if there is complete isostatic compensation of the relief by the Mohorovicic boundary:

$$\sigma_1 H_1(\varphi,\lambda) = -\Delta\sigma_2 H_2(\varphi,\lambda),$$

where $\Delta\sigma_2$ is the M density discontinuity, the proportionality

$$\frac{A^{(2)}_{nm}}{A^{(1)}_{nm}} = \frac{B^{(2)}_{nm}}{B^{(1)}_{nm}} = \text{const},$$

yields

$$L_1 = L_2 = L_3 = 0.$$

Thus, the net torque applied by the crust pressing on the mantle can differ from zero only if the isostatic compensation of the relief is not complete.

The computations show that, at the present time, the components of the total torque of the crust pressing on the mantle are almost constant in sign (independent of the power N of the representation of the relief) and reach $|L| \approx 5\times10^{25}$ Nm for $N = 30$ (Fig. 3), which is approximately three orders of magnitude larger than the lunar–solar torque. If there is no rigid connection between the crust and mantle, these torques can retard the mantle's rotation with respect to the crust ($L_3 < 0$) and produce a relative rotation of the mantle in the direction determined by $L_1 > 0$ and $L_2 > 0$.

By virtue of conservation of the Earth's total angular momentum, the rotation of the mantle resulting from the uncompensated crust pressure on the mantle creates a rotation of the crust in the opposite direction. For the crust, the linear corrections $\dot{\boldsymbol{\Theta}}''$ to the total rotation vector of the Earth can be determined by the equations

$$J_{1,2,3}\dot\Theta''_{1,2,3} = L^k_{1,2,3} + L_{\rm fr},$$

where $J_{1,2,3}$ are the moments of inertia of the crust, $L^k_{1,2,3} = -L_{1,2,3}$ is the torque due to the non-hydrostatic mantle pressing on the crust, and $L_{\rm fr}$ is the friction torque directed opposite to the L^k. Motion is possible when $|L_{\rm fr}| < |L^k|$, depending on the physical properties (primarily the viscosity) of the crust–mantle boundary layer.

As demonstrated above, a crust rotation torque can only arise if the isostatic equilibrium of the crust is disrupted. The main origins of such disruption are phe-

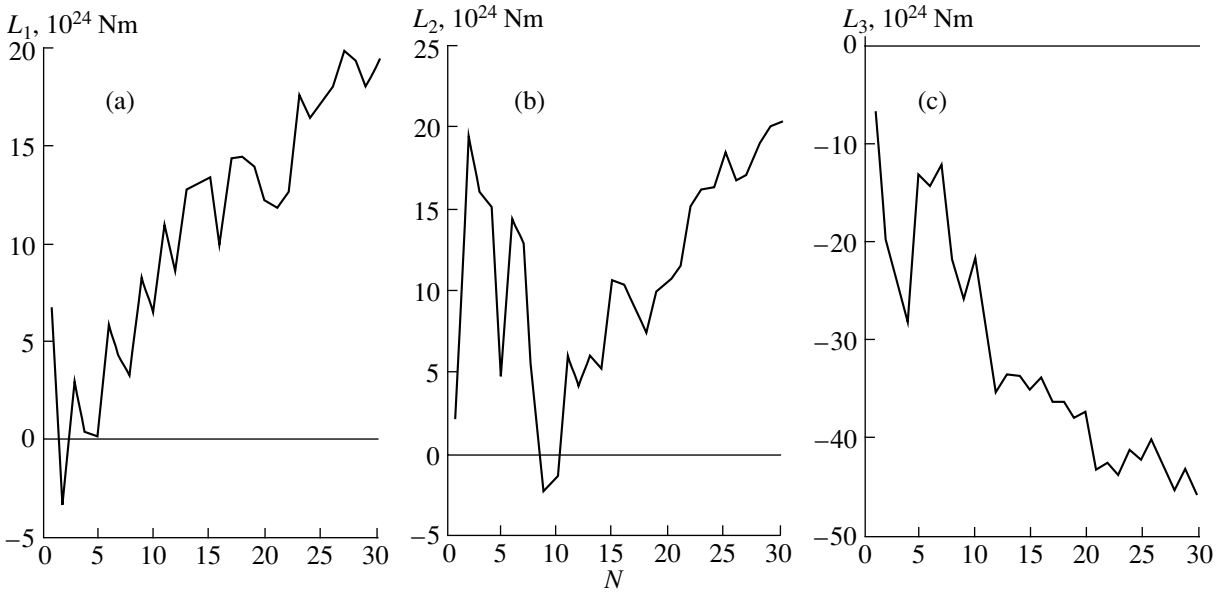

Fig. 3. Total torque (a) L_1, (b) L_2, and (c) L_3 of the crust pressing on the mantle as a function of the order N for the last term in the expansion.

nomena connected with the Earth's surface (denudation of mountains, accumulation of precipitation, global freezing, melting of glaciers, and other effects resulting from solar radiation) and phenomena occurring over the entire crustal layer (tectonic phenomena and tidal retardation).

Let us consider in more detail this last question: tidal retardation. Non-elastic tidal deformations are primarily accumulated in the Earth's hydrosphere and in layers with the lowest modules of stiffness and viscosity; i.e., in layers with the largest deformations. Therefore, the main expenditure of tidal energy should be associated with retardation in these layers, namely, in shallow epicontinental seas and lower crustal layers near the mantle.

Since tidal retardation acts only on the Earth's crust, there must be motion of the crust with respect to the mantle. Our calculations show that such rotation, indeed, exists (Fig. 4). The total longitudinal shift of the crust with respect to the mantle (the crust rotation vector coincides with the z-axis) is

$$\Delta\lambda = \frac{L_3^k}{4\pi L_0} \Big/ \sum_{n=1}^{N}\sum_{m=1}^{n} m^2 (A_{nm}^{(1)} A_{nm}^{(2)} + B_{nm}^{(1)} B_{nm}^{(2)}).$$

In the zx-plane, the latitudinal shift of the crust with respect to the mantle (the crust rotation vector coincides with the y axis) is

$$\Theta_1'' = \frac{L_2^k}{4\pi L_0 \sum_{n=1}^{N} (A_0 + S_1 - S_2)},$$

while in the yz-plane, the latitudinal shift of the crust with respect to the mantle (the crust rotation vector coincides with the $-x$ axis) is

$$\Theta_2'' = -\frac{L_1^k}{4\pi L_0 \sum_{n=1}^{N} (B_0 + S_1 + S_2)},$$

where

$$A_0 = \bar{A}_{n,1}^{(1)} \bar{A}_{n,1}^{(2)}, \quad B_0 = \bar{B}_{n,1}^{(1)} \bar{B}_{n,1}^{(2)},$$

$$S_1 = 2(n^2+n)\bar{A}_{n,0}^{(1)} \bar{A}_{n,0}^{(2)} + \sum_{m=1}^{n} \frac{2}{\delta_{m-1}} \left(\frac{n^2+n}{\delta_{m-1}} - m^2 \right) S_{mn},$$

and

$$S_2 = \sum_{m=2}^{n} \sqrt{a_{n,m-1} a_{n,m-2}}$$
$$\times (\sqrt{\delta_{m-2}} (\bar{A}_{n,m}^{(1)} \bar{A}_{n,m-2}^{(2)} + \bar{A}_{n,m}^{(2)} \bar{A}_{n,m-2}^{(1)})$$
$$+ \bar{B}_{n,m}^{(1)} \bar{B}_{n,m-2}^{(2)} + \bar{B}_{n,m}^{(2)} \bar{B}_{n,m-2}^{(1)}).$$

However, the rotation of the crust with respect to the mantle disrupts the isostatic equilibrium, and a torque L proportional to the shift arises to restore the equilibrium. Since this torque acts on the crust in the opposite sense to the crust's shift, an oscillation can arise in the Earth's crust, whose period T depends on both the moment of inertia of the crust and the physical conditions at the crust–mantle boundary (viscosity, inclination of the M surface, pressure applied on the surface).

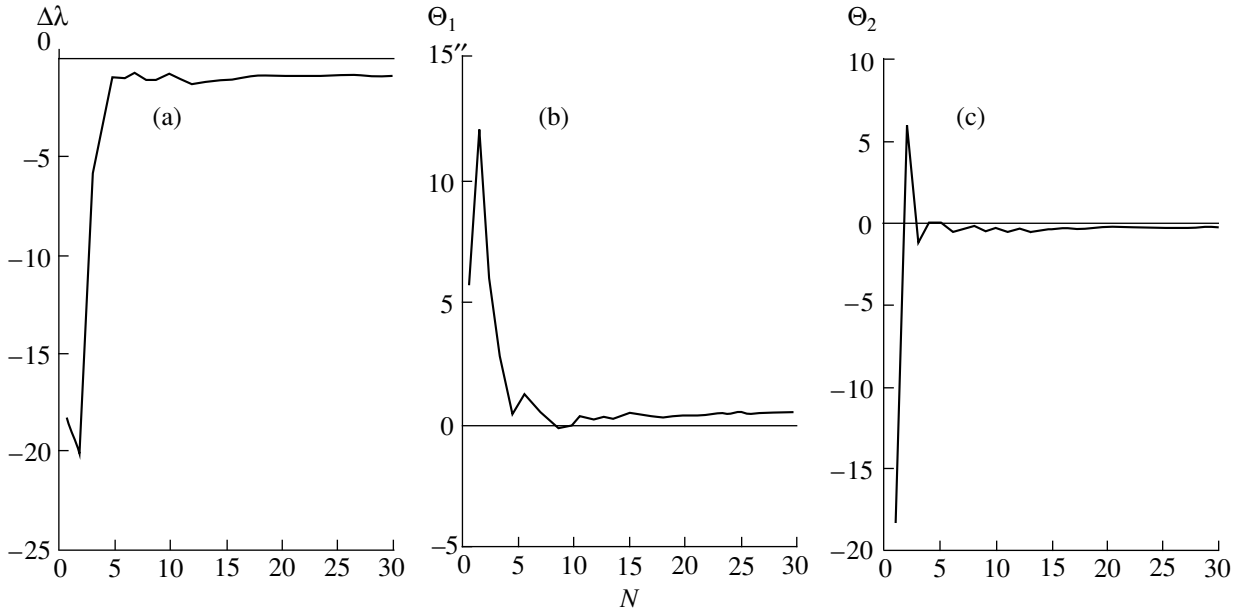

Fig. 4. Total shift of the crust with respect to the mantle as a function of the order N for the last term in the expansion: (a) longitudinal, (b) latitudinal in the plane of the Greenwich meridian, (c) latitudinal in the plane of the 90° meridian.

The presence of crustal rotation will be manifest in astronomical observations. Namely, there should be variations in the velocity of the Earth's rotation and the polar motion with respect to the Earth's surface; errors in the precession parameters could also arise.

At the present time, $L_3^k = -L_3 > 0$, $\Delta\lambda < 0$, and, together with the total tidal background deceleration in the Earth's rotation, there should be some acceleration in the rotation at the Earth's surface. This is clearly indicated by solar-eclipse data obtained over 2500 years [27]. Careful analysis of these data indicates that, currently, in addition to the overall deceleration in the Earth's rotation $\dot{\omega} = -6.1 \times 10^{-22}$ rad/s^2 due to tidal retardation, there is a significant positive acceleration $\dot{\omega} = 1.6 \times 10^{-22}$ rad/s^2. Moreover, periodic changes in the rotation velocity with a period $T \approx 1500$ yr are indicated [27].

At the present time, $L_1^k = -L_1 < 0$, $\dot{\Theta}_2'' < 0$, $L_2^k = -L_2 < 0$, and $\dot{\Theta}_1'' > 0$. Since the small quantities $\dot{\Theta}_1''$ and $\dot{\Theta}_2''$ describe the shift of the crust along the x and y axes, observations of the position of the pole should indicate a shift in the opposite direction. By virtue of the opposite signs of the torques and shifts, we should detect a corresponding deceleration in the polar motion. To reveal this phenomenon, due to its long period (probably of the order of the period of isostatic smoothing, ~10000 yr [28]), observations of the polar motion must be accumulated over a longer time interval than presently available.

Thus, there is a secular or long-term component of the motion of the crust with respect to the mantle with a period of about 10^4 yr. A periodic motion determined by the parameters of the Earth's crust as an oscillating system is also possible. According to our estimates, the period of this motion should be about 1500 yr.

The differential rotation of the crust with respect to the mantle is confirmed by the studies in [29]. An analysis of velocities of the Earth's surface in a coordinate frame fixed to so-called "hot spots" (supposed to be connected with the Earth's mantle and manifest at the surface as chains of volcanos) reveals a total toroidal component corresponding to a rotation of the crust with respect to the mantle with a speed ~1.7 cm/yr about the pole with coordinates $\varphi = -54°$ and $\lambda = 84°$ (that is, approximately opposite to the Earth's total rotation). Geological data and the physical conditions in the mantle [30] suggest that the sources of the hot spots are situated in the uppermost mantle. Therefore, the derived rotation parameters correspond to motion of the crust (not the lithosphere) with respect to the mantle.

7. CONCLUSION

Due to the gravitational fields of our Galaxy, the light from distant sources moves along curved trajectories. Consequently, the observed direction toward the light source does not coincide with the straight line connecting the source and observer. Since the Galactic gravitational fields are nonstationary, the direction of arrival of the light will also be nonstationary. In other words, the apparent position of a distant radio source on the sky will fluctuate randomly. This phenomenon is quite similar to fluctuations of the position of a star when its light is transmitted through the Earth's turbu-

lent atmosphere. The only difference is the characteristic amplitudes and times. For the case considered above, the characteristic amplitudes are of the order of 1 μarcsec and the characteristic times are of the order of tens of years.

The corresponding amplitudes can vary from 1 μarcsec to 1 mas, depending on the model for the Galaxy and the random disposition of stars near the quasar–Earth trajectories. Individual effects can have rather large amplitudes, reaching hundreds of microarcsec, although they are nonstationary phenomena with characteristic time scales from several months to several years. These processes cannot substantially influence the construction of fundamental astrometric catalogs. Nevertheless, there is a complete change of the positions of nearly all stars at a level of several microarcsec every several dozen years.

Here, we can draw an important conclusion. Astrometric catalogs of microsecond precision must be revised every 10–30 yr to establish a new celestial-coordinate reference system. In addition, the microsecond instability of the CCS limits the precision of amplitudes of the nutation harmonics.

We have also revealed a previously unstudied effect in secular and long-term variations of the ECS, due to the differential rotation of the Earth's crust with respect to the mantle. This leads to long-term and secular variations in the Earth's rotation velocity and the polar motion. The effect is confirmed by measurements of the duration of the day over 2500 yr, which indicate a secular acceleration of the rotation of the Earth's surface, in addition to the overall tidal retardation of the Earth's rotation, as well as an oscillation with period ~1500 yr.

The torque producing the relative rotation of the mantle and crust is associated with the nonsymmetrical displacement of the centers of inertia of the crust and mantle with respect to the Earth's center of inertia. This displacement creates a nonisostatic pressure of the crust on the mantle, which can produce a relative shift of the mantle as a single rigid body with respect to the less rigid crust (which acts as a system of blocks of reduced strength) if the torque due to pressure forces at the crust–mantle boundary exceeds the torque of frictional forces.

Our hypothesis of possible rotation of the crust is verified by direct calculations of the torques of the nonhydrostatic pressure of the crust on the mantle and shifts of the crust with respect to the mantle ascribed to the nonsymmetrical displacement of the centers of inertia of the crust and mantle with respect to the Earth's center of inertia.

ACKNOWLEDGMENTS

The authors thank T.G. Maksimova and S.A. Kazaryan for their assistance in the computations and in preparing the manuscript. This work was supported by the Russian Foundation for Basic Research (project nos. 97-05-64342 and 98-05-64797), the program "Russian Universities" (no. 2-5547), and the State Program "Integration" (no. K0641).

REFERENCES

1. C. Ma, E. F. Arias, T. M. Eubanks, *et al.*, Astron. J. **116**, 516 (1998).
2. *IERS Technical Note 26* (Observatoire de Paris, International Earth Rotation Service, Paris, 1998).
3. *IAU Inf. Bull.*, No. 81 (1998).
4. *IERS Technical Note 21* (Observatoire de Paris, International Earth Rotation Service, Paris, 1996).
5. J. Souchay, M. Feissel, C. Bizouard, *et al.*, Astron. Astrophys. **299**, 277 (1995).
6. M. V. Sazhin, Pis'ma Astron. Zh. **22**, 643 (1996).
7. M. V. Sazhin, V. E. Zharov, A. V. Volynkin, *et al.*, Mon. Not. R. Astron. Soc. **300**, 287 (1998).
8. G. Morits and A. Muller, *Rotation of the Earth: Theory and Observations* [in Russian] (Naukova Dumka, Kiev, 1992).
9. E. F. Arias, P. Charlot, M. Feissel, *et al.*, Astron. Astrophys. **303**, 604 (1995).
10. G. H. Kaplan, F. J. Josties, P. E. Angerhofer, *et al.*, Astron. J. **87**, 570 (1982).
11. C. S. Jacobs, O. J. Sovers, J. G. Williams, *et al.*, Adv. Space Res. **13** (11), 161 (1993).
12. W. H. Munk and G. J. F. McDonald, *The Rotation of the Earth: A Geophysical Discussion* (Cambridge University Press, Cambridge, 1960; Mir, Moscow, 1964).
13. I. A. Rezanov, A. Sh. Faĭtel'son, and G. V. Krasnopevtseva, *The Nature of the Mohorovocic Discontinuity* [in Russian] (Nedra, Moscow, 1984).
14. S.-Y. Zhu and I. I. Mueller, Bull. Geod. **57**, 29 (1983).
15. V. E. Zharov, M. V. Sazhin, and T. A. Kalinina, IGGOS Proc., Munich, 1998 (in press).
16. A. F. Zakharov and M. V. Sazhin, Usp. Fiz. Nauk **168**, 1041 (1998).
17. B. M. Lasker, C. R. Struch, B. J. McLean, *et al.*, Astron. J. **99**, 2019 (1990).
18. *The Hipparcos and Tycho Catalogues*, ESA Publication SP-1200 (1997).
19. S. A. Kaplan and S. B. Pikel'ner, *Physics of the Interstellar Medium* [in Russian] (Nauka, Moscow, 1979).
20. G. Korn and T. Korn, *Mathematical Handbook for Scientists and Engineers* (McGraw-Hill, New York, 1961; Nauka, Moscow, 1977).
21. J. M. Wahr, Geophys. J. R. Astron. Soc. **64**, 705 (1981).

22. P. M. Mathews, B. A. Buffet, T. A. Herring, *et al.*, J. Geophys. Res. **96**, 8243 (1991).
23. N. A. Chuĭkova and T. G. Maksimova, Trudy GAISh **65**, 33 (1996).
24. N. A. Chuĭkova, A. N. Grushinskiĭ, and T. G. Maksimova, Trudy GAISh **65**, 51 (1996).
25. A. M. Dziwonski and D. L. Anderson, Phys. Earth Planet. Inter. **25**, 297 (1981).
26. G. K. Duboshin, *Theory of Gravitation* [in Russian] (Gosizdat, Moscow, 1961).
27. F. R. Stephenson and L. V. Morrison, Philos. Trans. R. Soc. Lond. Ser. A **351**, 165 (1995).
28. P. J. Melchior, *Physique et dynamique planetaires* (Bruxelles, 1971; Mir, Moscow, 1976), Chap. II.
29. Y. Ricard, C. Doglioni, and R. Sabadini, J. Geophys. Res. **96**, 8407 (1991).
30. O. G. Sorokhtin and S. A. Ushakov, Itogi Nauki Tekhniki, Fizika Zemli **12** (1993).

Translated by V. Badin

Astronomy Reports, Vol. 44, No. 2, 2000, pp. 65–75. Translated from Astronomicheskiĭ Zhurnal, Vol. 77, No. 2, 2000, pp. 83–95.

Observational Manifestations of Gaseous Baryon Dark Matter

Yu. A. Shchekinov

Rostov State University, Rostov-on-Don, Russia

Received August 3, 1998

Abstract—The paper considers possible observational implications of the presence of dark matter in the Galaxy in the form of dense gas clouds—clumpuscules with masses $M_c \sim 10^{-3}\ M_\odot$ and radii $R_c \sim 3 \times 10^{13}$ cm. The existence of such clouds is implied by modern interpretations of extreme scattering events—variations in quasar radio fluxes due to refraction in dense plasma condensations in the Galactic halo. The rate of collisions between these clouds is shown to be rather high: from 1 to 10 $M_\odot$ per year is ejected into the interstellar medium as a result of such collisions. The optical continuum and 21-cm emission from hot post-collision gas could be observable. Gas clouds composed of dark matter could be formed around O stars in an H II region with radius $R \sim 30$ pc and emission measure EM $\simeq 20$ cm^{-6} pc. They could also be observable in the H_α line. The evaporation of clumpuscules by external ionizing radiation could be a substantial source of matter for the interstellar medium. Assuming that the total mass of matter entering the interstellar medium over the Hubble time does not exceed the mass of luminous matter in the Galaxy, upper limits are found for the cloud radii ($R_c < 3.5 \times 10^{12}$ cm) and the contribution of clouds to the surface density of the Galaxy (<50 $M_\odot$ pc^{-2}). Dissipation of the kinetic energy of matter lost by clumpuscules could provide an efficient mechanism for heating gas in the Galactic halo. © *2000 MAIK "Nauka/Interperiodica".*

1. INTRODUCTION

The idea that hidden mass in the Galaxy could be in the form of baryons has recently obtained convincing observational support after the discovery of microlensing events by massive compact halo objects (MACHOs) [1–3]. The nature of such objects is under discussion. However, it is clear from general considerations that they could be low-mass ($M \sim 10^{-3}\ M_\odot$) stars (brown dwarfs, or "jupiters," as they are also called): Due to their low mass (below the hydrogen ignition limit), they have low luminosities and are optically invisible, but they are sufficiently massive to provide the observed characteristics of gravitational microlensing events. It is not excluded that microlensing events with the observed rate could be associated with red dwarfs ($M \gtrsim 0.08\ M_\odot$), whose total mass is several times larger than the total mass of stars in the Galaxy [4].

Gaseous atomic and molecular clouds maintained in equilibrium by external pressure or self-gravitation [5–14] have recently been discussed as an alternative type of MACHO. In contrast to brown dwarfs, such clouds are expected to have very low temperatures (from 3 K [6] to 10 K [14]), so that they cannot be detected even at infrared wavelengths. These clouds would have surface densities from $\sim 3 \times 10^{23}$ cm^{-2} [11] to 10^{25} cm^{-2} [13] and are therefore also opaque in the 21-cm line. From this point of view, detecting them presents a serious observational problem.

De Paolis *et al.* [7] showed that the existence of baryonic gas clouds of dark matter in the Galactic halo could be betrayed by gamma-ray radiation generated when they interact with cosmic rays. Recently published statistical data indicate the presence of large-scale anisotropy in the background gamma-ray radiation [15], whose flux at high energies (>1 GeV) is close to that predicted in [7]. These data may provide evidence for the existence of dark matter in the form of dense gas clouds.

Another possible observational manifestation is associated with optical (nongravitational) lensing of the radio emission of quasars passing through ionized gas surrounding dense clouds of baryonic dark matter. Significant short-time scale (of the order of weeks or months) variations of the radio fluxes of quasars—so-called extreme scattering events—were first detected more than 10 years ago at 3.7 and 11 cm [16]. These variations are due to refraction of the radio waves in dense plasma clouds passing through the line of sight toward the observed quasar [16, 17]. The sizes (of the order of several AU) and electron densities n_e (about 10^3 cm^{-3}) of the regions of plasma giving rise to the lensing were derived based on the characteristics of the 3.7 and 11-cm radio emission. These regions appear to be H II regions maintained by the background UV radiation. The gas pressure in these regions, $n_e T_e \sim 10^7$ K cm^{-3}, is three to four orders of magnitude higher than the pressure in the surrounding interstellar gas. Therefore, they could be transient formations with characteristic lifetimes of several months, which would obviously mean that they could not explain the observed extreme scattering events.

1063-7729/00/4402-0065$20.00

Recently [18], a possible resolution for this paradox has been proposed: The lensing plasma regions are envelopes of ionized hydrogen surrounding dense, gravitationally bound molecular clouds [9]. In this case, the high pressure in these regions leads to a steady-state outflow of ionized gas from the outer layers of the dense molecular clouds, so that the electron distribution in the lensing region does not change. The mass content in the clouds is high enough to compensate the mass outflow on time scales comparable with the lifetime of the Galaxy. In [18], these clouds were identified with dense molecular regions—the so-called "clumpuscules" described in [5, 6] with $R_c \sim$ several AU and $M_c \sim 10^{-3}\ M_\odot$. Walker and Wardle [18] were able to accurately reproduce the profiles of radio-flux variations in the quasar 0954 + 658 at both observed wavelengths, which had long remained an unsolved problem in interpretions of extreme scattering events.

More recently, the idea that such clouds (clumpuscules) could contribute significantly to the dark matter has received further support: It has been shown [19] that clumpuscules are able to (non-gravitationally) lens stellar radiation at optical wavelengths, which could account for the excess of microlensing events observed toward the Small Magellanic Cloud. In the present paper, we consider additional implications of the existence of dark matter in the form of dense molecular clouds. We call these clouds DM clouds, or, in accordance with [13], clumpuscules.

In Section 2, we discuss the general properties of the population of DM clouds in the Galaxy, which can be estimated from the results obtained in [18]. A qualitative picture for collisions between DM clouds is considered in Section 3. Estimates of the optical emission from colliding clumpuscules are given in Section 4, and we estimate the characteristics of the 21-cm line emission from clumpuscule fragments after a collision in Section 5. In Section 6, we consider the H_α line emission from the envelopes of ionized gas around DM clouds. Possible implications of the existence of molecular clumpuscules for the gaseous halo of the Galaxy are discussed in Section 7. Finally, we analyze our results in Section 8.

2. GENERAL PROPERTIES OF DM CLOUDS

The parameters of molecular DM clouds suggested in [4, 5] correspond to rather high masses (about an order of magnitude higher than those for the visible matter), low luminosities, and long lifetimes (comparable to the Hubble time). It follows that the masses of such objects should be close to the mass of Jupiter ($M_c \sim 10^{-3}\ M_\odot$), while the densities, temperatures, and dimensions of the clouds should correspond to the gravitational stability limit: $n_c \sim 10^{11}$ cm^{-3}, $T_c \sim 3$ K, and $R_c \sim 10^{14}$ cm. The interpretation of extreme scattering events suggested in [18] has yielded similar values for the radii of DM clouds: The duration of extreme scattering events (of the order of two months) suggests that $R_c \lesssim 3 \times 10^{14}$ cm, assuming that the cloud velocity perpendicular to the line of sight has an upper limit of 500 km/s. Another observable quantity—the rate of occurrence of extreme scattering events—can be used to estimate the covering factor for such clouds, i.e., the fraction of the celestial sphere that is covered by the clouds: $f \sim 5 \times 10^{-3}$ [16]. This, in turn, can be used to determine the contribution of molecular clumpuscules to the surface density of the Galaxy [18]: $\Sigma \sim fM_c/\pi R_c^2$, where M_c is estimated from the condition of hydrostatic equilibrium, $M_c \sim kT_cR_c/Gm_p$. In this way, assuming that $T_c \gtrsim 3$ K, Walker and Wardle [18] obtained $\Sigma \gtrsim 10^2\ M_\odot$ pc^{-2}, which is close to estimates based on dynamical considerations [20].

The characteristic mean free path for DM clouds with respect to their collisions with each other is estimated to be r_0/f, where r_0 is the characteristic size of the region occupied by the clouds. Taking $r_0 \sim 10$ kpc, we find for the characteristic time between collisions $\gtrsim 10^{10}$ yr. Since the masses and densities of the clouds are large, disruption of the clouds by the ionizing background UV radiation is also a fairly slow process, with the same characteristic time scale. Because contact interactions between the DM clouds and interstellar-gas clouds are inefficient, owing to the large difference in their densities, Walker and Wardle [18] conclude that the population of DM clouds is dynamically stable over the Hubble time scale t_H. At the same time, even such slow processes disrupting the DM clouds could have significant consequences, due to the large total mass contained in these clouds.

For the sake of definiteness, we will assume that the distribution of DM clouds in the Galaxy is described by the law

$$\mathcal{N} = \frac{\mathcal{N}_0}{1 + (r/r_0)^2}, \tag{1}$$

which, at $r > r_0$, gives a distribution corresponding to a singular isothermal sphere (we consider r_0 to be a free parameter). Here, $\mathcal{N}_0$ is the number of clouds per unit volume at the center of the Galaxy. The number of collisions between DM clouds per unit time in unit volume is

$$\nu = \pi R_c^2 \mathcal{N}^2 v_c, \tag{2}$$

where we have assumed for simplicity that all clouds have the same velocity v_c irrespective of their position in the Galaxy. Unless otherwise specified, we use $R_c = 3 \times 10^{13}$ cm and $v_c = 250$ cm s^{-1} in numerical estimates. The total number of collisions in the Galaxy per unit time,

$$\nu_G = 4\pi \int_0^\infty \nu(r) r^2 dr = \pi^3 R_c^2 r_0^3 \mathcal{N}_0^2 v_c, \tag{3}$$

can be expressed in terms of the characteristic covering factor for the DM clouds, $f \sim \pi^2 \mathcal{N}_0 R_c^2 r_0$:

$$\nu_G \sim \frac{4}{\pi} \frac{r_0 v_c}{R_c^2} f^2.$$

For the above value $f \sim 5 \times 10^{-3}$, this gives $\nu_G \sim 10^{-26} r_0\ \mathrm{s}^{-1}$, or $\nu_G \sim 10^3$–$10^4\ \mathrm{yr}^{-1}$ for $r_0 = 1$–10 kpc, and the total number of clumpuscules N in the Galaxy could be as high as 10^{13}–10^{15}. Note that, for the given characteristic scale of the cloud distribution r_0 and a fixed total number of clouds N, their contribution to the surface density is proportional to the cloud radius ($\Sigma \sim kT_c N R_c / \pi G m_p r_0^2$), while for a fixed observed covering factor, it is inversely proportional to the radius R_c; i.e., $\Sigma \sim f R_c^{-1}$. Thus, the amount of matter in molecular clumpuscules passing through shock waves resulting from collisions is $\sim \nu_G M_c \sim 1$–$10\ M_\odot\ \mathrm{yr}^{-1}$. This is comparable to or exceeds the typical amount of matter involved per unit time in such Galactic processes as the conversion of interstellar gas into stars, heating of gas by shock waves from supernova explosions, and settling of gas from the Galactic halo onto the Galactic plane. We, therefore, expect that collisions between molecular DM clouds have appreciable consequences for the physics of the interstellar gas and are observable.

3. DYNAMICS OF COLLISIONS OF DM CLOUDS

In this section, we will qualitatively describe the dynamics of collisions of DM clouds. A detailed description based on numerical simulations performed in the framework of two-dimensional gas dynamics will be presented in a separate paper. We consider here a head-on collision of two clouds of equal mass, in which the velocities of the clouds are directed along the axis connecting their centers. We will first ignore the effects of self-gravitation. In the center-of-mass coordinate system, a contact discontinuity arises in the symmetry plane, from which two shock waves spread. The subsequent picture is symmetric with respect to this discontinuity. The characteristic duration of the collision—i.e., the time for the shock to reach the cloud surface opposite to the contact discontinuity—is $\tau_s \sim R_c / v_c \sim 0.4$ yr for the parameters indicated above. Because the post-shock gas density is rather high ($n_s = 4 n_c \sim 4 \times 10^{12}\ \mathrm{cm}^{-3}$), the time for radiative cooling due to deceleration processes does not exceed $\tau_R \sim 3$ s. However, hard radiation emerging from the region bounded by the shock waves is absorbed on scales $\sim 10^6$ cm, and by time $\sim 10^5$ s, when the shock encompasses about 1–2% of the cloud material, the gas in the cloud becomes ionized ($x \sim 1$), so that the optical depth to Thomson scattering is $\tau_T \sim 20$. On these grounds, we will ignore radiative losses.

Owing to the high pressure behind the shock front ($P_s \sim \rho_c v_c^2 \sim 10^3$ erg cm^{-3} ($\sim 10^{19}$ K cm^{-3})), there is a strong gas outflow along the symmetry plane immediately after the collision. This outflow reduces the pressure and temperature in this region and, over the collision time $t \sim \tau_s$, carries away a significant fraction of the cloud mass from the interaction region. This effect was first described by Stone [21] and was subsequently confirmed in [22–26]. For diffuse interstellar clouds with significant radiative cooling, the fraction of dispersed mass is estimated to be about 25%. In the adiabatic case (i.e., when we disregard radiative losses), this fraction could be somewhat higher due to the higher pressure. We emphasize, however, the approximate character of these estimates: The latest high-resolution calculations [26] have demonstrated that, at later stages after the collision (i.e., on time scales exceeding 10–15 dynamical times), Rayleigh–Taylor instability develops. As a result, clumps and filaments are formed, which can, in turn, increase the fraction of dispersed mass.

After the shock reaches the outer boundary of the cloud, a rarefaction wave begins to spread, causing the cloud to expand at the local sound speed [21]. At time $t \lesssim \tau_s$, the rarefaction wave reaches the symmetry plane and produces a reflected wave. The subsequent interaction of the reflected wave and the stream formed by the initial rarefaction wave decreases the rate of outflow from the symmetry plane, so that the stream behind the reflected beam turns out to be subsonic. By the time the reflected wave reaches the outer boundary of the cloud, the pressure in these regions has become equal to the pressure in the surrounding gas. As a result, the pressure behind the reflected wave ends up being lower than the surrounding pressure, and the secondary reflected wave becomes a compression wave. Due to this sequence of waves following a series of oscillations, the clouds separate, and the pressure in the clouds becomes equal to the surrounding pressure. Since viscous dissipation plays a significant role in the cloud collision behind the shock front, the entropy increases and the process is inelastic, even in the absence of radiative cooling. As a result, after the clouds separate, the cloud pressure becomes equal to the surrounding pressure at a gas density lower than the initial density; equilibrium is established along a Poisson adiabat with higher entropy than that for the clouds before the collision.

Up until now, we have ignored self-gravitation; its effect on the dynamics of the collision process is small because the kinetic energy of the collision substantially exceeds the gravitational energy of the clouds. Self-gravitation itself is important for molecular clumpuscules only in the unperturbed state (i.e., before the cloud collision), since it can maintain high densities in clouds over Galactic time scales, as suggested in [5, 6]. However, the picture changes radically after collision. Since the dissipation at the shock front increases the gas entropy, after the collision, the heat energy of the clouds exceeds their gravitational energy, and even

though the clouds were in gravitational equilibrium before the collision, they expand freely after the collision on account of the pressure excess. If the cloud is transparent to the external heating radiation at the end of the expansion or in the preceding stages, its expansion will occur in an isothermal (or nearly isothermal) regime, so that the cloud material will mix with the surrounding gas.

The fundamental difference of the gas dynamics in colliding clumpuscules from the picture described in [21–26] is that the radiative pressure dominates behind the shock front. As indicated above, in view of the large gas densities in clumpuscules, the Thomson optical depth quickly reaches unity, and we can take the gas and radiation behind the shock front to be in equilibrium. In this case, the gas pressure behind the front is

$$P = \frac{\mathcal{R}}{\mu}\rho T + \frac{4}{3}\sigma_{SB}T^4, \quad (4)$$

where $\mathcal{R}$ is the universal gas constant and σ_{SB} [in erg cm^{-3} K^{-4}] is the Stefan–Boltzmann constant. On the other hand, $P = \rho_0 D^2(1-\eta)$, where $\eta^{-1} = \rho/\rho_0$ is the gas compression factor and D is the shock velocity in the center-of-mass coordinate frame. It can readily be shown that the solution of (4) when $v_c = 250$ km s^{-1} is $T \simeq 2.8 \times 10^4$ K; the contribution of the gas pressure to the total pressure, which is determined by the first term in (4), is ~0.01 for $n_c = 10^{12}$ cm^{-3}. The degree of ionization of the gas, which is determined under such conditions by the Saha formula, is $x = 1$ (or, more precisely, $1 - x \simeq 6 \times 10^{-7}$). The diffusion of radiation in the gas ahead of the shock wave smears the shock front [27] on scales of the order of several photon mean free paths; i.e., in our case, on scales $\sim 10^{-2} R_c$. In this sense, the qualitative pattern of the dynamics of the shock wave passing through the cloud and the subsequent separation of the clouds is similar to that described in [21]. The sound speed behind the front is given by the formula

$$c_s = \frac{2}{3}\frac{\sigma_{SB}^{1/2}T^2}{\rho^{1/2}} \quad (5)$$

and, for the parameters adopted above, is equal to $c_s \simeq 0.7 \times 10^7$ cm s^{-1}.

4. OPTICAL EMISSION

For $v_c \gtrsim 15$ cm s^{-1} (i.e., for $n_c \sim 10^{12}$ cm^{-3}), the post-shock gas temperature is

$$T_s \simeq 2.8 \times 10^4 \left(\frac{v_c}{250\ \mathrm{km\ s^{-1}}}\right)^{1/2} \mathrm{K}.$$

At lower collision rates, the contribution of the radiative pressure behind the shock front is lower than the gas pressure; as a result, the temperature is determined by the formula

$$T_s \simeq 2.5 \times 10^6 \left(\frac{v_c}{250\ \mathrm{km\ s^{-1}}}\right)^2 \mathrm{K}.$$

After the radiation emerging from the central regions of the cloud compressed by the shock wave has ionized the gas ahead of the shock front, the optical depth of the cloud to Thomson scattering becomes $\tau_T \sim \sigma_T R_c n_c \sim 20$. The luminosity of the hot gas during a collision of DM clouds is determined by the diffusion of photons from the interior of the hot gas and is given by the formula

$$L_h \simeq \sigma_{SB}\tau_T^{-1} c T^4 S,$$

where $S \sim 2\pi R_c^2$ is the area of the emitting surface. For the adopted parameters, we have $L_h \simeq 3 \times 10^{38}$ erg s^{-1}. The duration of the hot stage is determined by the expansion of the compressed gas after the shock reaches the outer cloud surface and the rarefaction wave begins to propagate inward: $t_d \sim R_c/3c_s \sim 3 \times 10^6$ s. The total energy loss via radiation is $L_h t_d \sim 2 \times 10^{44}$ erg, which is 30% of the total kinetic energy of the clouds.

In terms of their observational manifestations, the colliding DM clouds are short-lived at these stages ($t \sim t_d \sim 10$ days), and they have temperatures and luminosities typical for massive stars. The total number of such objects in the Galaxy is $\nu_G t_d \sim 80\ (r_0/1\ \mathrm{kpc})$. Only a small fraction,

$$\sim 2\pi^{-1}\arctan(r/r_0),$$

is in the region with Galactocentric radius less than r, and can, therefore, be shadowed by dust in the central parts of the Galaxy. For example, the fraction within $r < 1$ kpc, at $r_0 = 1$ kpc, is 0.5 (i.e., the total number of colliding clouds at the hot stage located outside this region is ~40 in this case) while at $r_0 = 10$ kpc, it is merely 0.5. In general, the dependences of the observed characteristics of colliding DM clouds on their parameters (for $v_c \geq 100$ km s^{-1} and $n_c \sim 10^{12}$ cm^{-3}) are determined by the following formulas:

total number of clouds in the hot phase

$$N_h = \frac{6}{\pi}\left(\frac{1-\eta}{\eta}\right)^{1/2} f^2 \frac{r_0}{R_c} \simeq 80\left(\frac{r_0}{1\ \mathrm{kpc}}\right)\left(\frac{R_c}{3\times 10^{13}\ \mathrm{cm}}\right)^{-1},$$

cloud luminosity

$$L_h = \frac{2\pi\eta^2}{1-\eta}\frac{m_p v_c^2 R_c c}{\sigma_T}$$

$$\simeq 7.5 \times 10^{37}\left(\frac{R_c}{3\times 10^{13}\ \mathrm{cm}}\right)\left(\frac{v_c}{250\ \mathrm{km\ s^{-1}}}\right)^2 \mathrm{erg\ s^{-1}},$$

cloud temperature

$$T_h \simeq \left[\frac{\eta^2}{1-\eta}\frac{\rho_0 v_c^2}{\sigma_{SB}}\right]^{1/4}$$

$$\simeq 2.8 \times 10^4 \left(\frac{n_c}{10^{12}\ \mathrm{cm^{-3}}}\right)^{1/4}\left(\frac{v_c}{250\ \mathrm{km\ s^{-1}}}\right)^{1/2} \mathrm{K}.$$

In these estimates, we adopt $\eta \simeq 1/6$. The detection of such objects (or, conversely, failure to detect them at a given sensitivity level) would make it possible to estimate the parameters of the DM clouds and their contribution to the surface density of the Galaxy.

5. 21-CM LINE EMISSION

Order-of-magnitude estimates of the 21-cm line emission after a collision between clouds can be obtained if we assume that the cloud as a whole expands after the shock reaches its outer boundary. In this case, the gas initially expands adiabatically with index $\gamma = 4/3$:

$$P = P_1(\rho/\rho_1)^{4/3}.$$

Here, the subscript "1" specifies quantities at the time of maximum compression ($P_1 = 4\sigma_{SB}T_1^4/3$, $T_1 = 2.8 \times 10^4$ K, and $\rho_1 = \rho_c/\eta$). As the gas expands, the radiation temperature varies as $T \propto R^{-1}$. The gas temperature varies in the same way, as long as the optical depth to Thomson processes $\tau_T > 1$. Since the expansion of the cloud after the collision is appreciably three-dimensional, it is reasonable to suppose that the gas density ρ varies as R^{-3}. Thus, the gas pressure P_g and radiation pressure P_γ vary in the same way ($\propto R^{-4}$), and the initial relation between these pressures, $P_g/P_\gamma \simeq 0.01$, breaks down only when the electron density decreases so much that $\tau_T < 1$. If the degree of ionization up until then is determined by the Saha formula, we can show that the time $\tau_T = 1$ corresponds to the temperature $T_2 = 5.8 \times 10^3$ K, for which $n_2 = 0.016$, $n_1 \simeq 10^{11}$ cm^{-3} and $x = 0.12$. At this time, the density of neutral hydrogen along the line of sight to the cloud is $N_2(\mathrm{HI}) \simeq 6 \times 10^{23}$ cm^{-2}. Note that hydrodynamical instabilities lead to a nonuniform density distribution in the cloud and its fragments, but the differences in density between different regions on time scales $t > 50$–60 dynamical times does not exceed factors of three to four [26]. This means that the qualitative picture adopted by us, based on the assumption of a uniform distribution of matter after the collision, provides correct estimates to order of magnitude.

The ensuing gas expansion is adiabatic, with $\gamma = 5/3$, and for $n_3 = 10^6$ cm^{-3}, the gas temperature is $T_3 = 3$ K. The duration of this stage is $\sim R_3/c_s \sim 2 \times 10^{11}$ s, where $R_3 \sim (n_1/n_3)^{1/3}R_c$ is the characteristic size of the cloud (for the adopted numerical values, $R_3 \sim 10^{15}$ cm). Based on an analysis of turbulent motions in a neutral gas, Kalberla and Kerp [28] argued in favor of the existence of such cold clouds in the Galactic halo. The further expansion of the cloud is isothermal at a temperature $T = 3$ K, which is maintained by inelastic processes of collisional deactivation of the fine-structure levels of the hydrogen atoms, $F = 1 \longrightarrow F = 0$ at a rate $q_{10} = 3 \times 10^{-11}T^{1/3}$ cm^3 s^{-1} [29]; the corresponding characteristic time is $t_{10} \sim 2 \times 10^4$ s. The isothermal expansion ends when the gas density decreases to $n_4 \sim 3 \times 10^3$ cm^{-3} and the gas pressure becomes equal to the pressure of the surrounding gas. Further evolution is determined by heating of the gas by background X-ray radiation over a characteristic time scale $t_X \sim 4 \times 10^{11}$ s (we have adopted the heating rate per atom $\Gamma_X \simeq 10^{-27}$ erg s^{-1} atm^{-1} from [30]). The subsequent expansion is slow, with the characteristic time scale t_X. During these stages, as the temperature rises, the cloud becomes transparent to the 21-cm line, with a characteristic surface density $N(\mathrm{H\ I}) \sim 10^{19}$ cm^{-2}, which occurs at $t = t_{\mathrm{H\,I}} \sim 10^{13}$ s, when $n = n_5 \sim 10^3$ cm^{-3}. It is likely that, after a time $t_{\mathrm{H\,I}}$, the cloud mixes with the interstellar gas and ceases to be distinguishable. The total number of such clouds in the Galaxy, $\nu_G t_{\mathrm{H\,I}}$, is estimated to be $3 \times (10^8$–$10^9)$, and their total mass is $3 \times (10^5$–$10^6)\ M_\odot$ for $r_0 = 1$–10 kpc. They are characterized by a large velocity dispersion, which is close to the velocity dispersion v_c of the DM clouds (for a Maxwellian DM-cloud velocity distribution, the mean velocity of the centers of mass for pairs of clouds is $\sim\sqrt{3/2}\,v_c$). This fact can be used to identify such clouds and distinguish them from the general neutral-hydrogen background, the local velocity dispersion of which is much smaller than $v_c \sim 250$ km s^{-1}. Note, however, that, due to viscosity, the mixing of cloud fragments with the interstellar gas is accompanied by the conversion of the kinetic energy of these fragments to heat. As a consequence, some fraction of the fragmented material is heated to high temperatures and will not be seen in the 21-cm line emission.

As shown in [31], the force that slows the motion of the gas clouds through the intercloud medium is proportional to the dynamical pressure—i.e., to the square of the velocity ($\propto \rho_i v_c^2 R_c^2$)—even for subsonic motion. In this case, the cloud velocity drops over a scale $l_d \sim \delta R_c$, where δ is the density contrast (i.e., the ratio of the density of the cloud to the density of the surrounding gas) [32]. The cloud fragments become transparent to the 21-cm line when the number density of particles n_5 reaches 10^3 cm^{-3}; i.e., when the cloud size R_4 becomes $\sim 10^{16}$ cm. Thus, the deceleration length $l_d \sim 30$–300 pc if the density of the surrounding gas is $n_i \sim 0.1$–0.01 cm^{-3}, and the characteristic deceleration time $t_d \sim 3 \times (10^{12}$–$10^{13})$ s is comparable to t_{HI}. This means that, during the final stages, the evolution of the gas of cloud fragments depends appreciably on the environment; but, in any case, the duration of the stage when these fragments can be observed in the 21-cm line is close to the estimate of $t_{\mathrm{H\,I}}$ adopted above. During these stages, before they mix with the surrounding gas, clumpuscule fragments form a network of filaments with a covering factor of the order of ~ 0.01–0.3, so that they resemble the small-scale atomic structures described in [33].

Smaller DM clouds ($R_c \lesssim 3 \times 10^{12}$ cm) have smaller Thomson optical depths and may be transparent to the cooling radiation on account of the nonuniform density distribution generated by hydrodynamical instabilities [26]. In this case, as indicated in [34], they quickly cool after collision, so that the hot phase turns out to be very short. However, the dynamics of the subsequent expansion at stages when the temperature drops to several thousand degrees are qualitatively close to the scenario described above, since the clouds have higher densities at this pressure.

6. H_α EMISSION FROM ISOLATED DM CLOUDS

By isolated clouds, we mean separate clouds that are not involved in collisions with other clouds, but are located in a stellar radiation field. The gas in the ionized envelopes of clumpuscules has a temperature of about $T \sim 10^4$ K, which, at electron densities $n_e \sim 10^3$ cm^{-3} gives pressures three to four orders of magnitude higher than in the surrounding gas. In this case, the envelope gas expands freely at the rate $u_0 = \sqrt{2/\gamma - 1}\,c_0$, where $c_0 \simeq 10$ km s^{-1} is the sound speed in the H II envelope. As a result, the envelopes of the DM clouds are in a regime of steady-state outflow, with the density and velocity-field distributions described by the equations (see, for example, [35]):

$$\rho u r^2 = \rho_0 u_0 R_c^2,$$

$$\frac{u^2}{2} + \frac{P_0}{\rho_0}\ln\frac{\rho}{\rho_0} = \frac{u_0^2}{2},$$

$$P = P_0\frac{\rho}{\rho_0},$$

from which we easily obtain a solution for the density in the form

$$\left(\frac{\rho}{\rho_0}\right)^2\left[1 - \frac{2}{5}\ln\frac{\rho}{\rho_0}\right] = \left(\frac{R_c}{r}\right)^4. \qquad (6)$$

Hence, we find the electron density $n_e \propto \rho$, with the limiting value n_{e0} for $r = R_c$, which is determined from the equation of ionization equilibrium

$$4\pi\alpha_r R_c^3 n_{e0}^2 \int_1^\infty \left(\frac{\rho}{\rho_0}\right)^2 \zeta^2 d\zeta = 4\pi R_c^2 J,$$

where $\zeta = r/R_c$, J [cm^{-2} s^{-1} ster^{-1}] is the intensity of the Lyman-continuum radiation, and α_r is the recombination coefficient. Using (6) yields

$$n_{e0} \simeq \sqrt{\frac{2J}{\alpha_r R_c}}$$

and the emission measure corresponding to the envelope around an individual cloud:

$$\mathrm{EM} = \int_{R_c}^\infty n_e^2 dr = 0.236 n_{e0}^2 R_c = 1.8 \ \mathrm{cm}^{-6} \ \mathrm{pc},$$

where we have adopted for the Lyman-continuum intensity the estimate $J = J_0 \simeq 10^6$ cm^{-2} s^{-1} ster^{-1} [36] obtained for conditions at high Galactic latitudes, so that the intensity of H_α photons is $\simeq 1$ Rayleigh (1 Rayleigh = $10^6/4\pi$ photons cm^{-2} s^{-1} ster^{-1}). This is an order of magnitude larger than the value derived in [37] for high-velocity H I clouds. However, due to their small angular dimensions, the fluxes of H_α photons from distant DM clouds at $d > 1$ pc with angular sizes $\Delta\phi < 0.2'$ are too small to be detected. At the same time, the H_α emission characteristics of clouds at $d \sim 0.003$ pc with angular sizes $\Delta\phi \sim 7'$ are comparable to those of high-velocity H I clouds, and could be detectable in H_α line observations. For the above parameters and $r_0 = 1$ kpc, a volume with radius 0.03 pc in the solar neighborhood contains, on average, one DM cloud. For $r_0 = 10$ kpc, one cloud is located in a volume with radius 0.07 pc; its angular size decreases to ~3' and the flux of H_α emission decreases by a factor of five.

Clumpuscules located near hot stars beyond their dense H II zones, where the intensity of ionizing photons $J \gg J_0$, could have significantly higher emission measures. For O7 stars, this condition is satisfied at distances $r < 30$ pc. In this case, the emission measure from the H_α envelope increases as J/J_0, and at distances ~1 pc from the star, the cloud could be observed as a compact H_α nebula. This possibility was first indicated in [12, 18]. However, owing to the small angular dimensions of the clouds (~0.1" for a cloud about 100 pc from the Sun), the expected fluxes turn out to be very small: $F_{H_\alpha} \sim 3 \times 10^{-3}$ photons cm^{-2} s^{-1} for an individual cloud 1 pc from an O7 star. In the general case, the total number of H_α photons emitted by a separate cloud is

$$L(r) \simeq 0.025\frac{\mathcal{L}R_c^2}{r^2} \ \text{photons s}^{-1}, \qquad (7)$$

where $\mathcal{L}$ is the number of ionizing photons emitted by the exciting star and r is the distance between the cloud and the star. The size of the region near the star where the flux of photons from the star exceeds the background flux is

$$R_m = \sqrt{\frac{\mathcal{L}}{4\pi J_0}}.$$

For an O7 star, $R_m \simeq 30$ pc. The total number of H_α photons emitted by DM clouds in the region $r \le R_m$ is then determined by the formula $L_m = 4\pi\mathcal{N}\int_0^{R_m} L(r) r^2 dr$, i.e.

$$L_m = 0.3\frac{\mathcal{L}^{3/2}R_c^2\mathcal{N}}{\sqrt{4\pi J_0}} \ \text{photons s}^{-1}.$$

For the numerical values taken above, we find $\simeq 7 \times 10^{44}$ photons s^{-1}; however, the corresponding mean surface brightness is extremely low: The equivalent emission measure is only EM $\simeq 0.0025$ cm^{-6} pc.

One possible observable manifestations of DM clouds is related to the fact that the ionized gas flowing from their envelopes fills the surrounding space and, for sufficiently high outflow velocities, these surrounding regions could have a high gas density and be observable. The rate of outflow from H II envelopes grows substantially in the vicinity of hot stars, so that such stars could be surrounded by a halo of glowing ionized gas. In order to estimate this effect, we write approximate equations for the mass balance in a unit volume a distance r from the star in the form

$$\frac{\partial}{\partial r}(\rho u) = \mathcal{N}\dot{M}_c(r)r^2, \qquad (8)$$

where $\dot{M}_c = 2\pi R_c^2 m_p n_{e0}(r) u_0$ is the rate of mass loss by an individual cloud (here, we have taken into account the fact that the cloud is ionized by the star from only one side) and $n_{e0}(r) = 4.8 \times J^{1/2} R_c^{-1/2}$, so that $n_{e0} \propto r^{-1}$, since $J \propto r^{-2}$.

Note that ~10^6–10^7 clouds are near the star in the region with radius $r \sim 10$ pc at a given time, so that our assumption of a steady-state mass and energy balance is well founded. Integration of equation (8) over r then yields

$$m_p n u = \mathcal{N}\dot{M}_c(r)r$$

or, finally,

$$n = 8.5 \times 10^6 \mathcal{L}^{1/2} R_c^{3/2} \mathcal{N} \frac{u_0}{u}. \qquad (9)$$

This equation must be supplemented by the Bernoulli equation and energy balance equation. Below, we will demonstrate that the pressure in the regions filled with the H II envelope gas is much higher than the pressure of the surrounding gas. We can, therefore, assume that the rate of gas outflow from these regions u does not depend on r and, up to a factor $\sqrt{2/\gamma - 1}$, is equal to the sound speed, which is determined by the energy balance. We can readily seen that, in this case, n = const.

The energy balance, in turn, is determined by heating of the gas by ionizing radiation from the central star, as well as by its interaction with the high-velocity ionized gas flowing out from the clouds and by radiative cooling. The mean velocity of the gas lost by the clouds relative to the gas filling the space around the star is approximately equal to the characteristic velocity of motion of clouds in the Galaxy v_c, which implies that the heat released to deceleration of the lost gas could be significant (~10^{14} erg g^{-1} for $T \sim 10^6$ K). In this case, the equation of energy balance can be written in the form

$$H_{UV}(T)n^2 + \frac{1}{2}\mathcal{N}\dot{M}_c v_c^2 = \Lambda(T)n^2, \qquad (10)$$

where $H_{UV}(T)n^2$ is the rate of heating by the stellar UV radiation; $H_{UV}(T) = \alpha_r(T)\varepsilon_0$, $\alpha_r(T)$ is the recombination rate, ε_0 is the average energy received by electrons of hydrogen atoms ionized in the ground state [29, 38], and $\Lambda(T)$ is the radiative-loss rate. Assuming that the DM clouds are composed of primordial material [6, 13], we can assume that the cooling at temperatures from 10^4 to 10^6 K is determined by free–bound transitions in the hydrogen–helium mixture at a rate $\Lambda(T) \simeq 9.5 \times 10^{-17} T^{-3/2}$ erg cm^3 s^{-1} at $T = 10^4$–6×10^4 K and $\Lambda(T) \simeq 3 \times 10^{-21} T^{-1/2}$ at $T = 6 \times 10^4$–10^6 K [29]. Eliminating the gas density from (9) and (10) and assuming that the velocity u is equal to the rate of steady-state outflow to the vacuum ($u = \sqrt{2/\gamma - 1}\, c_s$), we find that the temperature varies from $T \simeq 10^4$ K at $r = 1$ pc to $T = 5 \times 10^4$ K at $r = 30$ pc. Thus, we can adopt in our estimates $T = 10^4$ K over the entire range of r values, which yields $u \simeq 20$ km s^{-1}. Substituting u into (9), we obtain

$$n \simeq 4.2 \times 10^6 \mathcal{L}^{1/2} R_c^{3/2} \mathcal{N}, \qquad (11)$$

and the corresponding emission measure is

$$\mathrm{EM} \simeq 1.2 \times 10^{-6} \mathcal{L} R_c^2 \mathcal{N}^{4/3} \ \mathrm{cm}^{-6}\ \mathrm{pc}, \qquad (12)$$

which gives $u \simeq 0.65$ cm^{-3} and EM $\simeq 20$ cm^{-6} pc for the adopted parameters. Even allowing for the high temperature and the reduced recombination in the outer regions ($r \sim 30$ pc), the surface brightness in the H_α emission is fairly high and should be accessible to observations: $I_{H_\alpha} \gtrsim 8$ Rayleigh.

7. CONTRIBUTION OF GASEOUS CORONA OF THE GALAXY TO THE HEAT BALANCE

The DM clouds spend most of their time in the Galactic halo. Their ionized-gas envelopes are maintained by the background UV radiation, which has intensity $J_0 \simeq 10^6$ cm^{-2} s^{-1} ster^{-1} [18]. The mass-loss rate by an individual cloud due to the outflow of ionized gas is

$$\dot{M}_c = 4\pi m_p \sqrt{\frac{2J_0}{\alpha_r}} u_0 R_c^{3/2} \sim 10^{-13}\ M_\odot\ \mathrm{yr}^{-1}. \qquad (13)$$

The evaporating gas is slowed by viscous forces as it moves through the surrounding halo gas. The deceleration length is $l_d \delta R_c$ (Section 5), where the radius of the ionized atmosphere of the DM cloud is equal, to an order of magnitude, to its radius. With a mean gas density in the halo $n_h \sim 10^{-3}$ cm^{-3} and a density of ionized gas in the atmosphere $n_e \sim 10^3$ cm^{-3}, we obtain $l_d \sim 10^6 R_c \sim 10$ pc, which is much smaller than typical Galactic scales. Thus, the rate of heat inflow to the halo due to this source is of the order of $H_c \sim \dot{M}_c \mathcal{N} v_c^2/2 \sim 2.5 \times 10^{-25}$ erg cm^{-3} s^{-1}.

Upon integration over the halo height, the rate of heating is $\int H_c\,dz \sim 2.5\times10^{-3}$ erg cm^{-2} s^{-1} [here, $\mathcal{N} \sim f/\pi R_c^2 r_0$ (see Section 2), $R_c = 3\times10^{13}$ cm, and $r_0 = 10$ kpc]. Note that, for comparison, the total rate of energy input from type-II supernovae at a rate of 1/30 yr^{-1} is about $\sim 2\times10^{-4}$ erg cm^{-2} s^{-1}. The radiative-loss rate for interstellar gas with temperature $T \sim 10^6$ K and density $n \sim 10^{-3}$ cm^{-3} is, to an order of magnitude, $\Lambda(T)n^2 \sim 3\times10^{-29}$ erg cm^{-3} s^{-1}. Observations show that the halo gas has an extremely inhomogeneous distribution of density and temperature. In this case, we expect that the radiative-loss rates may be substantially higher than this estimate. In particular, in regions with densities $n \sim 10^{-2}$ cm^{-3} and temperatures $T \sim 10^5$ K, the radiative-loss rate is $\sim10^{-25}$ erg cm^{-3} s^{-1}. However, in any case, the inflow of energy from clumpuscules H_c substantially exceeds possible losses.

In this connection, we should mention the problem of maintaining the heat balance of the Galactic-halo gas, which is still far from understood. It is believed that collective supernova outbursts in OB associations can replenish radiative losses in the halo by forming extended chimneys connecting the disk and halo of the Galaxy. Detailed calculations show, however, that by no means every collective burst is capable of forming a chimney of this kind. In particular, Hensler *et al.* [39] showed that the hot remnant of a collective burst can reach a height $z \sim 1$–3 kpc only if ~100 supernovae are exploded at a height of 80 pc. Such events in the Galaxy are obviously very rare. Other recent results further exacerbate the problem. In their analysis of 21-cm, soft X-ray, gamma-ray, and radio continuum (408 MHz) sky surveys, Kalberla and Kerp [28] showed that the radial distribution of gas in the Galactic halo is characterized by a scale $R_h \sim 15$ kpc. At the same time, supernovae have a fundamentally different gas distribution: either an exponential radial distribution with a scale of about 4 kpc for type-I supernovae or a ring with radius ~5 kpc and width ~4 kpc for type-II supernovae. The idea that supernova explosions in the inner regions of the Galaxy eject hot gas into the halo, which then spreads in the radial direction, encounters difficulties because the characteristic time for spreading of the gas, $\sim10^8$ yr, is comparable to its radiative-cooling time, $(3$–$10)\times10^7$ yr. At the same time, this problem may have a simple solution if we take into consideration possible heating of the halo gas due to the conversion of the kinetic energy of ionized gas evaporating from DM clouds into heat. The power of this mechanism is comparable to that for supernova explosions and may even surpass the latter at $R > 10$ kpc if the total number or velocity of DM clouds in the Galaxy is smaller than the values adopted above: A tenfold reduced heating rate H_c is still comparable to the mean power of supernova explosions. (This may be important if further observations make it possible to significantly restrict parameters of clumpuscules, such as $\mathcal{N}$, M_c, and v_c.) Moreover, since the heating due to the dissipation of clumpuscule kinetic energy H_c exceeds the radiative-loss rate, it can maintain the heat balance in the halo gas on scales somewhat larger than r_0. For this reason, clumpuscules with a characteristic scale $r_0 \lesssim 10$ kpc are capable of maintaining the halo gas on radial scales $R_h \sim 15$ kpc (although the estimate $r_0 > 10$ kpc seems to be more realistic).

8. DISCUSSION AND CONCLUSION

The effects of mass loss by DM clouds during collisions or through evaporation brought about by external ionizing radiation are of interest not only from the viewpoint of possible observational manifestations of these effects, but also in connection with their influence on the dynamical and chemical evolution of the Galaxy. Here, we restrict our consideration to a qualitative discussion of this influence. A detailed analysis calls for a more specialized treatment. As was shown in Section 7, the rate of mass loss by an individual cloud due to the Galactic background UV radiation is $\dot{M}_c \sim 10^{-13}\,M_\odot$ yr^{-1}. Thus, if our estimate of the mass of a DM cloud ($\sim10^{-3}\,M_\odot$) is correct, the cloud will completely lose its mass during the lifetime of the Galaxy. Taking into account the fact that the clouds spend some time in the vicinity of hot OB stars, where the flux of ionizing UV photons exceeds the background radiation flux, and also the fact that, in the early stages of evolution, the background radiation might have been more intense than its present level, it seems likely that the lifetime of DM clouds is shorter than the age of the Galaxy. Note that the evaporation of clumpuscules is inefficient. This follows from the fact that the total amount of thermal energy absorbed by an individual cloud is $\sim 4\pi R_c k n_h T_h v_h t_H \sim 3\times10^{39}$ erg (where $n_h \sim 10^{-2}$ cm^{-3}, $T_h \sim 10^6$ K, and $v_h \sim 10^7$ cm s^{-1} are the density, temperature, and thermal velocity in the surrounding hot gas), whereas the binding energy in the molecular gas of clumpuscules is $\sim \varepsilon_b M_c/m_H \sim 3\times10^{42}$ erg, where $\varepsilon_b \sim 4$ eV is the binding energy of an individual molecule.

Assuming that the matter lost by clouds is captured in the inner regions of the Galaxy (at $R \lesssim 10$ kpc), it unavoidably follows that the total mass of visible matter in the Galaxy must have been larger than the mass currently contained in DM clouds. However, this is in sharp contrast with observations, since the surface density of the matter of DM clouds is $\Sigma \gtrsim 10^2\,M_\odot$ pc^{-2}, according to the estimate made in [18] on the basis of simulations of the lensing of quasar radio emission. This contradiction can be avoided by restricting the size of clouds R_c. Assuming, in accordance with [6, 18], that clumpuscules are gravitationally stable—i.e., $M_c \propto R_c$—and using (13), we obtain the time for the evaporation of an individual cloud by photoionizing radiation $t_{ev} \simeq 1.2\times10^{23}\,T_c R_c^{-1/2}$. Thus, clouds with radius $R_c < 1$–3.5×10^{12} cm can survive

over the Hubble time at T_c = 2.7–5 K. (Note that this limitation is weaker for higher temperatures, since $R_c \propto T_c^2$.) We should emphasize, however, that the matter lost by clouds (in particular, in collisions between clouds) can, in principle, settle in the outer regions of the Galaxy and form an extended ionized disk, as suggested in [40].

We can derive a lower limit to the cloud radius R_c taking into account their possible interaction with the Solar system. The rate of interaction of DM clouds with the Solar system is

$$\nu_S \sim \pi R_S^2 \mathcal{N} v_c,$$

where $\mathcal{N} \sim f/\pi R_c^2 r_0$ and $R_S \sim 40$ AU. This gives

$$R_c \sim \sqrt{\frac{f v_c}{\nu_S r_0}} R_S.$$

It seems reasonable to suggest that $\nu_S \leq (100\ \text{yr})^{-1}$: More frequent collisions would result in detectable perturbations of planetary orbits. In this case, for r_0 = 10 kpc, we obtain $R_c \geq 10^{11}$ cm. The total change of the surface density due to evaporating clumpuscules on time scales of order of the Hubble time is

$$\Delta\Sigma = \Sigma[(1 + 2t_H/t_{ev})^2 - 1],$$

where Σ is the current surface density of clumpuscules. Requiring $\Delta\Sigma < \Sigma_v$, where $\Sigma_v \sim 50\ M_\odot\ \text{pc}^{-2}$ is the surface density of stars, we find

$$\Sigma < \frac{\Sigma_v}{[(1 + 2t_H/t_{ev})^2 - 1]}.$$

For the lower limit $R_c = 10^{11}$ cm, this condition yields $\Sigma < \Sigma_v$. This estimate is inconsistent with the lower limit $\Sigma > 100\ M_\odot\ \text{pc}^{-2}$ obtained in [18]. The contradiction can be avoided if we assume that the covering factor f is half the value obtained in [16] based on measurements of variations in the radio fluxes of quasars. Note, in this connection, that the conservative estimate made in [18] gives $f \sim 10^{-4}$. We should stress that, since $2t_H/t_{ev} < 1$ and $t_{ev} \propto R_c^{-1/2}$, the upper bound obtained depends only slightly on other parameters—approximately as $(f\nu_S r_0/v_c)^{1/4}$, although it is sensitive (inversely proportional) to the fraction of the evaporated matter captured by the Galaxy. The cloud velocity perpendicular to the line of sight must be decreased ($v_{c\perp} \propto \propto R_c$) in order to leave the duration of extreme scattering events unchanged. In turn, this means that DM clouds must have very elongated orbits, so that the radial component of the velocity ($\leq$500 km s^{-1}) substantially exceeds the tangential component.

Under these constraints, the rate of mass inflow due to cloud collisions varies as $\nu_G M_c \propto f^2 R_c^{-1}$ and can be as high as 2 and 20 $M_\odot$ yr^{-1} for r_0 = 1 and 10 kpc, respectively, which would lead to a mass overproduction during the lifetime of the Galaxy. However, in view of the strong dependence on f, this quantity can be decreased to < (0.4–4) $M_\odot$ yr^{-1} for $f < 10^{-3}$.

Although the origin of DM clouds is currently far from fully understood, it is likely that they arose during prestellar stages in the evolution of the Universe and are thus among the oldest Galactic objects [13]. In this case, these clouds should be composed of matter with primordial chemical composition, so that they can decrease the metallicity of the interstellar gas—i.e., the content of heavy elements in the gas—when they mix with it. In other words, models for the chemical evolution of the Galaxy that include mass exchange with DM clouds should predict, all other conditions being the same, a slower enrichment in heavy elements than models without clouds. In particular, it follows that, since the rate of cloud collisions per unit volume given by (2) increases toward the Galactic center, the corresponding mass loss should have markedly weakened the observed radial metallicity gradient for stars and the interstellar gas, or even inverted it, unless the characteristic scale r_0 of distribution (1) exceeds 10–15 kpc. Otherwise, the star-formation rate must increase toward the center, to compensate for the inflow of gas with primordial composition.

The problems discussed in this work can be summarized as follows:

(1) Collisions of dense gaseous condensations—possible carriers of Galactic dark matter, which manifest themselves in extreme scattering events—occur rather frequently: Depending on the total number of such clouds, there may be from 10^3 to 10^4 collisions per year in the Galaxy.

(2) The gas contained in these condensations is heated after collisions, then disperses and mixes with the interstellar gas. The rate of matter inflow into the interstellar medium from collisions can reach 1–10 $M_\odot$ yr^{-1}. In this case, the effect of such condensations on the dynamical and chemical evolution of the Galaxy could be significant. In particular, it could reduce the metallicity gradients for stars and the interstellar gas.

(3) At some stages of expansion, after collisions between condensations, the hot gas becomes a source of optical radiation with characteristics close to those of the radiation of massive O stars. The duration of these stages is about 10 days.

(4) At later stages, expanding fragments of the condensations could be detectable in the 21-cm line. The duration of these stages is about 1 million years, and the total mass contained in the fragments is $\sim 3 \times (10^5$–$10^6)\ M_\odot$. This H I gas has a higher velocity dispersion than the interstellar hydrogen.

(5) Clouds surrounding hot stars outside their H II zones are subject to the action of more intense ionizing radiation. As a result of the outflow of ionized gas from the envelopes of the clouds, this gives rise to the formation of zones of rather high density (with $n_e \sim 0.65$ cm^{-3}) around such stars, which may be observable in recom-

bination H_α emission with emission measure EM ~ 20 cm^{-6} pc^{-1}, even if these stars are far from the disk, where the density of the interstellar gas is low.

(6) The outflow of ionized gas from the envelopes of clouds may be a substantial source of mass for the interstellar gas: The total mass loss from all the clouds could reach (2–20) $M_\odot$ yr^{-1}. If a large fraction of this matter is captured by the Galaxy, the requirement that the total inflow during the evolution of the Galaxy not exceed the total mass of stars leads to a constraint on the radius of the clouds, $R_c \le 3.5 \times 10^{12}$ cm, and also suggests that the cloud orbits are very elongated. In this case, the upper limit to the surface density of DM clouds is 50 $M_\odot$ pc^{-2}.

(7) The material lost by gas DM clouds generally gas high velocities relative to the interstellar gas ($\le$500 km s^{-1} [18]). The subsequent deceleration and mixing of the lost matter with the interstellar gas is accompanied by the conversion of its kinetic energy into heat, which could serve as a fairly powerful source of heating. This could explain the large radial scale of the Galactic-halo gas (~15 kpc), provided the scale (1) of the cloud distribution is sufficiently large ($\gtrsim$10 kpc).

The discovery (or, conversely, failure to detect at a given level) of optical radiation, H_α emission, and 21-cm radio emission from clouds of dark matter or their fragments would enable more accurate estimation of the cloud parameters, in particular, their contribution to the total mass of the Galaxy (if they are not detected, this can place limits on such parameters). In principle, the dense atomic clouds proposed by Field and Corbelli [11] as dark-matter candidates could also be detectable in H_α and 21-cm emission as a result of collisions and ionization by the background radiation. However, their parameters (size, density, velocity dispersion) are uncertain, and this prevents us from drawing definite conclusions. It is assumed in [7, 8, 12, 14, 41] that baryonic dark matter forms structures similar to globular clusters—clusters of dark baryonic matter with some fraction of baryons in the form of gaseous clouds (see the more detailed discussion in [12, 14]). The stability of such configurations suggests that the gas clouds in them are collisionless; however, even rare collisions can provide a significant inflow of mass to the interstellar medium if the clouds are numerous. Moreover, the impact of the background ionizing UV radiation could also be important, although the influence of the neighboring stars (brown dwarfs) could be more significant [14].

ACKNOWLEDGMENTS

I would like to thank P.M.W. Kalberla, who attracted my attention to the problem of extreme scattering events and to the paper by Walker and Wardle [18]. I am also grateful to D. Bomans, E. Corbelli, R.-J. Dettmar, R. Schlickeiser, A. Schröer, and C. Taylor for useful discussions and to B.M. Shustov for valuable remarks. I am also grateful to Ph. Jetzer for comments on global clusters of dark matter. This work was supported by the State Research Program "Astronomy" and the Center "Ground-based Astronomy" in the framework of the Federal program "Integration" (projects nos. 352 and 353). I also wish to thank the Osservatorio Astrofisico di Aecetri, where this work was completed, for its hospitality.

Note to the Proofs. Recently, Kalberla *et al.* [Astron. Astrophys. **350**, L9 (1999)] have shown that the residual diffuse background of gamma-ray radiation can be best explained if dark matter is contained in clumpuscules with the parameters discussed here. Their contribution to the surface density is estimated to be 140. Jaking this into account, the lower limit on the gas temperature can be about 10 K.

REFERENCES

1. C. Alcock, C. W. Akerlof, R. A. Allsman, *et al.*, Nature **365**, 621 (1993).
2. E. Auborg, P. Bazeyre, S. Brehin, *et al.*, Nature **365**, 623 (1993).
3. C. Alcock, R. A. Allsman, D. Alves, *et al.*, Astrophys. J. **486**, 697 (1997).
4. B. V. Komberg, D. A. Kompaneets, and V. N. Lukash, Astron. Zh. **72**, 457 (1995).
5. D. Pfenniger, F. Combes, and L. Martinet, Astron. Astrophys. **285**, 79 (1994).
6. D. Pfenniger and F. Combes, Astron. Astrophys. **285**, 94 (1994).
7. F. De Paolis, G. Ingrosso, Ph. Jetzer, *et al.*, Astron. Astrophys. **295**, 567 (1995).
8. F. De Paolis, G. Ingrosso, Ph. Jetzer, *et al.*, Astron. Astrophys. **299**, 647 (1995).
9. R. N. Henriksen and L. M. Widrow, Astrophys. J. **441**, 70 (1995).
10. F. De Paolis, G. Ingrosso, Ph. Jetzer, *et al.*, *Dark Matter in Galaxies*, ASP Conf. Ser. **117**, 266 (1997).
11. G. B. Field and E. Corbelli, Dark Matter in Galaxies, ASP Conf. Ser. **117**, 258 (1997).
12. O. Gerhard and J. Silk, Astrophys. J. **472**, 34 (1996).
13. D. Pfenniger and F. Combes, astro-ph/9801319 (1998).
14. F. De Paolis, G. Ingrosso, Ph. Jetzer, *et al.*, Astrophys. J., 1999 (in press) astro-ph/9801126.
15. D. D. Dixon, D. H. Hartmann, E. D. Kolaczyk, *et al.*, New Astronomy **3**, 539, astro-ph/9803237 (1998).
16. R. L. Fiedler, B. Dennison, K. J. Johnston, *et al.*, Nature **326**, 675 (1987).
17. R. Romani, R. D. Blandford, and J. M. Cordes, Nature **328**, 324 (1987).
18. M. Walker and M. Wardle, Astrophys. J. Lett. **498**, L125 (1998).
19. B. T. Draine, Astrophys. J. Lett. **509**, L41 (1998).
20. J. Binney and S. Tremain, *Galactic Dynamics* (Princeton Univ., Princeton, 1987).
21. M. E. Stone, Astrophys. J. **159**, 277 (1970).
22. M. A. Hausmann, Astrophys. J. **245**, 72 (1981).
23. D. L. Gilden, Astrophys. J. **279**, 335 (1984).

24. J. C. Lattanzio, J. J. Monagham, H. Pongracic, *et al.*, Mon. Not. R. Astron. Soc. **215**, 125 (1985).
25. R. I. Klein, C. F. McKee, and D. T. Woods, *The Physics of Interstellar and Intergalactic Medium*, ASP Conf. Ser. **80**, 366 (1995).
26. F. Miniati, T. W. Jones, A. Ferrara, *et al.*, Astrophys. J. **491**, 216 (1997).
27. Ya. B. Zeldovich and Yu. P. Zaĭzer, *Physics of Shock Waves and High-Temperature Gas-Dynamical Phenomena* [in Russian] (Nauka, Moscow, 1966).
28. P. M. W. Kalberla and J. Kerp, Astron. Astrophys. **339**, 745 (1998).
29. S. A. Kaplan and S. B. Pikel'ner, *Physics of the Interstellar Medium* [in Russian] (Nauka, Moscow, 1979).
30. M. G. Wolfire, D. Hollenbach, C. F. McKee, *et al.*, Astrophys. J. **443**, 152 (1995).
31. R. I. Klein, C. F. McKee, and P. Collela, Astrophys. J. **420**, 213 (1994).
32. Yu. A. Shchekinov, Astron. Astrophys. **314**, 927 (1996).
33. C. Heiles, Astrophys. J. **481**, 193 (1997).
34. M. Walker and M. Wardle, ASP Conf. Ser. **166**, 269 (1999).
35. J. E. Dyson, Astrophys. Space Sci. **1**, 388 (1968).
36. J. B. Dove and J. M. Shull, Astrophys. J. **430**, 222 (1994).
37. V. P. Kutyrev and R. J. Reynolds, Astrophys. J. Lett. **344**, L9 (1989).
38. L. Spitzer, *Physical Processes in the Interstellar Medium* (Wiley, New York, 1978; Mir, Moscow, 1981).
39. G. Hensler, M. Samland, O. Michaelis, *et al.*, *The Physics of Galactic Halos* (Akademie, Berlin, 1996), 225.
40. E. E. Salpeter, *The Physics of Interstellar and Intergalactic Medium*, ASP Conf. Ser. **80**, 264.
41. I. Wasserman and E. E. Salpeter, Astrophys. J. **433**, 670 (1994).

Translated by A. Kozlenkov

Astronomy Reports, Vol. 44, No. 2, 2000, pp. 76–88. Translated from Astronomicheskiĭ Zhurnal, Vol. 77, No. 2, 2000, pp. 96–108.

Analysis of Elemental Abundances in the Atmospheres of Three Hyades Red Giants

A. A. Boyarchuk[1], L. I. Antipova[1], M. E. Boyarchuk[1], and I. S. Savanov[2]

[1]*Institute of Astronomy, Russian Academy of Sciences, Pyatnitskaya ul. 48, Moscow, 109017 Russia*

[2]*Astrophysical Observatory, pos. Nauchnyĭ, Crimea, Ukraine*

Received February 25, 1999

Abstract—Model atmospheres are fitted to spectroscopic data in order to analyze the elemental abundances in the atmospheres of three red giants in the Hyades cluster. The three stars have almost identical chemical compositions, with iron-group elements slightly overabundant compared to the solar values—a pattern that is typical of Hyades dwarfs. The overabundances of the light elements Na, Al, and Si are virtually equal to those observed for field giants. No enrichment in rare-earth elements relative to iron was found, in sharp contrast to field giants. It is concluded that these discrepancies are due to the age difference between the two groups of stars, which have resulted in different degrees of convective overshooting. © *2000 MAIK "Nauka/Interperiodica".*

The Hyades, which is the star cluster nearest to the Sun, has long been a focus of attention for researchers. The distance to the Hyades is used to establish the scale of the Universe, and much research has been centered on refining this crucial parameter. New stellar parallaxes measured using the *Hipparcos* satellite have enabled a very accurate determination of the distance modulus of the cluster: $m - M = 3.33 \pm 0.01^m$ [1]. Furthermore, the Hyades is among the youngest open clusters and is of considerable interest for studies of the chemical evolution of the Galaxy, including analyses of the age–metallicity relation and estimates of the mixing time in the Galactic disk [2–4]. Numerous studies have suggested that the metal abundances in Hyades stars exceed the solar values. For example, from their analysis of 14 F dwarfs, Boesgaard and Friel [4] determined very accurately the mean metallicity of the cluster to be [Fe/H] = +0.127 ± 0.022, in good agreement with earlier determinations. Comparison of the metal abundance of the Hyades with those of other clusters led these authors to conclude that cluster metallicities are determined more by their position in the Galaxy and the chemical composition of the local gas out of which each cluster forms than by the cluster's age. A young cluster with higher-than-average metallicity located in the vicinity of the Sun, and therefore containing fairly bright stars, is of obvious interest for analyses of stellar-abundance anomalies associated with the evolutionary stage of the stars studied.

For this reason, we included three of the four bright red giants in the Hyades cluster in our program of analyses of elemental abundances in the atmospheres of red giants. (We excluded the fourth giant from our program because it is a spectroscopic binary.) Several researchers have already performed similar studies of these stars [5–7]; however, their analyses were based on photographic data. In contrast, our work is based on CCD observations. In addition, we felt that it was of interest to analyze the elemental abundances in the Hyades red giants using the same technique we had used earlier for field stars (described, for example, in [10, 11]), and thereby to compare the chemical compositions of Hyades and field stars determined by applying the same technique to homogeneous data.

Our observations were obtained in 1994–1997 on the 2.6-m telescope of the Crimean Astrophysical observatory of the Ukrainian Ministry for Science and Technology. We used a CCD detector mounted in the first chamber of the Coudé focus. The dispersion was 3 Å/mm and the signal-to-noise ratios were 100–300. Each frame recorded a 30 or 60 Å spectral interval, depending on the type of CCD used. We selected the 20 spectral bands so as to ensure a sufficient number of lines for our analysis. We reduced the observational data using the software package developed for this purpose at the Crimean Astrophysical Observatory.

We particularly paid attention to definition of the continuum level, since this is often the main factor determining the accuracy of results for red giants. We selected unblended lines with well-determined oscillator strengths for further analysis. We used the EW program developed at the Crimean Astrophysical Observatory to determine the equivalent widths of the spectral lines [8]. This program fits a Gaussian curve to the line profile and constructs the calibration curve relating the residual line intensity and equivalent width. We used this relation to estimate the equivalent widths of spectral lines with blended wings that could not be determined by fitting Gaussian profiles. In these cases, we selected only lines that were not blended at their cen-

1063-7729/00/4402-0076$20.00 © 2000 MAIK "Nauka/Interperiodica"

ters. The spectral-line data (including equivalent widths) used to determine the elemental abundances are summarized in Table 1.

We analyzed the chemical compositions of the program stars using model atmospheres based on the grid of [9] and used the Width9 program to determine the elemental abundances. We estimated the stellar atmosphere parameters as follows.

We determined the microturbulent velocity V_t from the profiles of FeI lines, which are most numerous in the spectra of red giants. To this end, we selected from [9] a model atmosphere with $T_{\rm eff}$ and $\log g$ as close as possible to the expected values (based on the spectral type of the star studied), then computed FeI abundances assuming various V_t. We chose the V_t value that yielded FeI abundances that did not depend on the equivalent width and used it in the subsequent analysis. After determining the final $T_{\rm eff}$ and $\log g$ values, we checked our estimate of V_t in an analogous way and, when necessary, repeated the analysis with a refined value for V_t.

We determined the effective temperatures $T_{\rm eff}$ and surface gravities $\log g$ of the program stars using lines of neutral elements and of ions with various excitation and ionization potentials. Our analysis is based on the following effect. It is well known from the theory of stellar evolution that iron-peak elements are synthesized only in supernova explosions and cannot be produced during the main-sequence or giant stages. This implies that the relative abundances of these elements in the atmospheres of giants should be the same as in the gas from which the stars formed. Furthermore, since the Hyades is rather close to the Sun, we do not expect significant differences in the relative abundances of iron-group elements for the solar atmosphere and the atmospheres of Hyades stars. In other words, $\log\varepsilon(E)_* - \log\varepsilon(E)_0$ should be the same for all iron-group elements E:

$$[X] = \log\varepsilon(E)_* - \log\varepsilon(E)_0 = M = \text{const}.$$

Here, $\varepsilon(E)_*$ and $\varepsilon(E)_0$ are the abundances of the corresponding element in the star and Sun, respectively, and M characterizes the metallicity of the star; i.e., the difference between the iron-group element abundances in its atmosphere and the corresponding values for the solar atmosphere. Of course, in practice, M is not the same for all elements, and the scatter could be due not only to the accuracy of the equivalent widths and adopted oscillator strengths, but also to the correctness of our choice of stellar parameters.

Guided by these considerations, we used the selected iron-group lines to calculate for each program star the elemental abundances corresponding to various sets of stellar-atmosphere parameters near the expected values. We then analyzed the results to identify those parameters that resulted in the smallest scatter of the relative abundances for the iron-group elements. See [10, 11] for a more detailed description of this technique.

As an example, Fig. 1 illustrates some results of our calculations for the giant γ Tau (we constructed similar plots for all our program stars). We performed our computations for $\log g = 2.83$, which was indicated by our analysis for this star, and various effective temperatures. It is evident from the figure that the abundance curves for different elements—both neutral atoms and ions—intersect at essentially a single point corresponding to $T_{\rm eff} = 4956$ K. This means that the model with this temperature exhibits the minimum scatter in the relative abundances of different chemical elements, both neutral atoms and ions. We, therefore, adopted $T_{\rm eff} = 4956$ K as our final effective-temperature estimate for γ Tau. The small scatter for this temperature suggests that our relative abundances for the iron-group elements are correct. If the relative abundance of some element (e.g., with respect to iron) differed from the solar value, the line in Fig. 1 corresponding to this element would pass above or below the common intersection point.

Figure 2 shows FeI abundances in γ Tau derived using spectral lines with various excitation potentials using a model atmosphere with $T_{\rm eff} = 4956$ K and $\log g = 2.83$. It is evident that the calculated abundances remain constant, on average, throughout the range of excitation potentials; i.e., our temperature estimate describes the excitation of different atoms well.

We have thus shown in [10, 11] and in the current paper that the adopted grid of model atmospheres contains a solution that best describes the observed line spectrum—the inferred abundances of iron-group elements have the least scatter; the abundances inferred from the lines of neutral elements agree with those derived from ion lines, and the results exhibit no trend with excitation potential. It is the parameters of this best-fit model atmosphere that we adopted in our subsequent analysis.

Note that the atmosphere parameters determined in this way, from an analysis of stellar spectra, can differ from those given by other, nonspectroscopic methods. For example, the discrepancies for the Sun are $\Delta(T_{\rm eff}) = 150$ K and $\Delta(\log g) = 0.15$ [12]. Systematic discrepancies have also been found for red giants [10, 11]. Note that the atmosphere parameters derived from spectroscopic analyses are formal parameters, since they merely enable selection of a most suitable model atmosphere. We have already shown [12] that, if a model-atmosphere analysis uses the Sun as a "reference" star, the solar elemental abundances should be derived using the same model-atmosphere grid, since the spectroscopic atmosphere parameters and resulting metallicities can differ slightly from one grid to another [12]. Fortunately, we also showed in [12] (see Figs. 6 and 7 in that paper) that the relative abundances (e.g., Na/Fe) determined using this approach are grid-independent, a

Table 1. Line equivalent widths and elemental abundances for Hyades giants

		γ Tau		δ^1 Tau		ε Tau		Sun	
Sp =		K0IIIabCN1		K0IIICN0.5		G9.5IIICN0.5			
T (K) =		4956		4880		4880		5887	
log$g$ =		2.83		2.84		2.50		4.57	
v_t (km/s) =		1.35		1.25		1.46		0.80	
Line	E. P., eV	loggf	W_λ, mÅ	log(N/H)	W_λ, mÅ	log(N/H)	W_λ, mÅ	log(N/H)	log(N/H)
1	2	3	4	5	6	7	8	9	10
NaI									
6160.75	2.10	–1.21	122.1	–5.24	120.0	–5.21	125.0	–5.26	–5.70
6154.22	2.10	–1.51	96.1	–5.34	101.8	–5.21	112.0	–5.16	–5.75
MgI									
8717.83	5.93	–0.86	111.8	–4.22	116.5	–4.15	–	–	–4.51
8712.70	5.93	–1.16	84.5	–4.25	–	–	–	–	–4.49
6319.24	5.11	–2.22	65.1	–4.18	64.5	–4.17	–	–	–4.50
6318.71	5.11	–1.94	78.4	–4.27	–	–	–	–	–4.49
AlI									
6698.67	3.13	–1.86	57.4	–5.36	56.90	–5.34	64.00	–5.29	–5.59
6696.03	3.13	–1.55	80.0	–5.32	81.30	–5.26	88.30	–5.24	–5.55
SiI									
6790.68	6.08	–1.97	–	–	14.2	–4.25	–	–	(–4.52)
6414.99	5.87	–1.10	–	–	70.1	–4.19	68.90	–4.25	–4.52
6155.20	5.62	–0.80	96.6	–4.31	–	–	–	–	–4.65
6145.08	5.59	–1.41	58.7	–4.34	66.5	–4.20	–	–	–4.54
6142.53	5.59	–1.49	50.3	–4.41	55.8	–4.30	53.00	–4.41	–4.50
6131.86	5.59	–1.68	45.6	–4.30	46.8	–4.27	48.00	–4.30	–4.58
6131.54	5.59	–1.75	48.1	–4.18	49.4	–4.15	–	–	–4.51
6125.03	5.59	–1.57	53.4	–4.27	53.6	–4.26	56.00	–4.27	–4.48
6106.62	5.61	–2.15	22.1	–4.30	24.7	–4.23	–	–	–4.49
5793.05	4.93	–1.89	73.0	–4.31	–	–	–	–	–4.51
5772.25	5.06	–1.70	72.9	–4.36	83.8	–4.15	82.00	–4.28	–4.43
5701.12	4.93	–1.96	62.6	–4.42	69.5	–4.28	–	–	–4.51
5690.43	4.93	–1.73	–	–	74.4	–4.42	–	–	–4.50
5684.47	4.95	–1.57	80.0	–4.49	86.3	–4.34	–	–	–4.51
5517.55	5.08	–2.40	31.4	–4.39	33.7	–4.34	–	–	–4.52
CaI									
6798.51	2.70	–2.56	31.3	–5.37	27.5	–5.43	–	–	(–5.46)
6455.60	2.52	–1.34	106.2	–5.45	107.9	–5.35	–	–	–5.66
6166.44	2.51	–1.15	112.5	–5.51	–	–	–	–	–5.71
6156.10	2.51	–2.46	–	–	39.0	–5.48	39.0	–5.58	–5.82
5867.57	2.92	–1.59	59.0	–5.55	59.0	–5.51	54.0	–5.70	–5.67
5260.39	2.52	–1.74	67.3	–5.67	72.5	–5.52	77.4	–5.57	–5.65
ScII									
6604.59	1.36	–1.11	82.5	–8.81	86.2	–8.71	–	–	–8.90
6320.84	1.50	–1.83	38.2	–8.74	36.4	–8.76	–	–	–8.93
6300.68	1.51	–1.97	29.1	–8.78	28.3	–8.79	–	–	–8.92
5684.19	1.51	–0.91	78.8	–8.84	83.7	–8.70	–	–	–8.90
5552.22	1.45	–2.10	22.8	–8.84	–	–	–	–	–9.00
5357.20	1.50	–2.15	21.0	–8.78	23.3	–8.71	–	–	–9.02
5334.22	1.49	–2.10	24.0	–8.76	22.0	–8.81	–	–	–8.95
5318.34	1.35	–1.69	45.5	–8.87	–	–	–	–	–8.96
5239.84	1.45	–0.69	91.0	–8.83	98.9	–8.59	–	–	–8.88
TiI									
8682.98	1.05	–1.84	76.6	–6.88	–	–	–	–	–7.06
8675.38	1.07	–1.58	92.0	–6.89	–	–	–	–	–7.04
6599.11	0.90	–1.99	57.0	–7.03	79.9	–6.57	–	–	–7.03
6497.68	1.44	–1.93	–	–	34.1	–6.78	–	–	(–7.01)
6325.15	0.02	–3.57	30.3	–6.94	28.4	–6.93	–	–	–6.99
6312.24	1.46	–1.52	49.7	–6.93	46.7	–6.93	–	–	–7.06
6303.77	1.44	–1.50	54.3	–6.89	52.7	–6.87	–	–	–7.10

Table 1. (Contd.)

1	2	3	4	5	6	7	8	9	10
6149.74	2.15	–1.26	–	–	–	–	20.0	–7.04	–7.04
6146.22	1.87	–1.52	27.8	–6.83	–	–	–	–	–7.05
6126.22	1.06	–1.34	–	–	81.7	–6.93	91.0	–7.01	–7.10
6121.01	1.87	–1.34	30.0	–6.97	25.8	–7.02	36.0	–6.94	–6.99
6098.66	3.06	–0.10	–	–	31.2	–6.78	–	–	–7.10
6092.80	1.89	–1.36	30.5	–6.91	30.8	–6.87	–	–	–7.05
6091.18	2.27	–0.38	58.6	–6.95	62.8	–6.81	–	–	–7.07
6064.63	1.05	–1.82	56.4	–6.98	59.6	–6.87	–	–	–7.08
6031.68	0.05	–3.92	17.9	–6.82	–	–	–	–	(–7.01)
5941.75	1.05	–1.51	–	–	86.2	–6.65	–	–	–7.07
5937.80	1.07	–1.85	–	–	64.2	–6.72	–	–	–7.09
5880.27	1.05	–1.94	56.2	–6.85	–	–	–	–	–7.09
5866.45	1.06	–0.80	113.2	–6.91	–	–	–	–	–7.00
5774.03	3.30	0.45	–	–	42.7	–6.82	–	–	–7.08
5766.33	3.28	0.36	30.6	–7.02	–	–	–	–	(–7.01)
5716.45	2.30	–0.78	32.8	–6.95	31.3	–6.94	–	–	–7.04
5713.88	2.29	–0.93	–	–	25.8	–6.93	–	–	–7.08
5702.64	2.29	–0.65	41.6	–6.92	45.6	–6.81	–	–	–7.10
5689.46	2.30	–0.40	53.0	–6.96	52.4	–6.92	–	–	–7.08
5679.92	2.47	–0.63	–	–	28.1	–6.97	–	–	–7.11
5673.41	3.11	–0.36	–	–	11.0	–7.02	–	–	–7.01
5449.16	1.44	–2.00	23.9	–6.89	–	–	–	–	–6.84
5438.29	1.43	–1.87	–	–	19.1	–7.12	–	–	–7.08
5426.24	0.02	–2.87	52.8	–7.16	52.4	–7.11	–	–	–7.06
5384.63	0.83	–2.78	–	–	14.1	–7.07	–	–	(–7.01)
5366.65	0.81	–2.54	35.7	–6.84	35.8	–6.79	–	–	–7.00
5351.07	2.77	–0.07	42.0	–6.92	42.8	–6.87	–	–	–7.04
5313.25	1.06	–2.25	22.3	–7.11	25.6	–7.00	–	–	–7.05
5295.78	1.06	–1.65	60.3	–7.00	56.9	–7.00	70.0	–6.96	–6.99
5282.40	1.05	–1.53	–	–	65.5	–6.97	–	–	–6.71
5251.49	0.82	–2.49	26.5	–7.05	30.4	–6.93	40.4	–6.90	–6.97
5223.63	2.09	–0.53	56.2	–6.98	53.4	–6.98	64.3	–6.94	–7.08
5219.70	0.02	–2.19	–	–	88.5	–7.06	–	–	–7.07
5147.48	0.00	–1.96	107.2	–6.99	109.8	–6.80	124.8	–6.83	–6.96
5145.47	1.46	–0.45	–	–	91.1	–6.99	96.0	–7.13	–7.08
5113.43	1.44	–0.80	75.0	–7.08	–	–	–	–	–7.08
VI									
6504.16	1.18	–0.74	–	–	60.3	–7.82	–	–	(–8.04)
6292.82	0.29	–1.47	75.1	–7.97	78.3	–7.83	–	–	–8.04
6285.16	0.28	–1.56	68.0	–8.00	69.6	–7.91	–	–	–8.06
6224.50	0.29	–1.82	61.7	–7.83	60.4	–7.79	–	–	–8.06
6216.35	0.28	–0.88	113.8	–7.85	113.1	–7.74	–	–	–8.06
6150.13	0.30	–1.51	–	–	77.0	–7.78	87.0	–7.87	–8.03
6135.36	1.05	–0.76	–	–	69.3	–7.76	–	–	–8.04
6119.50	1.06	–0.44	–	–	–	–	93.0	–7.88	–8.04
6111.62	1.04	–0.71	71.6	–7.85	67.8	–7.85	75.0	–7.94	–8.05
6090.21	1.08	–0.13	96.8	–7.90	95.2	–7.83	–	–	–8.04
6081.44	1.05	–0.63	75.8	–7.84	77.4	–7.73	–	–	–8.04
6058.18	1.04	–1.39	33.4	–7.83	32.1	–7.81	–	–	–7.98
6039.69	1.06	–0.64	67.8	–7.96	–	–	69.0	–8.07	–8.06
5830.68	3.11	0.69	18.3	–7.85	–	–	–	–	–8.07
5776.67	1.08	–1.49	18.8	–7.99	–	–	20.0	–8.06	–8.01
5670.85	1.08	–0.39	75.8	–7.99	–	–	–	–	–8.02
5668.37	1.08	–0.96	–	–	47.6	–7.87	–	–	–8.03
5507.77	2.36	–0.17	–	–	11.0	–8.06	–	–	–8.09
5240.88	2.37	0.33	24.8	–8.13	29.3	–7.99	34.4	–8.01	–8.06

Table 1. (Contd.)

1	2	3	4	5	6	7	8	9	10
CrI									
6680.14	4.16	–0.40	26.4	–6.19	–	–	–	–	–6.35
6630.02	1.03	–3.48	57.0	–6.17	60.4	–6.05	62.0	–6.23	–6.38
6501.21	0.98	–3.61	–	–	40.9	–6.31	–	–	(–6.36)
6330.09	0.94	–2.83	–	–	86.2	–6.31	–	–	–6.37
5982.85	3.17	–1.67	17.4	–6.24	–	–	–	–	(–6.36)
5843.24	3.00	–2.03	14.0	–6.17	–	–	–	–	–6.40
5788.39	3.00	–1.60	38.9	–6.00	32.0	–6.10	–	–	–6.41
5787.99	3.31	–0.09	83.6	–6.31	78.6	–6.35	86.0	–6.37	–6.34
5783.11	3.31	–0.34	71.2	–6.30	74.8	–6.18	75.0	–6.33	–6.33
5738.55	3.54	–1.35	11.5	–6.34	–	–	–	–	–6.39
5719.82	3.01	–1.66	26.0	–6.19	27.0	–6.14	–	–	–6.34
5694.74	3.86	–0.20	–	–	53.9	–6.11	–	–	–6.38
5348.32	1.00	–1.20	157.0	–6.41	–	–	–	–	–6.33
5344.76	3.43	–0.98	–	–	30.4	–6.25	35.0	–6.25	–6.39
5329.12	2.91	–0.01	115.1	–6.16	107.6	–6.22	–	–	–6.32
5318.78	3.43	–0.68	46.6	–6.26	42.7	–6.30	49.0	–6.29	–6.37
5312.88	3.43	–0.54	51.1	–6.32	55.3	–6.20	60.0	–6.23	–6.39
5304.21	3.45	–0.63	41.2	–6.39	44.6	–6.29	51.0	–6.28	–6.37
5300.75	0.98	–2.07	120.7	–6.20	–	–	–	–	–6.28
5296.69	0.98	–1.39	147.6	–6.37	–	–	–	–	–6.27
5287.18	3.44	–0.87	37.2	–6.24	42.3	–6.10	41.5	–6.22	–6.38
5272.00	3.45	–0.47	63.8	–6.12	64.6	–6.05	–	–	–6.38
5247.56	0.96	–1.65	139.2	–6.27	–	–	–	–	–6.26
5243.35	3.39	–0.59	–	–	43.2	–6.42	–	–	–6.37
5241.46	2.71	–2.05	18.9	–6.29	18.8	–6.27	23.7	–6.24	–6.44
5238.97	2.71	–1.34	49.2	–6.36	49.7	–6.31	56.4	–6.32	–6.38
5214.62	3.32	–0.68	–	–	–	–	61.8	–6.18	–6.43
5122.12	1.03	–3.14	63.0	–6.25	60.6	–6.23	71.0	–6.25	–6.38
CrII									
5508.62	4.15	–2.01	–	–	37.5	–6.11	–	–	–6.36
5502.09	4.17	–1.89	–	–	37.4	–6.22	–	–	–6.34
5334.88	4.07	–1.62	54.0	–6.21	53.3	–6.21	–	–	–6.31
5313.59	4.06	–1.61	52.8	–6.26	58.8	–6.10	–	–	–6.35
5310.70	4.05	–2.18	26.7	–6.34	31.2	–6.22	–	–	–6.34
5308.44	4.05	–1.79	49.8	–6.16	53.6	–6.05	–	–	–6.37
5305.85	3.81	–2.00	44.6	–6.33	50.1	–6.19	50.0	–6.33	–6.38
5237.32	4.07	–1.12	71.6	–6.31	75.0	–6.18	–	–	–6.27
MnI									
6440.93	3.77	–1.28	–	–	26.1	–6.41	25.5	–6.51	–6.61
5551.97	5.49	0.50	–	–	17.5	–6.50	–	–	–6.60
5413.68	3.86	–0.55	–	–	64.7	–6.19	–	–	–6.54
5399.48	3.85	–0.21	–	–	79.1	–6.23	–	–	–6.43
5377.61	3.84	–0.09	–	–	–	–	–	–	–6.44
5344.45	5.38	0.47	–	–	25.5	–6.36	–	–	–6.61
5260.77	3.12	–1.55	–	–	35.0	–6.61	–	–	–6.62
FeI									
6810.27	4.61	–0.92	86.0	–4.40	–	–	–	–	–4.51
6806.86	2.73	–3.05	92.7	–4.33	–	–	–	–	–4.56
6793.27	4.12	–2.34	48.6	–4.24	47.6	–4.22	–	–	–4.52
6786.88	4.17	–1.87	59.6	–4.45	59.4	–4.40	65.0	–4.44	–4.53
6783.71	2.58	–3.83	–	–	61.1	–4.26	–	–	–4.38
6783.27	2.55	–4.54	–	–	24.5	–4.29	31.0	–4.28	–4.65
6752.72	4.62	–1.17	69.4	–4.44	–	–	–	–	–4.54
6739.54	1.55	–4.82	55.1	–4.64	–	–	–	–	–4.55
6726.67	4.59	–0.98	81.2	–4.44	–	–	–	–	–4.51
6713.76	4.77	–1.39	44.7	–4.52	–	–	–	–	–4.53
6710.31	1.48	–4.77	84.8	–4.25	86.6	–4.15	–	–	–4.59

Table 1. (Contd.)

1	2	3	4	5	6	7	8	9	10
6704.48	4.20	–2.55	26.0	–4.39	33.2	–4.21	27.0	–4.43	–4.56
6703.57	2.75	–2.95	94.7	–4.36	98.4	–4.19	97.0	–4.46	–4.52
6699.14	4.57	–2.07	26.7	–4.44	29.3	–4.35	33.0	–4.36	–4.57
6653.88	4.14	–2.42	42.5	–4.24	40.4	–4.25	43.0	–4.31	–4.56
6646.98	2.60	–3.86	59.2	–4.28	57.9	–4.26	62.0	–4.36	–4.53
6633.76	4.54	–0.66	–	–	–	–	103.0	–4.50	–4.59
6633.44	4.81	–1.20	–	–	–	–	65.0	–4.36	–4.52
6627.56	4.55	–1.46	69.4	–4.23	70.6	–4.16	–	–	–4.56
6625.04	1.01	–5.20	89.0	–4.32	–	–	–	–	–4.58
6608.04	2.28	–3.88	67.8	–4.48	74.0	–4.30	–	–	–4.57
6597.60	4.77	–0.95	67.6	–4.53	75.2	–4.33	–	–	–4.53
6498.95	0.95	–4.55	–	–	–	–	130.0	–4.47	–4.52
6496.46	4.77	–0.50	–	–	112.1	–4.10	103.0	–4.40	–4.52
6495.78	4.81	–0.93	–	–	85.3	–4.09	–	–	–4.57
6481.87	2.27	–2.83	–	–	–	–	124.0	–4.63	–4.60
6475.63	2.55	–2.88	108.7	–4.36	–	–	–	–	–4.40
6436.41	4.19	–2.35	45.0	–4.20	42.5	–4.21	50.0	–4.19	–4.54
6419.96	4.73	–0.12	118.8	–4.47	–	–	129.2	–4.37	–4.63
6411.66	3.65	–0.61	–	–	–	–	175.5	–4.42	–4.56
6392.54	2.28	–3.89	70.9	–4.39	70.0	–4.35	–	–	–4.58
6385.73	4.73	–1.78	29.2	–4.48	31.3	–4.41	–	–	–4.53
6330.85	4.73	–1.14	58.3	–4.54	60.6	–4.46	–	–	–4.54
6322.68	2.59	–2.26	125.6	–4.58	–	–	–	–	–4.53
6307.85	3.64	–3.21	23.1	–4.41	24.2	–4.36	–	–	–4.50
6290.97	4.73	–0.54	93.0	–4.47	101.7	–4.26	–	–	–4.54
6226.72	3.88	–2.04	62.6	–4.51	65.1	–4.41	–	–	–4.51
6187.99	3.94	–1.58	84.9	–4.46	90.8	–4.28	–	–	–4.47
6180.21	2.73	–2.56	110.6	–4.38	117.0	–4.16	–	–	–4.83
6173.34	2.21	–2.76	122.6	–4.56	124.4	–4.43	–	–	–4.50
6165.37	4.12	–1.37	80.0	–4.57	78.4	–4.54	89.0	–4.49	–4.57
6159.41	4.59	–1.82	45.8	–4.25	38.6	–4.36	41.0	–4.40	–4.58
6157.73	4.06	–1.11	111.2	–4.29	115.6	–4.14	112.0	–4.39	–4.58
6151.62	2.17	–3.18	98.9	–4.65	100.9	–4.52	109.0	–4.63	–4.56
6148.65	4.30	–2.61	21.4	–4.31	24.1	–4.22	23.0	–4.33	–4.58
6145.42	3.35	–3.60	20.6	–4.40	20.0	–4.40	17.0	–4.59	–4.61
6120.25	0.91	–5.81	50.6	–4.45	49.2	–4.42	55.0	–4.52	–4.45
6114.42	3.93	–3.28	–	–	11.3	–4.37	–	–	–4.74
6105.13	4.55	–1.94	32.8	–4.43	36.7	–4.33	–	–	–4.57
6102.18	4.83	–0.07	119.2	–4.39	117.2	–4.36	–	–	–4.57
6098.25	4.56	–1.74	50.9	–4.26	47.5	–4.30	–	–	–4.56
6096.67	3.98	–1.71	80.1	–4.38	81.3	–4.29	–	–	–4.52
6094.38	4.65	–1.50	45.4	–4.50	50.4	–4.38	–	–	–4.56
6093.65	4.61	–1.30	60.8	–4.46	64.6	–4.34	–	–	–4.54
6089.57	5.02	–0.79	73.4	–4.27	–	–	–	–	–4.55
6079.02	4.65	–0.91	75.8	–4.51	82.5	–4.32	–	–	–4.52
6078.50	4.79	–0.26	103.5	–4.49	109.6	–4.33	–	–	–4.53
6056.01	4.73	–0.30	96.1	–4.64	102.3	–4.47	–	–	–4.58
6054.10	4.35	–2.16	33.8	–4.40	30.7	–4.45	37.0	–4.41	–4.55
6034.04	4.29	–2.28	32.0	–4.39	–	–	31.0	–4.48	–4.53
6019.36	3.56	–3.20	32.0	–4.29	–	–	33.0	–4.36	–4.57
6015.25	2.21	–4.56	34.9	–4.43	–	–	–	–	–4.51
6012.75	4.54	–2.35	–	–	–	–	21.0	–4.36	–4.74
6008.58	3.88	–0.84	119.8	–4.59	–	–	–	–	–4.53
6007.96	4.63	–0.62	87.9	–4.57	–	–	91.0	–4.60	–4.57
6003.03	3.86	–1.12	108.4	–4.53	–	–	109.0	–4.64	–4.42
5881.25	4.61	–1.68	48.0	–4.31	–	–	–	–	–4.57
5879.49	4.61	–1.88	39.1	–4.29	–	–	–	–	–4.56
5873.22	4.26	–1.97	55.8	–4.27	–	–	–	–	–4.56

Table 1. (Contd.)

1	2	3	4	5	6	7	8	9	10
5864.24	4.28	–2.40	31.4	–4.29	29.1	–4.32	29.0	–4.41	–4.47
5862.36	4.53	–0.36	108.8	–4.55	116.8	–4.35	–	–	–4.52
5861.11	4.26	–2.31	32.3	–4.38	27.1	–4.48	–	–	–4.52
5859.61	4.55	–0.49	101.3	–4.53	109.0	–4.33	–	–	–4.55
5858.77	4.20	–2.13	45.3	–4.37	43.8	–4.37	45.0	–4.45	–4.57
5856.08	4.28	–1.51	68.6	–4.45	73.2	–4.30	77.0	–4.38	–4.54
5855.13	4.59	–1.54	49.0	–4.45	48.4	–4.43	50.0	–4.51	–4.52
5853.18	1.48	–5.03	49.5	–4.54	53.3	–4.42	55.0	–4.58	–4.46
5852.19	4.53	–1.17	72.3	–4.43	82.0	–4.18	77.0	–4.43	–4.50
5849.70	3.68	–2.82	34.0	–4.49	22.9	–4.72	31.0	–4.63	–4.61
5845.27	5.01	–1.70	19.5	–4.48	24.1	–4.33	26.0	–4.36	–4.63
5844.88	4.14	–2.83	16.0	–4.41	20.2	–4.27	20.0	–4.35	–4.54
5837.70	4.29	–2.13	31.7	–4.54	–	–	–	–	–4.67
5835.11	4.26	–2.09	43.1	–4.38	–	–	–	–	–4.57
5827.88	3.28	–3.10	49.2	–4.37	–	–	–	–	–4.55
5809.22	3.88	–1.59	82.8	–4.52	–	–	–	–	–4.52
5806.73	4.61	–0.82	80.1	–4.53	–	–	–	–	–4.54
5793.91	4.22	–1.55	75.2	–4.34	–	–	–	–	–4.53
5784.69	3.38	–2.24	75.7	–4.60	77.8	–4.48	–	–	(–4.56)
5778.47	2.58	–3.42	70.7	–4.46	77.2	–4.24	82.0	–4.38	–4.58
5775.09	4.20	–1.10	93.2	–4.44	96.9	–4.30	96.0	–4.49	–4.44
5769.31	4.59	–2.08	–	–	–	–	25.0	–4.47	(–4.56)
5760.35	3.63	–2.32	61.0	–4.52	61.2	–4.47	59.0	–4.66	–4.65
5752.04	4.55	–0.80	83.6	–4.54	–	–	–	–	–4.54
5732.30	4.99	–1.40	41.6	–4.30	42.0	–4.26	–	–	–4.51
5731.77	4.26	–1.06	93.1	–4.42	101.4	–4.19	–	–	–4.51
5724.40	4.28	–2.52	22.5	–4.37	–	–	–	–	–4.57
5720.90	4.55	–1.81	43.6	–4.33	49.3	–4.18	–	–	–4.53
5717.86	4.28	–1.01	95.6	–4.40	103.9	–4.17	–	–	–4.46
5705.47	4.30	–1.40	74.5	–4.41	76.4	–4.31	–	–	–4.57
5686.54	4.55	–0.56	100.8	–4.46	106.4	–4.29	–	–	–4.55
5679.02	4.65	–0.57	–	–	83.3	–4.61	–	–	–4.59
5677.70	4.10	–2.56	27.3	–4.41	24.0	–4.47	–	–	–4.55
5560.38	4.43	–1.01	75.9	–4.62	79.6	–4.47	–	–	–4.54
5554.90	4.55	–0.23	–	–	125.2	–4.32	–	–	–4.48
5552.70	4.95	–1.69	28.0	–4.33	25.7	–4.36	–	–	–4.57
5546.63	4.37	–1.04	88.8	–4.39	94.7	–4.20	–	–	–4.53
5544.04	4.22	–0.92	91.0	–4.62	99.0	–4.39	–	–	–4.52
5539.83	4.29	–2.29	32.5	–4.35	33.0	–4.32	–	–	–4.56
5525.55	4.23	–1.20	81.9	–4.51	93.2	–4.22	–	–	–4.45
5522.40	4.21	–1.40	70.0	–4.59	76.3	–4.40	–	–	–4.52
5445.04	4.39	0.19	–	–	–	–	155.7	–4.57	–4.68
5441.35	4.31	–1.55	62.9	–4.46	64.5	–4.38	71.0	–4.39	–4.45
5432.95	4.44	–0.61	100.3	–4.50	103.6	–4.38	–	–	–4.55
5417.04	4.41	–1.37	59.6	–4.60	65.2	–4.43	67.2	–4.54	–4.55
5412.79	4.43	–1.73	48.4	–4.43	51.0	–4.35	56.7	–4.35	–4.56
5406.78	4.37	–1.35	66.8	–4.52	68.2	–4.43	71.6	–4.51	–4.52
5401.29	4.32	–1.68	56.5	–4.45	60.3	–4.32	67.7	–4.31	–4.56
5398.28	4.44	–0.51	–	–	97.2	–4.59	106.9	–4.56	–4.62
5395.22	4.44	–1.67	38.0	–4.69	47.2	–4.47	53.5	–4.46	–4.56
5386.34	4.15	–1.67	51.6	–4.74	62.1	–4.49	–	–	–4.54
5385.55	3.69	–3.08	13.5	–4.73	17.9	–4.56	–	–	–4.57
5379.57	3.69	–1.44	95.2	–4.58	106.4	–4.27	–	–	–4.51
5376.84	4.29	–2.00	45.0	–4.38	47.0	–4.31	–	–	–4.57
5373.71	4.47	–0.69	–	–	92.6	–4.47	–	–	–4.56
5358.10	3.29	–3.23	38.6	–4.40	36.5	–4.41	–	–	–4.49
5326.79	4.40	–1.97	41.9	–4.35	44.3	–4.27	49.0	–4.29	–4.53
5322.05	2.27	–2.81	102.5	–4.67	107.6	–4.46	–	–	–4.42

Table 1. (Contd.)

1	2	3	4	5	6	7	8	9	10
5321.11	4.42	–1.24	71.9	–4.45	69.4	–4.45	72.0	–4.55	–4.49
5320.05	3.63	–2.43	56.5	–4.47	–	–	61.0	–4.48	–4.61
5318.04	3.00	–4.13	–	–	14.9	–4.38	–	–	–4.87
5315.78	3.62	–3.13	23.7	–4.45	22.2	–4.46	20.0	–4.62	–4.47
5315.07	4.35	–1.44	67.4	–4.42	74.3	–4.22	80.0	–4.26	–4.53
5295.32	4.40	–1.50	57.1	–4.52	56.3	–4.50	64.0	–4.47	–4.54
5294.55	3.62	–2.64	44.6	–4.50	45.2	–4.45	48.0	–4.52	–4.58
5293.97	4.12	–1.72	60.7	–4.54	65.0	–4.40	70.0	–4.45	–4.62
5285.13	4.43	–1.42	58.5	–4.54	65.4	–4.35	64.3	–4.51	–4.60
5253.48	3.28	–1.45	113.4	–4.63	116.4	–4.49	138.0	–4.29	–4.52
5243.78	4.26	–0.94	86.5	–4.62	95.5	–4.37	96.3	–4.52	–4.55
5242.50	3.63	–0.91	–	–	116.2	–4.66	132.4	–4.55	–4.68
5228.37	4.22	–1.05	89.2	–4.49	92.7	–4.36	–	–	–4.53
5223.19	3.63	–2.21	61.4	–4.58	59.9	–4.56	–	–	–4.55
5197.94	4.30	–1.42	–	–	–	–	81.2	–4.31	–4.50
5159.06	4.28	–0.82	91.9	–4.60	–	–	111.6	–4.30	–4.50
5145.11	2.20	–3.12	102.7	–4.41	110.6	–4.12	112.6	–4.37	–4.41
5143.73	2.20	–3.74	70.1	–4.52	78.7	–4.24	89.2	–4.26	–4.48
5141.75	2.42	–1.97	–	–	–	–	148.2	–4.55	–4.60
5136.09	4.17	–1.90	53.2	4.44	56.9	–4.32	–	–	–4.67
5124.64	3.30	–2.92	54.1	–4.38	–	–	–	–	–4.35
FeII									
6456.39	3.90	–2.03	84.6	–4.45	88.2	–4.35	91.6	–4.41	–4.52
6446.39	6.22	–2.07	–	–	–	–	8.0	–4.31	–4.51
6442.95	5.55	–2.47	10.7	–4.30	14.5	–4.12	–	–	–4.63
6432.68	2.89	–3.50	68.9	–4.45	65.9	–4.48	69.8	–4.39	–4.54
6416.93	3.89	–2.74	–	–	–	–	61.5	–4.40	(–4.54)
6179.39	5.57	–2.55	–	–	9.8	–4.28	–	–	–4.53
6149.24	3.87	–2.67	56.8	–4.45	61.2	–4.33	60.0	–4.46	–4.56
6113.33	3.21	–4.09	32.4	–4.33	30.8	–4.37	29.0	–4.54	–4.55
6084.10	3.20	–3.76	46.6	–4.33	47.5	–4.29	–	–	–4.53
5991.38	3.15	–3.51	61.2	–4.31	–	–	–	–	–4.54
5425.26	3.20	–3.22	61.1	–4.55	66.6	–4.39	59.9	–4.58	–4.49
5414.07	3.22	–3.53	48.4	–4.51	47.2	–4.52	55.2	–4.27	–4.58
5325.56	3.22	–3.27	64.5	–4.40	63.7	–4.39	79.0	–4.28	–4.49
5264.81	3.23	–3.01	71.2	–4.48	79.4	–4.25	83.6	–4.20	–4.55
5234.63	3.22	–2.19	103.0	–4.60	104.9	–4.50	121.4	–4.42	–4.46
5197.58	3.23	–2.23	–	–	–	–	117.3	–4.41	–4.51
5161.18	2.86	–4.24	37.1	–4.46	–	–	–	–	–4.51
5132.67	2.81	–3.99	49.4	–4.47	–	–	56.1	–4.56	–4.52
CoI									
6632.44	2.27	–1.83	–	–	52.8	–6.85	48.0	–7.09	–7.12
6477.86	3.76	–0.73	18.9	–6.97	17.5	–7.00	16.0	–7.14	–7.12
6455.00	3.63	–0.26	–	–	–	–	57.8	–6.88	–7.14
6429.90	2.14	–2.30	–	–	29.9	–6.96	34.3	–7.01	–7.23
6347.84	4.39	–0.09	–	–	21.8	–6.81	–	–	–7.16
6188.98	1.71	–2.19	62.2	–6.99	–	–	–	–	–7.13
6117.00	1.78	–2.45	41.1	–7.02	36.6	–7.07	44.0	–7.09	–7.17
6093.15	1.74	–2.27	56.2	–6.97	–	–	–	–	–7.17
6000.67	3.61	–0.80	22.7	–6.95	–	–	–	–	–7.17
5530.78	1.70	–2.04	71.3	–6.91	–	–	–	–	–7.12
5523.34	2.32	–1.58	44.9	–7.14	45.4	–7.09	–	–	–7.11
5381.76	4.24	–0.13	21.6	–6.92	17.1	–7.04	–	–	–7.07
5368.93	3.51	–1.18	–	–	13.8	–6.90	–	–	–7.16
5359.19	4.15	0.11	26.8	–7.13	24.7	–7.16	–	–	–7.16
5352.05	3.56	–0.02	63.5	–6.91	–	–	–	–	–7.09
5342.70	4.00	0.62	60.0	–7.12	63.9	–7.00	66.0	–7.10	–7.10
5336.16	4.01	–0.52	–	–	15.7	–6.94	–	–	(–7.14)
5325.27	4.02	–0.03	35.4	–6.94	32.0	–6.99	–	–	–7.12

Table 1. (Contd.)

1	2	3	4	5	6	7	8	9	10
NiI									
6772.36	3.64	–0.89	87.2	–5.70	86.0	–5.66	91.0	–5.76	(–5.80)
6767.78	1.83	–1.95	139.8	–5.80	–	–	–	–	–5.80
6643.64	1.67	–1.86	155.6	–5.80	–	–	–	–	–5.83
6635.15	4.40	–0.71	59.0	–5.56	64.5	–5.41	56.0	–5.70	–5.79
6598.59	4.22	–0.88	53.5	–5.69	58.3	–5.57	–	–	–5.79
6424.86	4.17	–1.32	–	–	42.5	–5.49	43.8	–5.57	–5.80
6327.60	1.68	–3.01	–	–	100.2	–5.48	–	–	–5.78
6322.17	4.15	–1.16	–	–	51.9	–5.48	–	–	–5.79
6316.58	4.15	–1.90	–	–	18.0	–5.51	–	–	–5.76
6223.98	4.10	–0.93	62.4	–5.58	66.7	–5.46	–	–	–5.78
6204.60	4.09	–1.09	53.2	–5.61	57.8	–5.49	–	–	–5.79
6186.71	4.10	–0.87	59.3	–5.71	70.2	–5.44	–	–	–5.77
6177.25	1.83	–3.47	61.9	–5.68	63.4	–5.60	–	–	–5.89
6176.82	4.09	–0.17	95.0	–5.71	103.0	–5.49	–	–	–5.79
6175.37	4.09	–0.45	–	–	79.3	–5.68	–	–	–5.62
6133.95	4.07	–1.76	21.9	–5.63	18.8	–5.71	24.0	–5.65	–5.86
6130.17	4.25	–0.92	49.8	–5.67	50.0	–5.64	52.0	–5.71	–5.81
6128.99	1.67	–3.30	80.8	–5.65	88.3	–5.42	89.0	–5.67	–5.80
6118.06	4.09	–2.08	–	–	13.7	–5.53	–	–	–5.76
6111.06	4.07	–0.75	67.1	–5.69	68.8	–5.62	67.0	–5.80	–5.80
6108.12	1.68	–2.54	112.6	–5.77	144.8	–5.62	–	–	–5.72
6086.28	4.26	–0.39	78.8	–5.60	78.6	–5.55	–	–	–5.77
6053.68	4.23	–1.01	–	–	49.8	–5.57	–	–	–5.82
6007.31	1.67	–3.30	76.6	–5.73	–	–	79.0	–5.84	–5.81
5996.74	4.23	–0.96	52.0	–5.60	–	–	–	–	–5.94
5857.76	4.17	–0.34	87.4	–5.57	–	–	–	–	–5.78
5847.01	1.67	–3.39	76.8	–5.63	83.1	–5.41	88.0	–5.57	–5.80
5805.22	4.17	–0.51	63.5	–5.88	–	–	–	–	–5.78
5760.85	4.09	–0.72	66.2	–5.70	70.2	–5.58	66.0	–5.81	–5.78
5748.35	1.68	–3.15	78.7	–5.80	–	–	–	–	–5.79
5694.98	4.09	–0.57	–	–	75.7	–5.59	–	–	–5.81
5682.20	4.10	–0.34	–	–	88.7	–5.54	–	–	–5.76
5537.10	3.85	–2.18	–	–	16.3	–5.58	–	–	–5.86
5435.87	1.99	–2.43	104.4	–5.54	106.8	–5.39	–	–	–5.75
5392.33	4.15	–1.28	35.4	–5.69	29.1	–5.80	–	–	–5.82
5388.34	1.93	–3.37	–	–	58.8	–5.60	–	–	–5.82
5347.71	3.78	–2.01	–	–	22.0	–5.65	–	–	–5.85
5259.48	3.74	–1.80	31.3	–5.70	35.4	–5.59	46.5	–5.47	–5.81
5176.56	3.90	–0.40	–	–	–	–	92.2	–5.76	–5.79
5157.98	3.61	–1.53	45.6	–5.81	–	–	52.0	–5.79	–5.83
5155.77	3.90	0.06	–	–	–	–	118.2	–5.70	–5.96
5155.13	3.90	–0.60	73.1	–5.85	–	–	86.6	–5.67	–5.79
5115.40	3.83	–0.03	–	–	–	–	110.0	–5.82	–5.88
5102.98	1.68	–2.86	90.0	–5.73	–	–	–	–	–5.73
YII									
6795.41	1.72	–1.12	26.2	–9.62	28.6	–9.54	–	–	(–9.78)
5728.89	1.84	–1.11	20.3	–9.62	18.1	–9.68	–	–	–9.91
5402.78	1.84	–0.57	39.7	–9.67	37.2	–9.71	41.8	–9.78	–9.81
5320.78	1.08	–1.94	19.8	–9.63	19.6	–9.62	–	–	–9.64
5289.82	1.03	–1.84	23.9	–9.67	21.7	–9.72	29.0	–9.70	–9.79
5119.12	0.99	–1.35	48.2	–9.65	49.4	–9.58	–	–	–9.68
BaII									
6496.89	0.60	–0.08	–	–	183.0	–9.60	–	–	–9.95
6141.72	0.70	0.40	193.8	–9.89	178.1	–9.97	190.0	–9.95	–10.17
5853.68	0.60	–0.80	115.9	–9.75	121.4	–9.54	114.0	–9.92	–9.88

Table 1. (Contd.)

1	2	3	4	5	6	7	8	9	10
LaII									
6774.28	0.13	–1.63	21.5	–10.76	25.1	–10.64	24.0	–10.86	–10.80
6390.48	0.32	–1.42	22.9	–10.69	21.9	–10.70	–	–	–10.81
6320.41	0.17	–1.30	30.8	–10.78	30.4	–10.77	–	–	–10.83
CeII									
6043.39	1.21	–0.25	10.8	–10.48	15.9	–10.27	17.0	–10.39	–10.47
5330.58	0.87	–0.30	19.7	–10.45	19.6	–10.45	23.0	–10.52	–10.52
5274.24	1.04	0.34	38.5	–10.44	41.9	–10.33	48.1	–10.41	–10.47
PrII									
6165.94	0.92	–0.26	–	–	12.4	–11.05	–	–	(–11.39)
5322.78	0.48	–0.31	18.7	–11.24	17.4	–11.27	21.0	–11.34	–11.42
5259.73	0.63	–0.04	22.3	–11.23	–	–	25.5	–11.31	–11.36
5219.02	0.79	0.11	–	–	13.9	–11.46	–	–	–11.39
NdII									
5842.39	1.28	–0.49	9.5	–10.49	–	–	11.0	–10.56	–10.75
5431.53	1.12	–0.29	–	–	17.4	–10.52	–	–	–10.75
5416.38	0.86	–0.82	9.6	–10.60	8.8	–10.64	7.3	–10.89	–10.78
5385.89	0.74	–0.83	8.8	–10.77	16.8	–10.42	–	–	–10.70
5356.99	1.26	–0.14	16.3	–10.56	13.7	–10.65	–	–	–10.60
5319.82	0.55	–0.10	56.2	–10.44	53.7	–10.44	57.0	–10.62	–10.75
5311.46	0.98	–0.31	21.0	–10.56	22.9	–10.49	–	–	–10.91
5306.49	0.86	–0.65	12.5	–10.64	15.6	–10.50	–	–	–10.53
5276.87	0.86	–0.71	11.2	–10.63	18.8	–10.34	17.1	–10.94	–10.71

result of importance for analyses of stellar chemical compositions and searches for abundance anomalies.

To summarize, we briefly describe the main points of our approach.

(a) All analyses are based on the model atmospheres of [9].

(b) The Sun is used as a reference star.

(c) The stellar-atmosphere parameters are determined by analyzing the observed spectra using the procedure described above.

(d) The solar-atmosphere parameters ($T_{\rm eff}$ = 5887 K and $\log g$ = 4.57 [12]), determined in the same way as the atmosphere parameters for the program stars, are used to estimate the solar abundances in terms of the adopted grid [9].

(e) To avoid errors due to inaccurate oscillator strengths, the star–Sun abundance differences are determined separately for each spectral line studied and the results subsequently averaged.

We believe that this approach should minimize the errors and allow very accurate comparisons of the program objects.

Our results for the three Hyades giants are summarized in Table 1. For each star, we give the derived atmosphere parameters and the abundance estimates obtained for each selected line using the Width9 program. To compute the model atmospheres corresponding to the inferred parameters, we employed the same Atlas9 program that Kurucz used to construct his grid [9]. In addition, we give the corresponding solar abun-

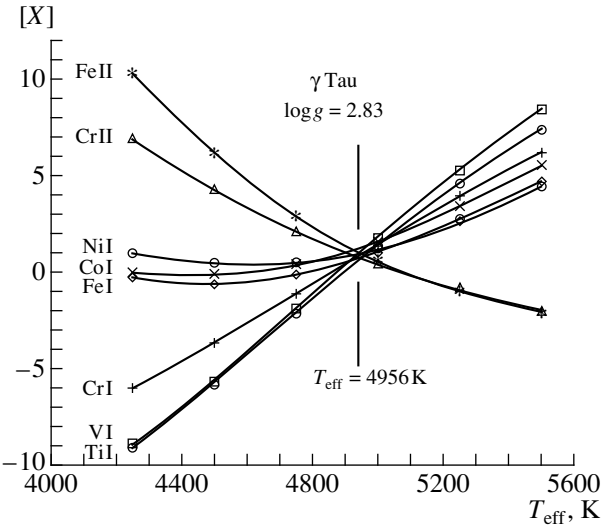

Fig. 1. Abundances of iron-group elements relative to the solar values calculated from the observed equivalent widths of absorption lines in the spectrum of γ Tau for $\log g$ = 2.83 and various effective temperatures.

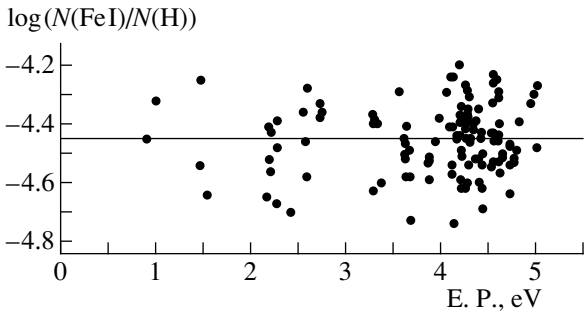

Fig. 2. Derived iron abundances, log ε (Fe), plotted as a function of the excitation potentials of the lower FeI levels in the spectrum of γ Tau. Calculations were performed with the model-atmosphere parameters $T = 4956$ K, $\log g = 2.83$, $V_t = 1.35$ km/s.

dance for each line. In some cases, the solar abundances differed significantly from the values averaged over all lines of the corresponding element, due to poor equivalent-width determinations for the corresponding lines in the solar spectrum (as a rule, the weakest lines). In these cases, we substituted the mean abundance for the discrepant solar value and give it in parentheses. Table 2 and Fig. 3 present the resulting relative elemental abundances (with respect to the Sun) for the atmospheres of the giants studied. For comparison, Fig. 4 shows the elemental abundances in three field stars.

Analysis of Table 2 and Figs. 3 and 4 leads us to the following conclusions.

(1) All three Hyades giants have virtually identical elemental abundance curves, as is to be expected for coeval stars in the same evolutionary stage.

(2) The overall metallicity (i.e., mean abundance of iron-group elements) of the Hyades giants studied is nearly the same as the observed metallicities of Hyades dwarfs (see, e.g., [4]). Table 2 lists the metallicities derived from iron-group elements. Note that the somewhat higher value obtained for δ Tau is still consistent with published Hyades metallicities: According to Boesgaard and Friel [4], two of 14 program dwarfs have metallicities of +0.173 and +0.177 dex, respectively, whereas the average value

Table 2. Atmospheric elemental abundances in Hyades red giants compared to the corresponding solar abundances

	γ Tau		δ Tau		ε Tau	
T (K) =	4956		4980		4880	
$\log g$ =	2.83		2.84		2.50	
v_t (km/s) =	1.35		1.25		1.46	
Element	Number of lines	[X]	Number of lines	[X]	Number of lines	[X]
NaI	2	+0.43 ± 0.02	2	+0.51 ± 0.02	2	+0.51 ± 0.05
MgI	4	+0.27 ± 0.04	2	+0.34 ± 0.02		
AlI	2	+0.23 ± 0.00	2	+0.27 ± 0.02	2	+0.31 ± 0.01
SiI	12	+0.18 ± 0.09	16	+0.25 ± 0.08	5	+0.20 ± 0.07
CaI	5	+0.12 ± 0.08	5	+0.19 ± 0.11	3	+0.10 ± 0.11
ScII	9	+0.11 ± 0.05	7	+0.20 ± 0.06		
TiI	28	+0.10 ± 0.08	33	+0.15 ± 0.12	8	+0.06 ± 0.08
VI	13	+0.12 ± 0.09	15	+0.21 ± 0.09	6	+0.07 ± 0.08
VII					2	+0.10 ± 0.01
CrI	22	+0.10 ± 0.09	19	+0.15 ± 0.10	12	+0.11 ± 0.05
CrII	6	+0.08 ± 0.07	8	+0.18 ± 0.08	1	+0.05
MnI			6	+0.18 ± 0.10	1	+0.10
FeI	127	+0.11 ± 0.12	107	+0.19 ± 0.12	66	+0.11 ± 0.11
FeII	14	+0.11 ± 0.09	12	+0.18 ± 0.11	13	+0.05 ± 0.11
CoI	12	+0.13 ± 0.08	15	+0.20 ± 0.13	6	+0.10 ± 0.09
NiI	29	+0.11 ± 0.09	31	+0.24 ± 0.10	16	+0.11 ± 0.10
YII	6	+0.12 ± 0.02	6	+0.14 ± 0.07	2	+0.06 ± 0.04
BaII	2	+0.20 ± 0.07	3	+0.34 ± 0.01	2	+0.20 ± 0.02
LaII	3	+0.08 ± 0.04	3	+0.14 ± 0.15	1	–0.06
CeII	3	+0.03 ± 0.02	3	+0.14 ± 0.05	3	+0.06 ± 0.06
PrII	2	+0.15 ± 0.01	3	+0.13 ± 0.17:	2	+0.06 ± 0.01
NdII	8	+0.13 ± 0.09	8	+0.21 ± 0.07	4	+0.01 ± 0.09
			M			
		+0.10 ± 0.02		+0.19 ± 0.03		+0.08 ± 0.04

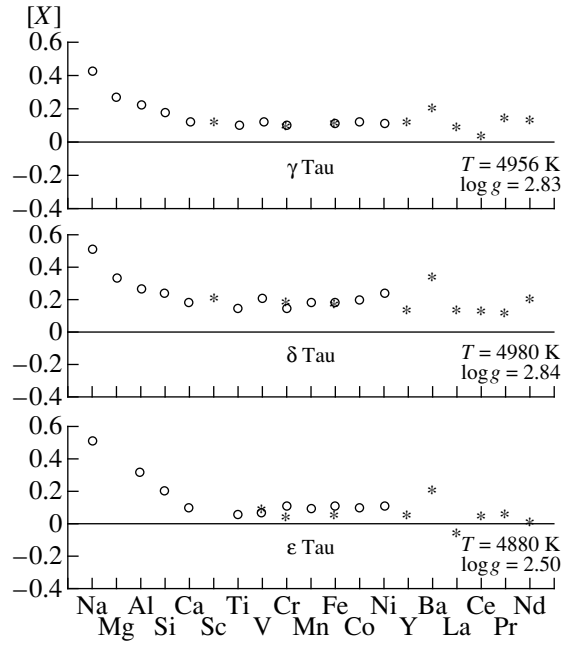

Fig. 3. Atmospheric elemental abundances for Hyades red giants relative to the corresponding solar abundances. The circles and asterisks show the abundances of neutral elements and ions, respectively.

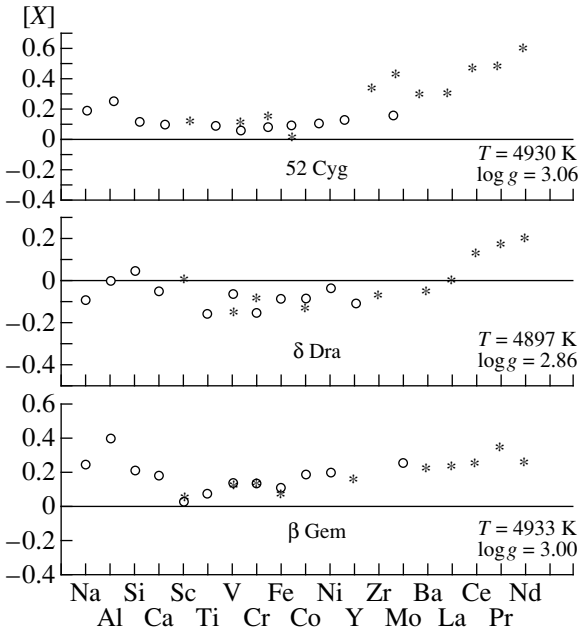

Fig. 4. Atmospheric elemental abundances in field red giants relative to the corresponding solar abundances. The circles and asterisks show the abundances of neutral elements and ions, respectively.

for all 14 stars is +0.127 dex, suggesting some scatter in the heavy-element abundances among the cluster stars.

(3) All three Hyades giants exhibit anomalously high Na abundances. The same is true for field giants and supergiants [10, 13], and this effect is explained by the convective dredge-up of processed material in the main-sequence stage, during the star's transition into a red giant. Sodium abundance anomalies in the atmospheres of Hyades giants have already been pointed out by other authors [5–7]. Note that the Hyades giants lie somewhat above the "log g–Na abundance anomaly" dependence for the field stars [13].

(4) The other light elements Al and Si also exhibit slight overabundances similar to those observed in the field stars (see Figs. 3 and 4).

(5) We found the abundances of *s*-process elements relative to iron to be normal in all three giants (the Ba overabundance is probably due to departure from LTE in the case of the BaII lines studied), whereas the field stars are characterized by higher-than-solar *s*-element abundances (see Fig. 4). Note that Griffin and Holweger [5] also found normal *s*-process element abundances in γ Tau.

The detected differences between the chemical compositions of the Hyades and field giants is probably due to the age difference between the two groups of objects. The Hyades is a young cluster, one tenth the age of the Sun [4], and mixing processes in its giants have been going on for a relatively short time. These processes are not yet fully developed and have not reached the deeper core layers. Field stars are, on average, older, and the development of mixing processes over a longer time could result in the dredge-up of material from deeper layers. In both cases, different processed material could be carried to the star's surface. Note also that the field stars do not make up as homogeneous a group as the Hyades giants: They can have different ages, metallicities, masses, and, to some extent, rates of evolution, so they can include both stars without anomalous *s*-process element abundances and those clearly exhibiting such anomalies (Fig. 4).

ACKNOWLEDGMENTS

This work was partially supported by the Russian Foundation for Basic Research (project code 97-02-17959). The observations on which this research is based were obtained with a SDS-9000 Photometrics Gmbtl CCD mounted on the 2.6-m telescope of the Crimean Astrophysical Observatory, which was acquired through financial support from the International Science Foundation (grants R2Q000 and U1C000) and ESO C&EE Program (A-05-067).

REFERENCES

1. M. A. C. Perryman, A. G. A. Brown, Y. Lebreton, *et al.*, Astron. Astrophys. **331**, 81 (1998).
2. B. Twarog, Astrophys. J. **242**, 242 (1980).

3. R. G. Carlberg, P. C. Dawson, T. Hsu, and D. A. Vandenberg, Astrophys. J. **294**, 674 (1985).
4. A. M. Boesgaard and E. D. Friel, Astrophys. J. **351**, 467 (1990).
5. R. E. M. Griffin and H. Holweger, Astron. Astrophys. **214** (1989).
6. T. V. Mishenina, N. S. Komarov, and L. É. Kantsen, Izv. SAO **31**, 82 (1991).
7. I. S. Savanov and M. E. Boyarchuk, Izv. Krym. Astrofiz. Obs. **86**, 3 (1992).
8. I. S. Savanov and Yu. Yu. Selezneva, Astrofizika **39** (1), 5 (1996).
9. R. L. Kurucz, Rev. Mex. Astron. Astrofis. **23**, 181 (1992).
10. A. A. Boyarchuk, L. I. Antipova, M. E. Boyarchuk, *et al.*, Astron. Zh. **73**, 862 (1996).
11. A. A. Boyarchuk, I. S. Savanov, M. E. Boyarchuk, *et al.*, Izv. Krym. Astrofiz. Obs. **94**, 36 (1998).
12. A. A. Boyarchuk, L. I. Antipova, M. E. Boyarchuk, *et al.*, Astron. Zh. **75**, 586 (1998).
13. A. A. Boyarchuk and L. S. Lyubimkov, Izv. Krym. Astrofiz. Obs. **66**, 130 (1983).

Translated by A. Dambis

Astronomy Reports, Vol. 44, No. 2, 2000, pp. 89–102. Translated from Astronomicheskiĭ Zhurnal, Vol. 77, No. 2, 2000, pp. 109–123.

Photometric Parameters of the Dwarf Nova SS Cygni in the Quiescent State

I. B. Voloshina and T. S. Khruzina

Sternberg Astronomical Institute,
Universitetskiĭ pr. 13, Moscow, 119899 Russia

Received June 22, 1998

Abstract—The mean 1983–1996 *UBV* light curves of the dwarf nova SS Cyg are used to derive the binary parameters in the quiescent state. Solutions are obtained for a classical hot-spot model and a model with an energy source lying outside the accretion disk. Photometric and spectroscopic data are combined to infer the masses and radii of the binary components. The white dwarf in SS Cyg is one and a half times as massive as the red dwarf, $q = M_{wd}/M_{rd} \sim 1.45$, $M_{rd} \sim 0.46M_{\odot}$, and $M_{wd} \sim 0.66M_{\odot}$. The orbital inclination of the system is $i \simeq 51°$–$54°$. The contribution of the accretion disk to the total flux in the quiescent state is estimated to be ~47–49% and ~54% in the *VU* and *B* filters, respectively. The hot spot contributes less than ~3% to the total optical flux. In the "non-classical" hot-spot model, the disk and bulge contributions are 27 and 2–8%, respectively, depending on the orbital phase. The shape of the mean light curves of SS Cyg suggests asymmetric heating of the red-dwarf surface in the quiescent state by high-temperature radiation generated in the hot-spot region. © *2000 MAIK "Nauka/Interperiodica".*

1. INTRODUCTION

We performed wide-band photometry of SS Cyg, one of the brightest cataclysmic variables in the Northern sky, as part of a composite observational program aimed at studying close binaries in late evolutionary stages. This program has been carried out in recent years at the Sternberg Astronomical Institute of Moscow State University. The goal of the observations is to detect photometric variability of the binary system.

We present the parameters of the dwarf nova SS Cyg in the quiescent state derived from an analysis of its mean light curves from 1983 through 1996. We used cataclysmic-variable models and the corresponding computer code of Khruzina [1] to construct synthetic light curves for the binary. The classical or standard cataclysmic-variable model is based on the hypothesis that there is a "hot spot" in the system, which forms as a result of shock interaction of the gaseous stream flowing from the inner Lagrangian point with the outer edge of the accretion disk (see, e.g., [2–4]). Figure 1a shows a schematic of the main components of this type of model. This classical hot-spot model can explain fairly well on a qualitative level typical light curves of cataclysmic variables in the quiescent state. As a rule, models with low-luminosity hot spots fit the observations satisfactorily, yielding reasonable spot parameters, such as the size, luminosity, and position angle of the spot (see, e.g., [5–8]). However, the classical model faces certain difficulties when applied to the light curves of cataclysmic variables in active states or to anomalous dwarf-nova light curves with two humps at different phases, a single hump on the rising branch, or a hump with no signs of eclipse.

Three-dimensional numerical simulations of the outflow of matter in semi-detached binaries without magnetic fields [9, 10] argue against classical hot spots resulting from shock interaction between the accretion disk and the stream flowing from the inner Lagrangian point. These computations indicate that the interaction of the stream with the gaseous envelope surrounding the white dwarf produces an extended shock along the stream edge, which has the same manifestations as a hot spot in the accretion disk. This model could explain both typical and anomalous light curves of cataclysmic variables without resorting to additional assumptions [11]. In cataclysmic variables with anomalous light curves, the shock radiation contributes substantially to the total flux, often determining the overall appearance of the dwarf-nova light curve [11]. The appearance of typical light curves, such as that of SS Cyg, is determined primarily by the radiation of the red dwarf and accretion disk, whereas the contribution of the shock radiation is negligible. This fact, together with the substantial reduction of calculation time implied, led us to adopt the classical hot-spot model when analyzing the *UBV* light curves of SS Cyg to determine the parameters of the red and white dwarfs and the accretion disk in a first approximation. We used a model with a bulge energy source located outside the accretion disk (Fig. 1b) to refine the parameters of the accretion disk and the "bulge spot."

Section 2 provides some basic information about SS Cyg; Sections 3 and 4 describe our observations and the mean light curves; Sections 5 and 6 outline the methods used to compute the synthetic light curves of the cataclysmic variable and to solve for the parameters

1063-7729/00/4402-0089$20.00 © 2000 MAIK "Nauka/Interperiodica"

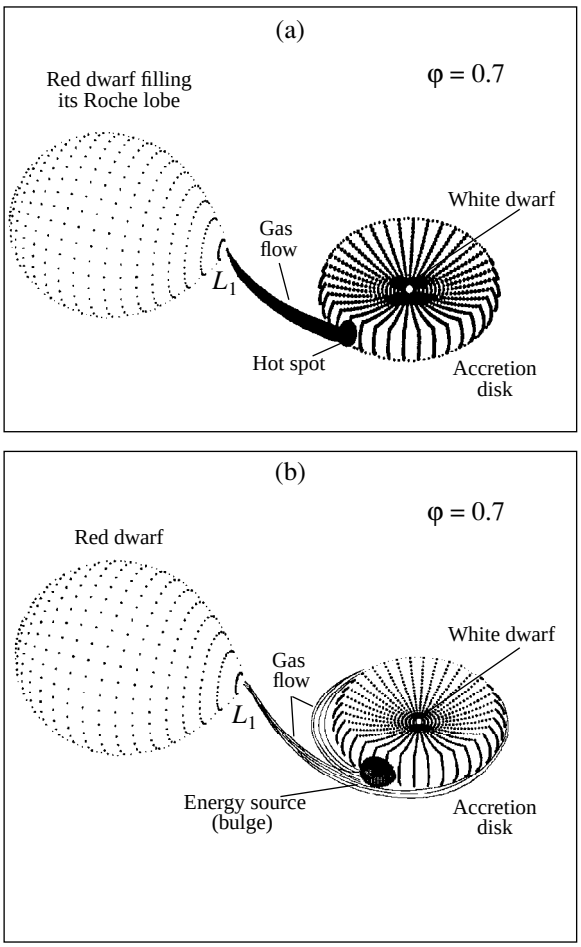

Fig. 1. Schematic of models of the dwarf nova SS Cyg with (a) classical and (b) nonclassical hot spots. The orbital phase is φ = 0.7. The binary parameters are $q = 1.5$, $i = 52°$, $R_d = 0.45\xi = 0.23a$, and $R_{wd} = 0.011\xi = 0.0061a$; the thickness of the outer disk edge is $2h = 0.11a$. (a) The radius and azimuth of the hot spot are $R_{sp} = 0.016a$ and 67°, and (b) the bulge parameters are $a_b = 0.06a$, $c_b = 0.04a$, and azimuth 81°. L_1 is the inner Lagrangian point.

of the problem; and Section 7 presents the solutions to the *UBV* light-curves of SS Cyg and discusses the range of admissible parameters for the system. Section 8 presents the light-curve solution for a non-classical bulge-spot model, and Section 9 summarizes our results.

2. BASIC FACTS ABOUT SS CYG

Cataclysmic variables or dwarf novae are low-mass interacting binaries with orbital periods of the order of several hours that consist of a compact object (white dwarf) and a K or M star (usually on the main sequence) that fills its Roche lobe (Fig. 1). Matter from the K star flows onto its companion through the inner Lagrangian point. The white dwarfs in such systems usually have rather weak magnetic fields. Dwarf novae exhibit irregular recurrent bursts with amplitudes from 2^m to $4\overset{m}{.}5$ on time scales ranging from one week to several months [12–16].

The brightest dwarf nova SS Cyg, discovered in the last century, is among the best studied binaries of this type. SS Cyg exhibits an outburst approximately once every 50 days [17], when the star's magnitude increases from 12^m to $8\overset{m}{.}5$. The binary remains in the quiescent state from four to ten weeks. The optical spectrum of SS Cyg in the quiescent state is dominated by Balmer emission lines and weaker He I lines. This spectrum, typical of cataclysmic variables, is superimposed on the absorption lines of the red component—a K5 V star [18, 19]. Szkody [17, 20, 21] has performed infrared photometry of SS Cyg. The star was the first dwarf nova found to be an X-ray source [22, 23]. Statistical analyses of the binary parameters have been performed in [24–27]. Detailed analyses of spectroscopic data are presented in [28–30]. The orbital inclination of SS Cyg has been estimated to be $i \sim 35$–$40°$, based on the lack of eclipses in this system (i.e., indirectly).

Although observations of SS Cyg span almost one hundred years, there are only a few light-curve studies that cover the time scale of the orbital period. The earliest studies [31–33] revealed no orbital modulations, while long-term photometric observations of SS Cyg in the quiescent state [34, 35] show strong evidence of such modulations with an amplitude of up to $0\overset{m}{.}2$. The presence of orbital light modulations in SS Cyg was subsequently confirmed by Bruch [36]. Most authors have attributed the observed inconsistencies between the spectroscopic and photometric data to the fact that they refer to different activity states.

3. PHOTOMETRY OF SS CYG

We observed SS Cyg in the quiescent state (i.e., between outbursts, $V \sim 11$–12^m) using a *UBV* photometer installed on the 60-cm telescope of the Crimean laboratory of the Sternberg Astronomical Institute. The photometric errors were 1–2% and 2–3% in the *BV* and *U* filters, respectively. The lengths of individual one-night observing runs were comparable to the orbital period in most cases and equal to six to seven hours. The entire dataset has a mean temporal resolution of about seven minutes. We obtained more than 2000 measurements in each filter from 1983 through 1996.

We observed SS Cyg using a standard differential photometry technique, using BD+42°4186 ($V = 9\overset{m}{.}8$, $B–V = 0\overset{m}{.}38$, and $U–V = 0\overset{m}{.}27$ [37]) as a standard star. We did not perform air-mass corrections since the program and comparison star are close to each other in the sky. We reduced all data to a heliocentric system.

4. MEAN LIGHT CURVES

We constructed the mean light curves of SS Cyg using the orbital elements derived by Voloshina and Lyutyĭ [35]:

$$Min.phot.I = \text{JD } 2444842.07537 + 0^{\text{d}}.2751302E,$$

where the time of the primary photometric minimum *Min.phot.I* corresponds to superior conjunction of the white dwarf (note that the time of minimum reported in [35] corresponds to inferior conjunction). Figure 2a shows one of our light curves of SS Cyg in the *B* filter by means of example. In addition to the periodic component, the light curve exhibits rapid, irregular fluctuations on time scales of several minutes. Note that the light curves are based exclusively on observations made on moonless nights with good seeing. Since the observations of SS Cyg were made at various phases of the outburst cycle, we subtracted the corresponding nightly magnitude-averaged fluxes from individual observations to allow for the night-to-night variations of the average magnitude.

We computed the mean *UBV* light curves (20 normal points) without allowing for the errors in the individual observations, since these are more or less the same for all data points. We excluded untrustworthy data. Figure 2b shows the mean light curves of SS Cyg in the *U*, *B*, and *V* filters. For convenience, we have shifted the curves by $0^m.1$ relative to each other. The orbital mean light curves of SS Cyg have the form of a double wave with maxima of different heights and minima separated by half the period. The mean light curves have amplitudes of $0^m.138$ and $0^m.128$ in the *VB* and *U* filter, respectively. Table 1 gives the normal-point values used to derive the parameters of SS Cyg.

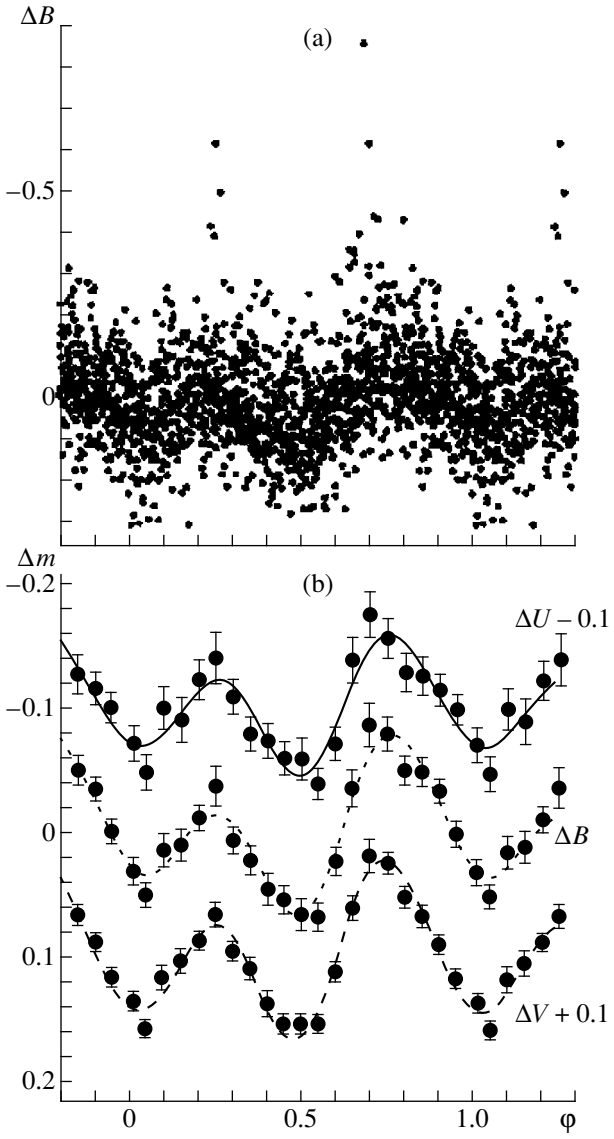

Fig. 2. Orbital light curves of SS Cyg in the quiescent state: (a) the observed light curve based on all *B*-band photometry from 1983 through 1996; (b) mean light curves of SS Cyg relative to the comparison star (dots). Solid, dotted, and dashed curves show theoretical curves computed with the best-fit binary parameters (Table 2) in the *U*, *B*, and *V* filters, respectively. Phase $\varphi = 0.0$ corresponds to superior conjunction of the white dwarf.

5. ADOPTED MODEL FOR THE SYSTEM

The optical orbital variability of dwarf novae is usually attributed to ellipsoidal variations of the red dwarf, possible white-dwarf eclipses, and partial (or total) eclipses of the accretion disk (which surrounds the white dwarf) and of a bright formation—the so-called hot spot that forms where the accreting gas stream flowing from the inner Lagrangian point impacts the matter surrounding the white dwarf. In the classical model (model I), the hot spot is located at the outer edge of the disk, whereas in the nonclassical model suggested by Bisikalo *et al.* [9–11] (model II), the hot spot has a form of an extended shock along the border of the outflowing stream. Figures 1a and 1b illustrate these two models.

Spectroscopy and photometry of SS Cyg suggest that the contribution of the hot spot to the total flux is rather small and by no means determines the shape of the light curve of the system in the quiescent state. It is evident from Fig. 2b that the form of the light curves of SS Cyg is mainly determined by ellipsoidal variations of the red dwarf. In this case, the classical hot-spot model can be used to interpret the light curve in order to determine the main parameters of the binary: component mass ratio, orbital inclination, and contributions of the disk and hot spot to the total luminosity. Model II can then be used to refine the disk and "spot" parameters. We analyzed the optical variability of SS Cyg using a version of our computer code [38] with a geometrically thick axisymmetric disk, written especially to interpret the light curves of dwarf novae [1].

Our analysis assumes that the close binary consists of a normal star (the red dwarf) and a degenerate star

Table 1. Mean *UBV* light curves of SS Cyg

Phase φ	$n_{V,B,U}$	Filter *V*		Filter *B*		Filter *U*	
		ΔV	σ_V	ΔB	σ_B	ΔU	σ_U
0.0129	84	0.0343	0.0087	0.0301	0.0112	0.0278	0.0139
0.0491	79	0.0555	0.0073	0.0496	0.0100	0.0511	0.0139
0.0997	74	0.0153	0.0099	0.0128	0.0131	−0.0013	0.0171
0.1511	66	0.0021	0.0102	0.0082	0.0128	0.0085	0.0184
0.2025	65	−0.0144	0.0069	−0.0132	0.0102	−0.0235	0.0159
0.2507	70	−0.0351	0.0090	−0.0389	0.0164	−0.0410	0.0208
0.3017	76	−0.0063	0.0077	0.0044	0.0105	−0.0098	0.0136
0.3509	73	0.0083	0.0089	0.0211	0.0113	0.0196	0.0137
0.4015	77	0.0362	0.0105	0.0434	0.0127	0.0250	0.0140
0.4493	73	0.0526	0.0088	0.0522	0.0115	0.0387	0.0135
0.4991	75	0.0535	0.0094	0.0646	0.0125	0.0390	0.0168
0.5490	75	0.0514	0.0080	0.0659	0.0109	0.0588	0.0129
0.5988	74	0.0101	0.0081	0.0211	0.0110	0.0271	0.0135
0.6485	74	−0.0417	0.0107	−0.0382	0.0144	−0.0400	0.0181
0.6988	77	−0.0832	0.0132	−0.0879	0.0174	−0.0765	0.0191
0.7499	65	−0.0782	0.0092	−0.0816	0.0132	−0.0577	0.0162
0.8007	76	−0.0497	0.0089	−0.0521	0.0114	−0.0305	0.0155
0.8508	82	−0.0342	0.0086	−0.0504	0.0114	−0.0275	0.0154
0.9003	80	−0.0130	0.0079	−0.0358	0.0100	−0.0162	0.0131
0.9493	82	0.0157	0.0080	−0.0008	0.0099	−0.0010	0.0125

Note: Orbital phase φ = 0.0 corresponds to superior conjunction of the white dwarf; *n* is the number of individual observations averaged to compute the normal point in question (it is the same for all filters *U*, *B*, and *V*).

(the white dwarf) emitting primarily in the visible part of the spectrum. We assume that the components rotate synchronously in circular orbits about the center of mass of the entire system. The red dwarf completely fills its Roche lobe, and the white dwarf is a sphere of radius R_{wd}. The emission spectra of both stars and of various parts of the disk are fitted by Planck laws. In our model, the white dwarf is surrounded by an optically thick accretion disk lying in the orbital plane, which is geometrically thin near the white-dwarf surface and geometrically thick at its outer edge. The disk can be heated by the optical emission of both binary components. The hot spot can also contribute to the total flux of the system at orbital phases when it is not eclipsed. The red dwarf can be partly heated by the hot spot. The disk is characterized by a nonuniform surface distribution of the temperature and, consequently, of the intensity.

Below, we give the input parameters required to compute the total magnitude of both components of the system at each of the orbital phases considered.

(1) We determine the input parameters of the red dwarf as follows. The shape of the star and the ratio of its size to the distance *a* between the component mass centers (in our program this distance is normalized to $a = 1$) are set by fixing the component mass ratio $q = M_{wd}/M_{rd}$ (where M_{wd} and M_{rd} are the masses of the red and white dwarfs, respectively) and the Roche-lobe filling factor of the star μ. We assumed $\mu = 1$ in our computations. To derive the star's luminosity in a selected filter, we used the effective temperature T_{eff} of the star in the absence of heating by the white dwarf and/or hot-spot and disk emission, the corresponding gravitational-darkening (β) and limb-darkening [$u(\lambda, T_j)$] coefficients (here, T_j is the temperature of a given area on the star's surface), and the coefficient for reprocessing of the white-dwarf and hot-spot radiation by the star's matter, κ_s. $\kappa_s = 1$ and $\beta = 0.25$ are usually adopted for cool stars. See [39] for a description of the computational technique used to infer the main geometrical parameters of the star.

(2) We assume the white dwarf to be a sphere with its center a distance *a* from the center of mass of the red dwarf. The luminosity of the white dwarf is determined by its radius R_{wd} in units of the distance ξ between the center of mass of the white dwarf and the inner Lagrangian point ($\xi = 1 - x_L$, where x_L is the *x* coordinate of the inner Lagrangian point in units of the orbital radius *a*) and also by the effective temperature T_{wd} and corresponding limb-darkening coefficient $u(\lambda, T)$. We

assume that heating of the white dwarf by the emission of the red dwarf is insignificant and that the temperature is constant throughout the surface. Therefore, $u(\lambda, T_{wd})$ is the same for all areas on the white-dwarf surface.

(3) To describe the disk shape, we use an *OXYZ* reference frame fixed to the white dwarf. The origin *O* coincides with the center of mass of the white dwarf, the *OZ* axis is perpendicular to the orbital plane, the *OX* axis is directed toward the center of mass of the red dwarf, and the *OY* axis lies in the orbital plane perpendicular to the *OX* axis. We specify the shape of the upper part of the disk $z > 0$ (Fig. 1) as follows. The inner disk is part of a paraboloid of revolution with paraboloid constant A_p, centered on the *OZ* axis ($z < 0$) such that the radius of the intersection of the paraboloid with the orbital plane is equal to R_{wd}, the radius of the white dwarf. The outer disk is part of an ellipsoid of revolution with semiaxes *b* (in the orbital plane) and *c* (perpendicular to the orbital plane). The intersection of the paraboloid of revolution and ellipsoid of revolution is the upper disk boundary, which determines the thickness of the outer disk edge. The shape of the lower part of the disk ($z < 0$) can be obtained by reflecting the "positive" part of the disk about the orbital plane.

The input parameters for the computation of the shape and luminosity of the disk are the disk radius R_d in units of the distance between the inner Lagrangian point L_1 and the center of mass of the white dwarf ξ and the paraboloid constant A_p in units of the disk radius R_d. We adopted the ellipsoid constants $b = R_d$ and $c/b = 0.5$. To estimate the degree of heating of the accretion disk by radiation from the white and red dwarfs, we used the usual coefficient κ_d for the reprocessing of optical emission by the disk matter, $\kappa_d = 1$. We allowed for the following factors when computing the flux of each disk area element visible at a given orbital phase. First, the temperature of an area element depends on the distance between its center and the white-dwarf surface. In this case, heating results from the reprocessing of gravitational energy into thermal energy of the accreting matter as it spirals down onto the white-dwarf surface. Spatial variations of the disk temperature are usually assumed to have the form $T_r = T_{wd}\left(\frac{R_{wd}}{r}\right)^{\alpha_g}$, where *r* is the distance between the centers of the white dwarf and the disk area element and $\alpha_g = 0.75$ to first approximation [40]. This approximation is based on the assumption that the radiation of each point in the disk has a blackbody spectrum. This is not the case in reality, and the observed distributions of the disk surface temperature imply that α_g can differ substantially from 0.75 [41]. The coefficient α_g is another parameter to be estimated. Further, each disk area element is heated by the optical radiation of the red dwarf. This heating is weak because the area elements can be screened from the red dwarf by both the disk edge and the white dwarf and also because the red dwarf is a rather cool star. The white-dwarf radiation is a more intense heating source for areas at the inner edge of the accretion disk. The total flux of the disk can be computed by summing the fluxes (allowing for the orbital inclination) from all uneclipsed area elements at both the inner and outer disk surfaces, taking into account the above factors.

The adopted classical hot-spot model assumes that the spot does not affect the inner (parabolic) disk regions. The input parameters determining the temperature, size, and location of the hot spot are f_{sp}, r_{sp}, and φ_{sp}. Here, $f_{sp} = \Delta T/T_d$ is the ratio of the disk temperature at the center of the hot-spot area to the temperature of the same disk area without any hot spot; f_{sp} is constant inside the spot, and r_{sp} is the spot radius (in units of the disk radius R_d). The spot is part of the ellipsoidal disk surface located inside the intersection of the disk surface with a sphere of radius r_{sp} centered at (x_{sp}, y_{sp}) with $z = 0$ at the outer disk surface. Finally, φ_{sp} is the orbital phase of the spot; i.e., the orbital phase when the line of sight is parallel to the vertical (with respect to the orbital plane) symmetry plane of the spot. The adopted parameters of the hot bulge spot in model II are given below in Section 8.

The hot-spot radiation not only contributes to the total flux of the system at orbital phases when the spot is visible but also heats the visible area of the red dwarf at orbital phases near $\varphi \sim 0.75$ (i.e., when the hot spot becomes visible), making it hotter than the opposite side of the star. If the heating coefficients are $k_{sp} = L_{sp}/L_{opt} \sim 0.5$–1, this effect makes the contribution of the red-dwarf radiation to the binary light curve asymmetric (relative to the line connecting the two components; see Fig. 2b). Here, L_{sp} and L_{opt} are the bolometric fluxes of the hot spot and red star, respectively. L_{opt} is computed by integrating over the surface of the red star flux elements not heated by other components of the system, and k_{sp} is a parameter of the problem.

Finally, the photometric amplitude and visibility conditions for area elements of the system components depend strongly on the orbital inclination *i* (the angle between the line of sight and the perpendicular to the orbital plane). Thus, a total of 12 parameters—*i*, *q*, T_{eff}, R_{wd}, T_{wd}, R_d, A_p, α_g, f_{sp}, r_{sp}, φ_{sp}, and k_{sp}—determine the light curve for a classical hot-spot model of the cataclysmic binary.

6. METHODS FOR DETERMINING THE PARAMETERS OF SS CYG

To assess how well a synthetic light curve fit the observed light curve, we computed the residual function

$$\chi^2 = \sum_{j=1}^{n} \frac{(m_j^{theor} - m_j^{obs})^2}{\sigma_j^2}, \qquad (1)$$

where m_j^{theor} and m_j^{obs} are the theoretical and observed total magnitudes at the *j*th orbital phase, σ_j^2 is the vari-

ance of the observed magnitudes at the jth orbital phase, and n is the number of mean points in the light curve. To determine a set of parameters yielding a theoretical curve that satisfactorily fits the observed light curve, we used the Nelder–Mead method [42] and a "genetic" [43] optimization algorithm.

In the Nelder–Mead method (also called the simplex method), a function of N independent variables is minimized using $N + 1$ deformable simplexes in an N-dimensional vector space E^N of the unknown parameters. The vertex of a simplex, or a vector $\mathbf{X}$, is a set of N parameters describing the unknown function in the space E^N. The following procedure is then used to minimize the target function. First, $N + 1$ values of the target function $F(\mathbf{X})$ are computed for $N + 1$ initial vectors $\mathbf{X} = \mathbf{X}(j)$, $j = 1, \ldots, N$. The point in the space E^N where the function $F(\mathbf{X})$ is largest is projected through the center of mass of the remaining points. The refined (lower) function values are found via a series of steps in which "better" points are substituted for the point with the largest $F(\mathbf{X})$ until the minimum of $F(\mathbf{X})$ is found. The drawback of this (and many other) search algorithms is that they require *a priori* knowledge that the target function has only one minimum in the domain considered. Since the parameter domain under study usually contains several local minima, the global minimization procedure must be restarted with several initial vectors $\mathbf{X}(j)$.

The genetic algorithm suggested and analyzed by Charbonneau [43] allows determination of the global extremum of a function $F(\mathbf{X})$ in the specified parameter domain as follows. Suppose we have a function of N variables $F(\mathbf{X})$. The variables, as in the Nelder–Mead method, are parameters $\mathbf{X}(N)$ of the theoretical light curve. We specify limits for the unknown parameters and normalize them so that they lie within the interval [0, 1]. The problem is to find the extremum of the function $F(\mathbf{X}) = F$, where the residual function χ^2 is computed from formula (1).

The genetic algorithm includes the following series of steps.

(1) We choose N_{gr} (N_{gr} = 100–200) random vectors $\mathbf{X}(N)$ in the parameter domain and compute the function $F(\mathbf{X}(N))$ at the corresponding points. N_{gr} is referred to as the size of the initial population.

(2) For each random vector $\mathbf{X}_i$, we combine a "gene"—a sequence of N_{gen} (N_{gen} = 6–8) significant digits of each vector component $\mathbf{X}_i$, $i = 1, \ldots, N$. This procedure is referred to as gene encoding.

(3) We multiply the gene; i.e., we randomly select pairs among the population objects, exchange genes in each such pair (the so-called crossover procedure), and substitute a random number for a randomly selected gene element (a number in the interval [0, 1]). This procedure is referred to as mutation.

(4) We decode the gene; i.e., we reconstruct a new vector $\mathbf{X}_i$, $i = 1, N$ from the resulting sequence of digits.

(5) We then compute the target function $F(\mathbf{X})$ for each of the newly obtained vectors $\mathbf{X}$ for the new population and substitute the new population for the old one. The population breeding process gives priority to those population members (i.e., vectors $\mathbf{X}$) that yield the highest values of the function $F(\mathbf{X})$.

This genetic algorithm makes it possible to optimize functions with several extreme in the parameter domain considered. Our optimization procedure first uses the genetic algorithm to determine the parameter domain containing the highest extremum and then applies the Nelder–Mead algorithm to identify the optimum $\mathbf{X}(N)$ in this domain.

7. ANALYSIS OF *UBV* LIGHT CURVES AND THE PARAMETER DOMAIN OF SS CYG

To infer the parameters of SS Cyg, we analyzed the observed light curves in each filter separately, allowing each parameter to vary over a fairly wide range. We fixed some parameters, since, due to its low orbital inclination, SS Cyg exhibits neither white-dwarf nor accretion-disk eclipses.

We estimated the effective temperature of the red dwarf from its spectral type. According to [30], the red dwarf is a K5 V star. Echevarria *et al.* [29] found the star to have a spectral type of K2 V–M IV, based on its absorption spectrum. The theoretical computations [44] suggest the spectral type of SS Cyg is K4 V. We computed the parameters of the binary assuming that the effective temperature of the red dwarf was 4550 K, which corresponds to spectral types K4–K5 V [45]. The corresponding gravity-darkening index is $\beta = 0.25$, and the limb-darkening coefficients are $u(\lambda, T_s) \simeq 0.7$ and ~0.88–0.93 for the V and BU filters, respectively, depending on the location of an area element with temperature T_s on the star's surface.

The thickness of the outer edge of the disk at orbital inclinations $i < 60°$, when the white dwarf is substantially out of eclipse, has virtually no effect on the minimization of the functional. The thickness of the outer disk edge decreases with A_p, decreasing the maximum possible size of the hot spot. A preliminary run showed that the residual function remained virtually unchanged in the A_p intervals ~1.1–3.0, ~1.6–1.9, and ~1.3–2.5 for the U, B, and V filters, respectively. We adopted $A_p = 1.9$ in our computations.

If ellipsoidal variations are the main source of variability, the orbital inclination i and component mass ratio q are the main parameters determining the appearance of the light curve. The light-curve shape also depends on k_{sp}, which determines the hot-spot radiation. The reprocessing of this radiation by the matter of the companion results in an asymmetric temperature distribution on the surface of the red dwarf, increasing this star's flux at one of the quadratures. Finally, the shape of the light curve can, to some degree, depend on variations of the hot-spot flux with orbital phase. In our model, the spot is located at the outer edge of the disk. Although the contribution of the outer disk surface to

Table 2. Parameters of SS Cyg from the *U*, *B*, and *V* light-curve solutions

Parameter	Filter *U*	Filter *B*	Filter *V*
$q = M_{wd}/M_{rd}$	1.81 ± 0.72	1.56 ± 0.39	1.67 ± 0.37
i, deg	53.4 ± 2.9	52.6 ± 1.5	51.7 ± 1.7
T_{eff}, K		4550 (fixed)	
R_{wd}/ξ	0.0113 ± 0.0014	0.0109 ± 0.0009	0.0122 ± 0.0010
R_{wd}/a	0.0062 ± 0.0008	0.0059 ± 0.0005	0.0066 ± 0.0006
T_{wd}, K	25340 ± 1900	25390 ± 1110	26820 ± 1250
R_d/ξ	0.44 ± 0.27	0.53 ± 0.11	0.51 ± 0.09
R_d/a	0.22 ± 0.15	0.29 ± 0.06	0.28 ± 0.06
α_g	0.64 ± 0.03	0.51 ± 0.02	0.54 ± 0.02
A_p		1.9 (fixed)	
$2h/a$		0.07–0.12	
$k_{sp} = L_{sp}/L_{opt}$	0.35 ± 0.25	0.51 ± 0.19	0.81 ± 0.17
f_{sp}	2.35 ± 0.25	2.14 ± 0.14	2.08 ± 0.24
r_{sp}/R_d	0.034 ± 0.007	0.038 ± 0.006	0.059 ± 0.004
r_{sp}/a	0.008 ± 0.006	0.011 ± 0.004	0.016 ± 0.004
φ_{sp}	0.819 ± 0.003	0.819 ± 0.003	0.813 ± 0.001
Azimuth, deg	65.2 ± 1.1	65.2 ± 1.1	67.3 ± 0.4

Note: ξ is the distance between the inner Lagrangian point and the center of mass of the white dwarf ($\xi = 0.56a$ for $q = 1.65$). $2h/a$ is the thickness of the outer disk edge in units of the separation between the components. A_p for the paraboloidal disk section is in units of $\sqrt{R_d}$. The dimensionless parameter $f_{sp} = \Delta T/T_d$ is equal to the ratio of the temperature of the disk matter at the center of the area considered to the temperature of the same disk area in the absence of hot spots.

the total flux is small compared to those of inner-disk regions at $i < 60°$, eclipses of the hot spot at the outer disk surface by the red dwarf or disk edge can affect the light curve's shape. The contribution of the white dwarf to the total flux, like that of the disk, is independent of orbital phase, since neither component is eclipsed. However, the corresponding contributions cannot be simply fixed, since the temperature of the white dwarf determines the heating of both the red dwarf and accretion disk. The disk temperature, radius, and radial temperature distribution, in turn, determine, through the parameter f_{sp}, the temperature of the hot spot and, consequently, the total flux in the wavelength interval considered. The theoretical dwarf-nova light curve for SS Cyg is, thus, determined by ten parameters (q, i, k_{sp}, f_{sp}, r_{sp}, φ_{sp}, R_{wd}, T_{wd}, R_d, and α_g); however, some of these parameters—namely, the temperature ($T_{wd} \sim$ 23000–27000 K) and radius ($R_{wd} \sim 0.009\xi$–0.013ξ) of the white dwarf and the disk radius ($R_d \sim 0.4\xi$–0.6ξ)—can be appreciably restricted.

Various researchers have suggested discrepant hypotheses in connection with the component mass ratio. According to Cowley et al. [46], q is close to 1, whereas Echevarria *et al.* [29] found the white dwarf to be more massive and suggested q values as high as 1.65. Therefore, we allowed q to vary over a wide range when minimizing the target function: q = 0.5–2.5. We allowed other parameters to vary in the following intervals: 5–85° for the orbital inclination, 0–10 for the parameter k_{sp}, 0.1–0.75 for α_g, $(0.01–0.5)R_d$ for the hot-spot radius, 0–90° for the hot-spot azimuth relative to the line connecting the components (this corresponds to orbital phases $\varphi_{sp} \sim$ 0.75–1.0), and $f_{sp} \sim$ 0–10 for the parameter characterizing the temperature enhancement in the disk areas inside the hot spot.

Table 2 gives the binary parameters obtained from the separate light-curve solutions in each filter for the classical model. We used a χ^2 criterion to determine the confidence intervals for the parameters of SS Cyg. In our case, the critical significance level is $\chi^2_{\alpha, N} = \chi^2_{0.03, 10} = 20.2$. Here, $\alpha = 0.03$ and the number of degrees of freedom is $N = n - k$, where n is the number of normal points ($n = 20$) and k is the number of independent variables in the minimization (k =10). To determine the confidence interval for each parameter, we computed χ^2 at a number of points throughout the corresponding domain, with other parameters fixed at their optimum values. Figure 3 plots χ^2 as functions of some of the parameters

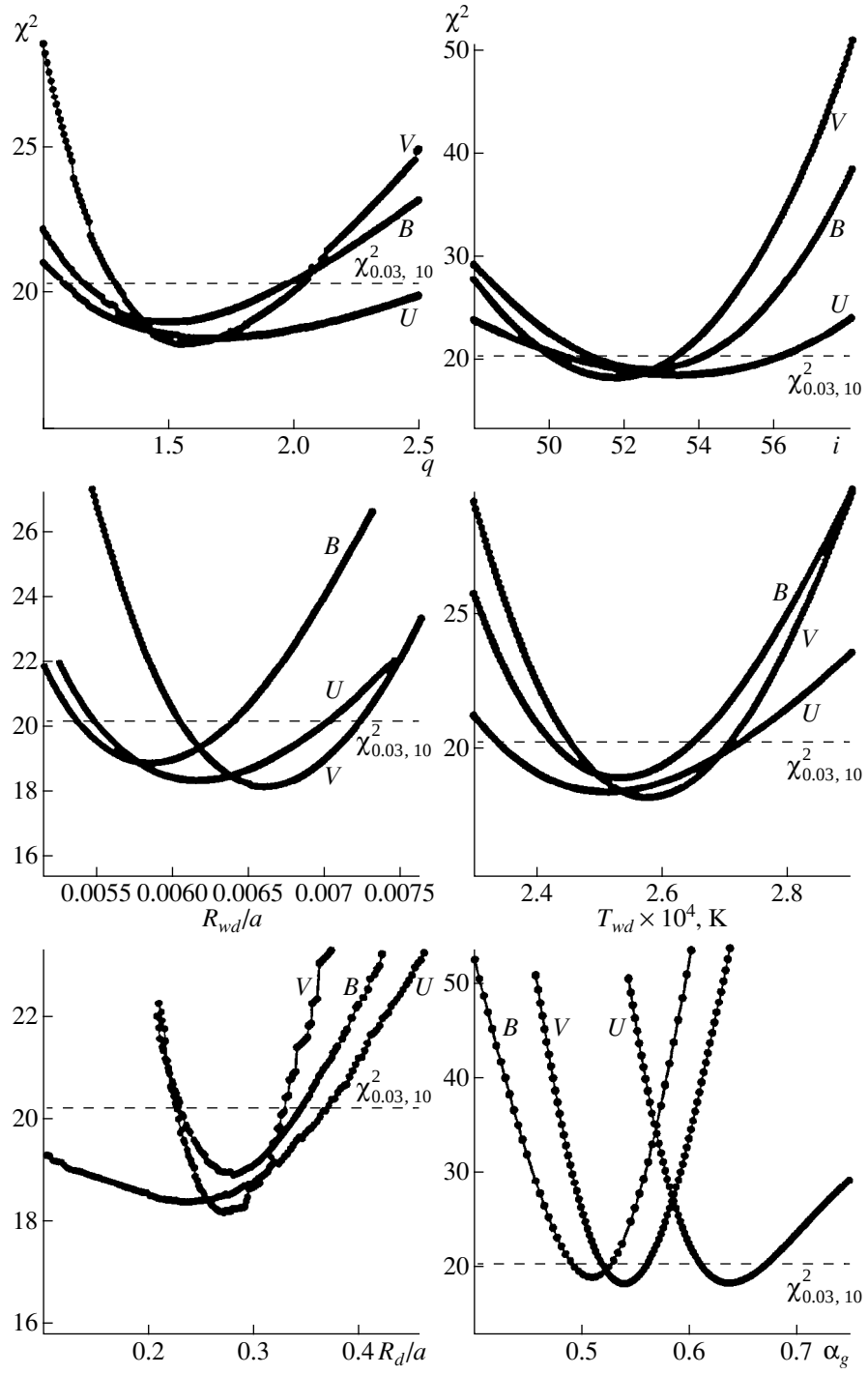

Fig. 3. Residual χ^2 as a function of selected parameters of SS Cyg (q, i, R_{wd}, T_{wd}, R_d, and α_g) for our binary light-curve solutions. The dashed curve shows the critical significance level $\chi^2_{crit} = \chi^2_{0.03,\,10} = 20.2$.

(q, i, R_{wd}, T_{wd}, R_d, and α_g). The dashed line shows the critical significance level $\chi^2_{crit} = \chi^2_{0.03,\,10} = 20.2$.

Our analysis of the light curves of SS Cyg supports the conclusion of Echevarria *et al.* [29] that the red star is less massive than the white dwarf; i.e., $q = M_{wd}/M_{rd} > 1$. q can vary over a fairly wide range: $q \sim 1.1$–2.5 in the U filter; $q \sim 1.2$–1.95 in the B filter, and $q \sim 1.3$–2.0 in the V filter. The common interval is $q \sim 1.30$–1.95, with a minimum at $q \sim 1.56$. Although the confidence interval for the

component mass ratio q is fairly broad at a significance level $\alpha = 0.03$, other parameters can be constrained to rather narrow intervals, e.g., the orbital inclination $i = 51$–$54°$ (Fig. 3).

The inferred temperature of the white-dwarf component is typical for this class of stars, $T_{wd} = 24500$–27000 K. As noted above, the form of the light curve depends on the temperature of the hot star mainly through the degree of heating of the accretion-disk surface; in other words, T_{wd} directly determines the contribution of the accretion disk to the total flux [1]. The photometric data for all filters yield consistent (within the errors) white-dwarf radii, with an average value of $R_{wd} \sim 0.0062a$. The contribution of the white dwarf proper to the total flux is rather small (Fig. 4a, curve *2*) and does not exceed 3%.

To further constrain the domain of q values allowed by the solution, both spectroscopic data for the binary and theoretical studies of white dwarfs are needed. Kepler's third law can be used to determine the distance between the stars, and the Hamada–Salpeter mass–radius relation [47] for helium white dwarfs can be used to estimate the radius of the white dwarf in SS Cyg R_{wd} in units of the solar radius for a number of adopted mass values M_{wd}, making it possible to infer other parameters of the binary, such as the mass of the secondary M_{rd}, the radial velocities of both stars, etc. Figure 5a shows the Hamada–Salpeter [47] mass–radius relation for white dwarfs obtained by solving the equation of state for He^4 (the *H–S* curve).

Our light-curve solutions yielded R_{wd} values in units of the separation between the component stars a that depend on the component masses. To transform R_{wd}/a into solar radii, we determine a from Kepler's third law written in the form

$$\frac{a}{R_\odot} = 4.2137\sqrt[3]{P^2 M_{wd}(1 + 1/q)}, \qquad (2)$$

where P is the orbital period of the binary in days, M_{wd} the mass of the white dwarf in units of the solar mass, and q the component mass ratio as determined above. Curves *1*, *2*, and *3* in Fig. 5a show the mass–radius relations for the white dwarf for $q = 1.30$ (curve *1*), 1.56 (curve *2*), and 1.95 (curve *3*), both for the minimum ($R_{wd} \sim 0.00606a$, solid lines) and maximum ($R_{wd} \sim 0.00635a$, dashed lines) white-dwarf radii. The corresponding relations for $R_{wd} \sim 0.00620a$ lie between the two curves shown in the figure. The theoretical $M_{wd} - R_{wd}$ relation crosses the relations obtained for $R_{wd} \sim (0.00606, 0.00620, 0.00635)a$ and $q = 1.30$–1.95 in the $M_{wd} \sim (0.63$–$0.71)M_\odot$ and $R_{wd} \sim (0.0111$–$0.0119)R_\odot$ mass and radius intervals, respectively, implying a red-dwarf mass of $M_{rd} \sim (0.34$–$0.52)M_\odot$.

Spectroscopic data for the red-dwarf component in SS Cyg allows us to further constrain the component masses. According to [44], the semi-amplitude of the radial-velocity curve of the red component is $K_v \sim 146$–162 km/s, and the corresponding mass function is $f_2 \sim (0.104$–$0.121)M_\odot$. The dashed lines in Fig. 5b show the relations between the white-dwarf mass M_{wd} and the component mass ratio q computed for three semi-amplitudes K_v of the radial-velocity curve for the adopted orbital inclination of $i = 52°$. The solid lines in the figure correspond to intersections between the Hamada–Salpeter relations and curves *1*, *2*, and *3* in Fig. 5a computed for the corresponding white-dwarf radii R_{wd}/a. The intersections of the curves $M_{wd}(q, K_v)$ with the relations $M_{wd}(q, R_{wd}/a)$ lie in the interval $q \simeq 1.12$–1.60. In view of the $\alpha = 0.03$ confidence interval, whose boundaries are shown by the vertical dotted lines, the component mass ratio q can be further constrained to the range $q \simeq 1.3$–1.6, implying

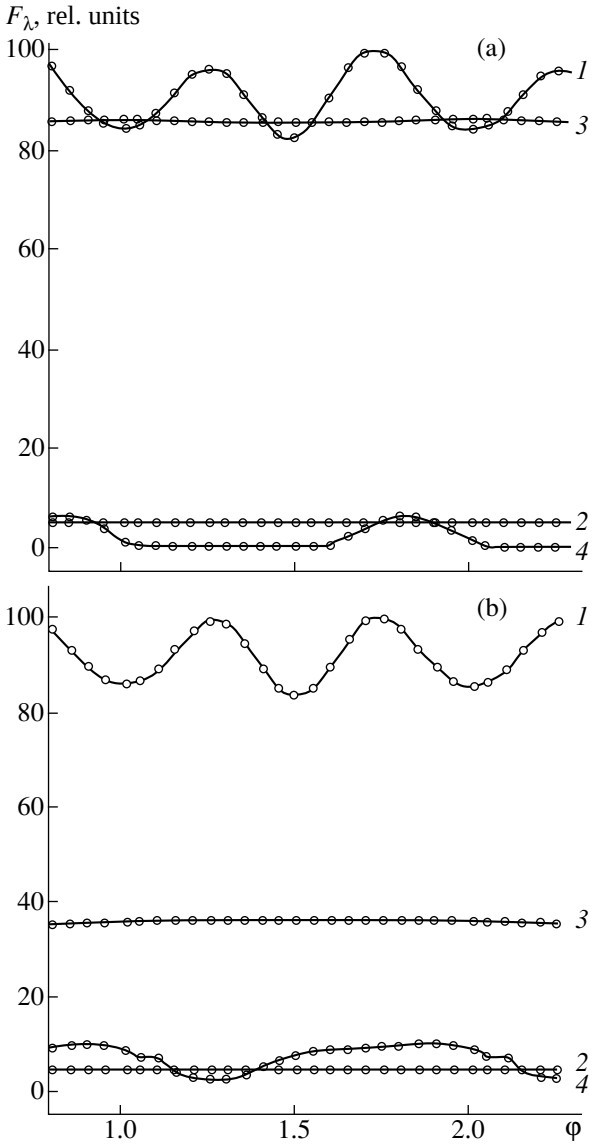

Fig. 4. Contribution of various components to the total flux of the binary as a function of the V orbital phase. (a) The classical hot-spot model I and (b) the nonclassical hot-spot model II. Curves *1*, *2*, *3*, and *4* correspond to the red dwarf, white dwarf, accretion disk, and hot spot, respectively.

Table 3. Physical parameters of the dwarf nova SS Cyg

Parameters of the system as a whole	
$q = M_{wd}/M_{rd} \sim 1.3$–$1.6$	
$i = 52° \pm 1°$	
$a \sim (1.82$–$1.89)R_\odot$	
Red dwarf	Accretion disk
$M_{rd} \sim (0.41$–$0.51)M_\odot$	$R_d \sim 0.44\xi \sim 0.22a$ (U)
$R_{rd} \sim (0.35$–$0.37)\ a \sim (0.63$–$0.69)R_\odot$	$R_d \sim 0.50\xi \sim 0.28a$ (B, V)
$T_{eff} = 4550$ K (fixed)	$2h \sim (0.07$–$0.12)a$
Sp K3–K5 V [30, 44]	$T_d \sim 3000$–3200 K (outer edge)
$L_{\rm bol} \simeq (6.5 \pm 0.6) \times 10^{32}$ erg/s	$T_d \sim 25\,000$ K (inner region)
White dwarf	Hot spot
$M_{wd} \sim (0.63$–$0.69)M_\odot$	$R_{sp} \sim (0.01$–$0.016)a$
$R_{wd} \sim (0.0110$–$0.0120)R_\odot$	$T_{sp} \simeq 6000$–8300 K
$T_{wd} \sim 24\,500$–$26\,200$ K	$L_{sp} \simeq (2$–$6) \times 10^{32}$ erg/s

Note: T_d and T_{sp} are the color temperatures of the disk and hot spot.

component masses of $M_{wd} \sim (0.63$–$0.69)M_\odot$ and $M_{rd} \sim (0.41$–$0.51)M_\odot$. The mean radius of the red dwarf for $q \sim 1.3$–1.6 is $R_{rd} \sim (0.35$–$0.37)a \sim (0.63$–$0.69)R_\odot$ (see Table 3).

The photometric radius of the accretion disk in SS Cyg is $R_d \sim (0.42$–$0.64)\xi \sim (0.22$–$0.35)a \simeq (3.7 \pm 0.9) \times 10^{10}$ cm, consistent within the quoted errors with the estimate reported in [48], $R_d \sim 2.8 \times 10^{10}$ cm. The thickness of the outer edge of the accretion disk is $2h \sim (0.07$–$0.12)a$ (Fig. 1 and Table 2). Here, h is the distance between the orbital plane and the upper side of the disk. The temperature at the outer surface of the disk is ~3000–3200 K (outside the hot spot). We assumed the temperature of the inner regions of the disk was equal to that of the white dwarf, 24000–27000 K. The disk contributes substantially (~47%) to the total flux in the V filter during the quiescent phase of the binary and its share is comparable to the mean flux from the red dwarf (~48%). The flux from the white dwarf is an order of magnitude lower (~3%). As expected, the hot-spot flux in the classical model is fairly low and does not exceed ~3% of the total optical flux at orbital phases $\varphi \sim 0.8$. Figure 4a compares the V fluxes of the two components in SS Cyg as a function of the orbital phase. The fluxes should be converted into common units as $f_\lambda = F_\lambda a^2 \times 10^{-12}$ erg s^{-1} cm^{-3}, where a is the separation between the two components in cm and F_λ is the flux show in the figure in arbitrary units. The disk contributions in the B and U filters are somewhat higher, ~54 and ~49% of the total flux, respectively.

Our computations support the conclusion of Djurasevic [41] that the coefficient α_g deviates from 0.75. For the B and V filters, $\alpha_g \sim 0.5$–0.54, and it is somewhat higher for the U filter, $\alpha_g \sim 0.64$. Figure 6 shows the radial temperature profile of the accretion disk (without allowance for heating of the disk surface by the radiation of the white dwarf) for $\alpha_g = 0.54$ and a similar profile $T_d(r)$ for $\alpha_g = 0.75$. A lower value for α_g results in smoother temperature variations in the disk from its inner to its outer regions, and, consequently, in a higher disk luminosity.

The optical flux of the hot spot is fairly low (Fig. 4) and depends only slightly on the component mass ratio. The hot spot contributes ~3, ~5, and ~3% to the total fluxes in the V, B, and U filters, respectively. The mean effective temperature of the gas at the hot-spot center is a factor of 2–2.6 higher than in the adjacent regions, $T_{sp} \sim 6000$–8300 K. The spot is small, and its diameter $2h$, $D_{sp} = 2r_{sp} \sim (0.02$–$0.03)a$ is much less than the thickness of the outer disk edge $2h$ (Table 3). The bolometric flux from the hot spot from an independent analysis of the UBV light curves of the binary is ~35–80% of the bolometric luminosity of the red dwarf. The adopted bolometric luminosity of the star $L_{\rm bol} = 4\pi\sigma T^4 R_{rd}^2 = (6.5 \pm 0.6) \times 10^{32}$ erg/s thus implies a hot-spot bolometric luminosity of $L_{sp} \sim (2$–$6) \times 10^{32}$ erg/s. If the radiation of a hot spot with the indicated size were purely thermal, the spot must have a temperature of 7500–21800 K to produce a flux of $L_{sp} \sim (2$–$6) \times 10^{32}$ erg/s.

8. THE NONCLASSICAL HOT-SPOT MODEL

In this section, we present the parameters of SS Cyg inferred using model II, which assumes that the hot spot is located outside the accretion disk. In this "nonclassical" model, the interaction between the matter flowing from the red dwarf and the gaseous envelope surrounding the white dwarf produces an extended shock along the edge of the stream, which has the same

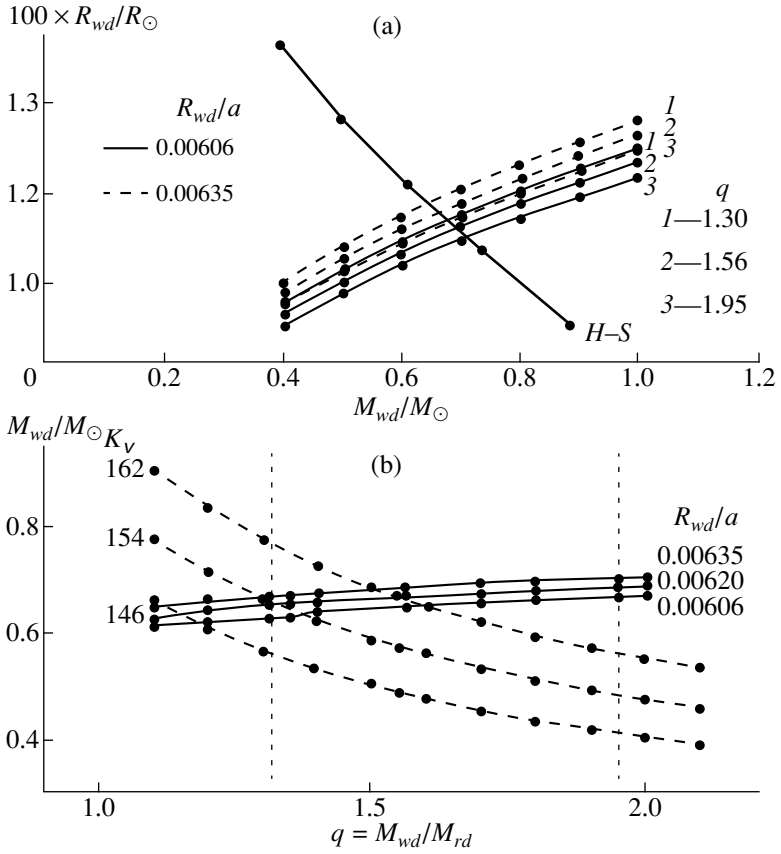

Fig. 5. Estimating the white-dwarf mass. (a) Theoretical (*H–S*) mass–radius relation for helium white dwarfs [47]; the thin lines show the Keplerian $R_{wd}(M_{wd})$ relation for component mass ratios q = 1.30 (*1*); 1.56 (*2*), and 1.95 (*3*). The thin solid and dashed lines correspond to $R_{wd} = 0.00606a$ and $R_{wd} = 0.00635a$, respectively. (b) M_{wd} as a function of mass ratio q for three semi-amplitudes K_v of the radial-velocity curve and $i = 52°$ (dashed lines); the solid lines connect the intersections of the *H–S* relation with curves *1*, *2*, and *3* in the upper panel computed for various q and $R_{wd} = 0.00606a$, $0.00620a$, and $0.00635a$; the vertical dotted lines show the allowable range of q at $\alpha = 0.03$ confidence interval from the solution of SS Cyg light curves.

observational manifestations as a hot spot in the disk. We parametrize the nonclassical hot spot in model II as a section of an ellipsoid of revolution (Fig. 1b) centered on the orbital plane on the lateral edge of the disk surface. One semiaxis (a_b) of this ellipsoid lies in the orbital plane and the other (c_b) is perpendicular to it. We will refer to this formation as a bulge. We assume that the bulge surface-brightness distribution can be far from uniform, since the optical depth of such a shock at the edge of the gaseous stream can be strongly nonisotropic. The adopted ellipsoidal bulge shape does not match exactly the shape of the shock at the edge of the gaseous stream. However, placing the bulge outside the accretion disk enables us to analyze how adopting the model of Bisikalo *et al.* [9, 10] for the gas-dynamic mass outflow in cataclysmic variables affects the parameters of the accretion-disk and hot-spot in the SS Cyg system.

As in model I, the location of the hot spot in model II is determined by the orbital phase of the bulge φ_{sp}, and the spot luminosity is determined by the coefficients f_{stream} and f_{back}. These parameters have the same meaning as f_{sp} in the classic spot model: They determine the temperature enhancement for the areas located at the side of the bulge facing the stream (φ_{stream}) and facing away from the stream (φ_{back}).

We analyzed the *V* light curve of SS Cyg to determine the binary parameters for model II. We assumed that the parameters determining the contributions of the red and white dwarfs to the total flux lie in the intervals implied by the model I light-curve solution (Table 2): T_{eff} = 4550 K, A_p = 1.9, T_{wd} = 26000 K, R_{wd}/ξ = 0.0100–0.0132, q = 1.3–1.65, and i = 50°–54°. We made a fit for the last three parameters, reducing the number of unknown quantities to eight: the radius of the accretion disk R_d, coefficient α_g, bulge semiaxes a_b and c_b, coefficients determining the bulge luminosity f_{stream} and f_{back}, orbital phase of the bulge center φ_{sp}, and the hot radiation from the shock region k_{sp}. The critical significance level for $\alpha = 0.03$ and $N = n - k$ degrees of freedom (here, n is the number of normal points, n = 20, and k is the number of unknowns, k = 8) is $\chi^2_{0.03,\,12} = 23.6$.

The χ^2 function was minimized at $\chi^2 = 17.67$ by the following set of model parameters (the $\alpha = 0.03$ confidence limits for each parameter are given in parentheses):

$$q = 1.5\ (1.45–1.65),$$

$$i = 54°.1\ (50°–54°.5),$$

$$R_{wd}/\xi = 0.0113\ (0.0109–0.0122),$$

$$R_d = 0.45\xi = 0.244a\ (0.44\xi–0.52\xi),$$

$$\alpha_g = 0.64\ (0.62–0.70),$$

$$a_b = 0.096a\ (0.045a–0.105a),$$

$$c_b = 0.030a\ (0.022a–0.042a),$$

$$\varphi_{sp} = 0.761\ (0.75–0.78),$$

$$k_{sp} = 0.33\ (0.10–1.0),$$

$$f_{\text{stream}} = 1.24\ (1.1–1.8),$$

$$f_{\text{back}} = 1.44\ (1.3–2.3).$$

The confidence intervals for the disk radius R_d and the parameter k_{sp} overlap with the corresponding intervals inferred for the classical hot-spot model (see Table 2, results of *V* light-curve solution). Compared to model I, the value of α_g (which determines the heating of the disk via conversion of gravitational energy into thermal energy of the accreting matter as it spirals down onto the white-dwarf surface) inferred using model II is closer to the theoretical value $\alpha_g = 0.75$ [40] obtained assuming each point of the disk radiates as a blackbody. The azimuth of the bulge center is 81° (79°–86°.4), which exceeds the hot-spot central azimuth by almost 10°. The angular size of the hot formation increased from ~7° for the spot in model I to ~25° for the bulge in model II, while the color temperature of the bulge is lower than that of the spot (see above). The large bulge size is in qualitative agreement with the existence of an extended energy source at the edge of the gaseous stream, although our model does not fully match the accretion pattern suggested by Bisikalo *et al.* [9, 10].

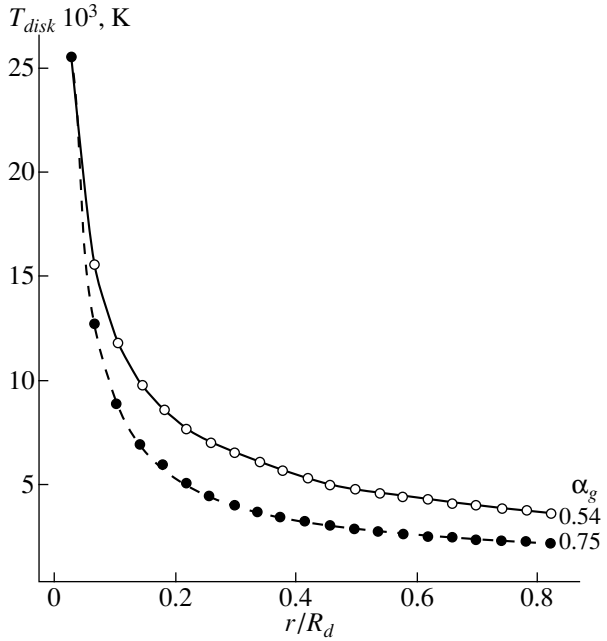

Fig. 6. Disk temperature as a function of distance from the white-dwarf surface for two values of the coefficient α_g.

Figure 4b shows the contributions of the various binary components to the total luminosity as functions of the orbital phase for the model-II *V* light-curve. Curves *1*, *2*, *3*, and *4* correspond to the red dwarf, white dwarf, accretion disk, and bulge, respectively. Comparison with Fig. 4a shows that the most substantial difference between the nonclassical and classical models is that the former implies a much higher contribution of the bulge to the total flux. With an orbital inclination $i \sim 54°$, the bulge is visible at all orbital phases. The bulge's contribution to the total flux is a factor of three to four higher at $\varphi \sim 0.4–1.1$ than at $\varphi \sim 0.15–0.35$, and is almost 7.4% at its maximum. Note that the hot spot in model I contributes to the total flux only at orbital phases $\varphi \sim 0.7–0.9$. At the same time, model II implies a substantially lower (~27% in the *V* filter) contribution from the disk and a higher (up to ~62%) contribution from the red dwarf, while leaving the white-dwarf contribution virtually unchanged (~3.6%).

9. CONCLUSION

Our analysis of mean *UBV* light curves of SS Cyg in the quiescent state has shown that their shape and amplitude can satisfactorily be explained by a close binary model with a red dwarf that fills completely its Roche lobe and a white dwarf ($T_{wd} \sim 25000$ K) with a radius $R_{wd} \sim 0.0062a = (7.7–8.4) \times 10^8$ cm surrounded by an optically and geometrically thick accretion disk of radius $R_d \sim 0.22a–0.35a = (2.8–4.6) \times 10^{10}$ cm. Our analysis yielded the following results.

(1) The masses of the binary components are $M_{rd} \sim (0.41–0.51)M_\odot$ and $M_{wd} \sim (0.63–0.69)M_\odot$. These values agree well with those derived from the spectroscopic observations of [29] ($M_{rd} = 0.47M_\odot$ and $M_{wd} = 0.77M_\odot$), though they are slightly higher than our previous qualitative estimates [35] based on the assumption that the observed photometric variability is due to partial mutual eclipses of the binary components. Our new results are substantially lower than the estimates obtained earlier by other authors, e.g., $M_{rd} = 0.65M_\odot$ and $M_{wd} = (0.98–1.20)M_\odot$ [44].

(2) Earlier analyses of radial-velocity data for SS Cyg performed by various researchers yielded two different component mass ratios: $q = M_{wd}/M_{rd} \sim 1.6$ [18] and $q \sim 1.0$ [46]. We tried a wide range of possible $q \simeq 0.05–2.5$ values, and our analysis enabled us to distinguish between these two values. The observed light curves were best fitted by a model with $q \sim 1.45–1.5$

(Figs. 3 and 5), corroborating the conclusion of Echevarria *et al.* [29] that the mass of the white dwarf in SS Cyg is a factor of 1.5 lower than the mass of the red star.

(3) Our analysis of photometric data for SS Cyg in the quiescent state enabled accurate determination of the orbital inclination of the system, $i \sim 52°$–$54°$. The orbital inclination had earlier been estimated to be 35–40° based on the absence of eclipses in SS Cyg [29, 44] or the known luminosity class (main-sequence) of the red dwarf [49]. At the same time, the dependence of the light variations of SS Cyg in the quiescent state on orbital phase, which amount to $0^m.2$ [34–36], favors larger orbital inclination, $i > 50°$. We demonstrated that the optical variability of the system is due primarily to ellipsoidal variations of the red dwarf. Eclipses of the hot spot by the disk edge contribute negligibly to the total light curve.

(4) We have estimated the contribution of the accretion disk to the total binary flux in the quiescent state. In a classical model, the disk contributes ~47–49% and ~54% of the total flux in the *VU* and *B* filters, respectively. The contribution of the hot spot to the total optical flux does not exceed 3–5%. In nonclassical bulge-spot models, the disk contributes ~26% to the total flux; the bulge contributes nearly 8%, and its radiation can be observed at all orbital phases for the inferred orbital inclination.

(5) Our nonclassical hot-spot model (model II) for the light curves of SS Cyg yielded the same values for the main parameters of the individual stellar components (mass ratio, orbital inclination, effective temperature, and disk radius) as the classical hot-spot model (model I). The azimuth of the bulge center in model II is 8°–10° larger than that of the hot-spot center in model I. The angular size of the bulge is rather large (~25°), which is qualitatively consistent with the presence of an extended energy source at the edge of the gaseous stream [9, 10].

ACKNOWLEDGMENTS

We thank A. M. Cherepashchuk for his discussions of the results of this work. This work was supported by the Russian Foundation for Basic Research (project code 99-02-17589), the Program for the Support of Leading Scientific Schools (grant no. 96-15-96489), the State Science and Technology Program "Astronomy: Fundamental Space Research" (grant nos. 1.4.2.1 and 1.4.2.2), and the Universities of Russia Program (grant no. 5556).

REFERENCES

1. T. S. Khruzina, Astron. Zh. **75**, 209 (1998).
2. S. Shore, M. Livio, and E. P. J. Van den Heuvel, Interacting Binaries (Springer, Berlin–Budapest, 1994).
3. M. Hack, *Cataclysmic Variables and Related Objects. P. 1* (U.S. Gov., Washington, 1993).
4. J. Smak, Acta Astron. **20**, 312 (1970).
5. A. N. Matvienko, A. M. Cherepashchuk, and A. G. Yagola, Astron. Zh. **65**, 1006 (1988).
6. K. Horne, Mon. Not. R. Astron. Soc. **213**, 129 (1985).
7. K. Horne and M. C. Cook, Mon. Not. R. Astron. Soc. **214**, 307 (1985).
8. K. Horne and T. R. March, Mon. Not. R. Astron. Soc. **218**, 761 (1986).
9. D. V. Bisikalo, A. A. Boyarchuk, O. A. Kuznetsov, *et al.*, Astron. Zh. **74**, 880 (1997).
10. D. V. Bisikalo, A. A. Boyarchuk, O. A. Kuznetsov, *et al.*, Astron. Zh. **74**, 889 (1997).
11. D. V. Bisikalo, A. A. Boyarchuk, O. A. Kuznetsov, *et al.*, Astron. Zh. **75**, 40 (1998).
12. G. T. Bath and J. E. Pringle, Mon. Not. R. Astron. Soc. **194**, 967 (1981).
13. Y. Osaki, Publ. Astron. Soc. Jpn. **26**, 429 (1974).
14. F. Meyer and E. Meyer-Hofmeister, Astron. Astrophys. **104**, 10 (1981).
15. J. K. Cannizzo, P. Ghosh, and J. C. Wheeler, Astrophys. J. Lett. **260**, L83 (1982).
16. R. Hoshi, Publ. Astron. Soc. Jpn. **36**, 785 (1984).
17. P. Szkody, Astrophys. J. Lett. **192**, L75 (1974).
18. R. J. Stover, *White Dwarfs and Variable Degenerate Stars* (Univ. of Rochester, Rochester, 1979), p. 489.
19. M. F. Walker, Astrophys. J. Lett. **248**, 256 (1981).
20. P. Szkody, Astrophys. J. **207**, 824 (1976).
21. P. Szkody, Astrophys. J. **217**, 140 (1977).
22. A. V. Holm and J. C. Gallagher, Astrophys. J. **192**, 425 (1974).
23. S. Rappaport, W. Cash, R. Doxsey, *et al.*, Astrophys. J. **187**, 5 (1974).
24. I. D. Howarth, J. Brit. Astron. Assoc. **88**, 458 (1978).
25. G. T. Bath and J. van Paradijs, Nature **305**, 33 (1983).
26. J. K. Cannizzo and J. A. Mattei, Astrophys. J. **401**, 642 (1992).
27. J. K. Cannizzo, Astrophys. J. **419**, 318 (1993).
28. A. H. Joy, Astrophys. J. **124**, 317 (1956).
29. J. Echevarría, F. Diego, M. Tapia, *et al.*, Mon. Not. R. Astron. Soc. **240**, 975 (1989).
30. F. V. Hessman, E. L. Robinson, R. E. Nather, *et al.*, Astrophys. J. **286**, 747 (1984).
31. G. Grant, Astrophys. J. **122**, 566 (1955).
32. M. C. Zuckerman, Ann. Astrophys. **24**, 431 (1961).
33. W. B. Honey, G. T. Bath, P. A. Charles, *et al.*, Mon. Not. R. Astron. Soc. **236**, 727 (1989).
34. I. B. Voloshina, Pis'ma Astron. Zh. **12**, 219 (1986).
35. I. B. Voloshina and V. M. Lyutyĭ, Astron. Zh. **70**, 61 (1993).

36. A. Bruch, Acta Astron. **40**, 369 (1990).
37. G. Grant and H. A. Abt, Astrophys. J. **129**, 320 (1959).
38. T. S. Khruzina, Astron. Zh. **68**, 1211 (1991).
39. A. V. Goncharskiĭ, A. M. Cherepashchuk, and A. G. Yagola, *Ill-posed Problems of Astrophysics* [in Russian] (Nauka, Moscow, 1985), p. 162.
40. N. I. Shakura and R. A. Sunyaev, Astron. Astrophys. **24**, 337 (1973).
41. G. Djurasevic, Astrophys. Space Sci. **240**, 317 (1996).
42. D. M. Himmelblau, *Applied Nonlinear Programming* (McGraw-Hill, New York, 1972; Mir, Moscow, 1975), p. 163.
43. P. Charbonneau, Astrophys. J., Suppl. Ser. **101**, 309 (1995).
44. S. Davey and R. C. Smith, Mon. Not. R. Astron. Soc. **257**, 476 (1992).
45. G. M. H. J. Habets and J. R. W. Heintze, Astron. Astrophys., Suppl. Ser. **46**, 193 (1981).
46. A. P. Coroley, D. Crampton, and J. B. Hutchings, Astrophys. J. **241**, 269 (1980).
47. T. Hamada and E. E. Salpeter, Astrophys. J. **134**, 683 (1961).
48. F. Giovannelli and I. G. Martínez-Pais, Space Sci. Rev. **56**, 313 (1991).
49. A. L. Kiplinger, Astron. J. **84**, 655 (1979).

Translated by A. Dambis